

PREVENTION OF PHYSICAL AGING WITHIN CARBON MOLECULAR SIEVE
MEMBRANES FOR GAS SEPARATIONS

by

Whitney K. Cosey



APPROVED BY SUPERVISORY COMMITTEE:

Dr. Inga H. Musselman, Chair

Dr. John P. Ferraris

Dr. Kenneth Balkus Jr.

Dr. Mihaela C. Stefan

Copyright 2020

Whitney K. Cosey

All Rights Reserved

I would like to dedicate my dissertation to the people whose voices and actions have made it possible for me to be where I am today.

PREVENTION OF PHYSICAL AGING WITHIN CARBON MOLECULAR SIEVE
MEMBRANES FOR GAS SEPARATIONS

by

WHITNEY K. COSEY, BS

DISSERTATION

Presented to the Faculty of
The University of Texas at Dallas
in Partial Fulfillment
of the Requirements
for the Degree of

DOCTOR OF PHILOSOPHY IN
CHEMISTRY

THE UNIVERSITY OF TEXAS AT DALLAS

August 2020

ACKNOWLEDGMENTS

I would like to express my sincere gratitude towards my supervisor, Dr. Inga H. Musselman, for her academic guidance and support throughout the PhD program.

I would like to thank Dr. Kenneth J. Balkus, Jr. as well as Dr. John P. Ferraris for their continual encouragement during my degree, and for their constant motivation to endeavor into areas outside of my comfort zone.

I wish also to thank Dr. Mihaela Stefan for her support and expertise.

Special mentions go to past and present members of Dr. Inga H. Musselman's research group. Their support allowed me to fulfill not only my research requirements but also provided me with so much more knowledge than I anticipated.

Finally, I wish to thank my husband and family whose love has made even the toughest days easier to overcome.

July 2020

PREVENTION OF PHYSICAL AGING WITHIN CARBON MOLECULAR SIEVE
MEMBRANES FOR GAS SEPARATIONS

Whitney K. Cosey, PhD
The University of Texas at Dallas, 2020

Supervising Professor: Dr. Inga H. Musselman, Chair

Carbon molecular sieve membranes (CMSMs) are a subclass of porous materials with the ability to perform molecular sieving. Controlling the jump lengths from one pore to another allows for enhanced permselectivity of such membranes. This control makes CMS materials extraordinarily attractive for gas separations, in comparison to state-of-the-art polymeric membranes that separate molecules based primarily on sorption-diffusion. This work considers the recent progress in the development of carbon membranes as well as limitations that prevent their commercialization, in particular the rapid onset of aging that occurs with CMSMs. Various aspects of how properties of a CMSM may change over time and how important it is to find the optimum starting materials and process conditions to minimize aging are addressed within. Conditions which affect the performance of CMSMs and current preparation methods are explored and aligned with future research needed to achieve commercially viable CMSMs.

Chapter 1 summarizes the history and applicability of CMSMs along with their ability to surpass commercially used polymeric membranes for gas separations. A focus on their limitations, primarily physical aging, is addressed along with current endeavors to mitigate it.

Chapter 2 explicates the novel use of metal nanoparticles in CMSMs to scaffold membranes' inherent pore structure to minimize aging. The in-situ formation of copper nanoparticles within polymer of intrinsic microporosity-1 (PIM-1) was studied via transmission electron microscopy and gas permeation.

Chapter 3 describes the synthesis of tailored metal pillars which can be used for various polymeric precursors, including Matrimid[®] 5218 and PIM-1. The tunability of the size of the metal nanoparticles provides a more universal approach to reduce physical aging within CMSMs that can be monitored by means of gas permeation.

TABLE OF CONTENTS

ACKNOWLEDGMENTS	v
ABSTRACT	vi
LIST OF FIGURES	x
LIST OF TABLES	xiv
CHAPTER 1 INTRODUCTION	1
1.1 Polymeric membrane precursors used for carbon membranes	6
1.2 General fabrication conditions for carbon membranes	8
1.3 Challenges with carbon membranes: chemical and physical aging	10
1.4 Current methods to reduce physical aging	21
1.5 Future direction in carbon membrane research	28
1.6 References	30
CHAPTER 2 AGE REDUCTION IN HIGHLY POROUS CARBON MOLECULAR SIEVE MEMBRANES	42
2.1 Abstract	43
2.2 Introduction	44
2.3 Experimental	46
2.4 Results and discussion	53
2.5 Conclusions	62
2.6 Acknowledgments	62
2.7 Appendix- Supporting information	62

2.8	References.....	65
CHAPTER 3 TAILORING COPPER PILLARS TO PREVENT PHYSICAL AGING IN CARBON MOLECULAR SIEVE MEMBRANES		71
3.1	Abstract.....	72
3.2	Introduction.....	73
3.3	Experimental.....	76
3.4	Results and discussion	82
3.5	Conclusions.....	98
3.6	Acknowledgments.....	98
3.7	Appendix- Supporting information.....	99
3.8	References.....	102
APPENDIX A A THERMAL CVD METHOD FOR THE SYNTHESIS OF AN AMORPHOUS CARBON GUTTER LAYER ON STAINLESS STEEL.....		105
 BIOGRAPHICAL SKETCH		112
 CURRICULUM VITAE.....		113

LIST OF FIGURES

Figure 1.1: Schematic illustration of turbostratic carbon reproduced with permission from Wiley Materials. ³³	3
Figure 1.2: Physical aging process of glassy polymers, reproduced with permission from Elsevier. ³⁹	5
Figure 1.3: Stylized Robeson plot ⁴⁷ showing selectivity-permeability trade-off for membrane systems and the effect of physical aging of CMSMs.....	6
Figure 1.4: Chemical structure of (a) Polybenzimidazole, (b) Matrimid [®] 5218, (c) 6FDA-Ar polymer precursors (Ar=1: 6FDA-DABA, Ar=2: 6FDA-DAM, Ar=3: 6FDA-NDA, Ar=1+2: 6FDD), and (d) Novolac.	7
Figure 1.5: (a) Plot of surface area versus pore width for a PIM-6FDA-OH membrane carbonized at various temperatures, and (b) corresponding XRD patterns reproduced with permission from Elsevier. ⁷⁸	9
Figure 1.6: Representation of chemical aging in CMSMs, adapted from Xu et al. ³¹	10
Figure 1.7: (a) Normalized plot of permeance versus time for a CMSM derived from a Novolac phenolic resin stored under (a) air laboratory environment, and (b) under nitrogen, reproduced with permission from Elsevier. ⁷⁷	11
Figure 1.8: Transition from turbostratic carbon to a more thermodynamically stable conformation.	16
Figure 1.9: Plot of CO ₂ permeance and CO ₂ /CH ₄ selectivity against time for a 6FDA-DETDA:DABA CMS fiber, reproduced with permission from Elsevier. ⁴⁷	18
Figure 1.10: Plot of normalized propylene permeance versus time for a Matrimid [®] 5218-derived CMSM operated at 2 and 7 bar at 50 °C, reproduced with permission from Elsevier. ¹⁰⁵	19
Figure 1.11: Time dependence of the on-stream separation performance of a CMSM for a 50:50 C ₃ H ₆ /C ₃ H ₈ gas mixture with a feed pressure of 2 bar at room temperature. Reprinted with permission from (Ma, X.; Williams, S.; Wei, X.; Kniep, J.; Lin, Y. S., <i>Ind. Eng. Chem. Res.</i> 2015 , <i>54</i> (40), 9824-9831.). Copyright (2015) American Chemical Society. ¹⁰⁶	20
Figure 1.12: Plot of CO ₂ permeance and CO ₂ /CH ₄ selectivity against time for a 10 ppm PPDA treated 6FDA: BPDA-DAM CMS fiber, reproduced with permission from Wiley Materials. ¹²⁵	25

Figure 1.13: Plot of propane (purple) and propylene (black) permeability alongside propane/propylene selectivity against time for (a) 6FDA-DABA, and (b) crosslinked 6FDA-DABA CMSMs, reproduced with permission from Elsevier. ⁹²	26
Figure 2.1: (a) Chemical structure of PIM-1, and (b) MOP-18	46
Figure 2.2: (a) TGA and derivative TGA curves of pristine PIM-1 (orange) and 40 wt/wt MOP-18/PIM-1 MMM (blue), and (b) DSC curve of 40 wt/wt MOP-18/PIM-1 MMM.	54
Figure 2.3: (a, b) TEM images of 40 wt/wt MOP-18/PIM-1 CMSM, and (c) its corresponding histogram.....	55
Figure 2.4: X-ray diffraction pattern of a 40 wt/wt MOP-18/PIM-1 derived CMSM.....	55
Figure 2.5: Raman spectra of carbon: (a) PIM-1, (b) MOP-18, and (c) 40 wt/wt MOP-18/PIM-1.	56
Figure 2.6: (a) Plot of CO ₂ /CH ₄ selectivity versus CO ₂ permeability for a 21-day aged 40 wt/wt MOP-18/PIM-1 CMSM, alongside CMSMs reported in literature on Robeson's CO ₂ /CH ₄ upperbound. ⁴⁰ PBI/Matrimid (), ⁴¹ PBI/UIP-S (○), ⁴¹ P84 (●), ⁴² 6FDA/PMDA-TMMDA (), ⁴³ PIM-PI (). ⁴⁴ (b) Plot of CO ₂ /CH ₄ selectivity versus CO ₂ permeability for fresh (b, ■) and aged (b, □) 40 wt/wt MOP-18/PIM-1 CMSMs alongside fresh (b, ▲) and aged (b, △) PIM-1 derived CMSMs.....	58
Figure 2.7: (a) Plot of normalized methane permeability versus time acquired under vacuum, and (b) plot of CO ₂ and CH ₄ permeability versus time acquired under a pressure gradient with a 50:50 CO ₂ :CH ₄ gas mixture. (a) 40 wt/wt MOP-18/PIM-1 (blue), PIM-1 bulk (green), PIM-1 submicron (black, from literature ⁴⁴); (b) CO ₂ permeability (blue) and CH ₄ permeability (red) of 40 wt/wt MOP-18/ PIM-1 CMSM.....	61
Figure 2.8: ATR-FTIR spectra of membranes: (a) Full spectra of PIM-1 (black), 40 wt/wt MOP-18/PIM-1 MMM (green), and MOP-18 powder (blue) along with Insets. (b) -CN stretch (c) C=C alkene stretch, and (d) C-O stretch.....	63
Figure 2.9: SEM images of polymer membrane cross-sections: (a) PIM-1, and (b) 40 wt/wt MOP-18/PIM-1 MMM	64
Figure 2.10: X-ray diffractions of PIM-1 (black), and 40 wt/wt MOP-18/ PIM-1 derived (blue) CMSMs.....	65
Figure 2.11: XPS spectra of 40 wt/wt MOP-18/PIM-1 CMSM: (a) survey, (b) carbon, and (c) copper.....	65

Figure 3.1: TGA of pristine polymers (orange), their corresponding MMMs (Blue), and MOP-18 (Black): (a) PIM-1, and (b) Matrimid [®] 5218	83
Figure 3.2: (a) XRD pattern and (b) DSC trace of Matrimid [®] 5218 (blue), and PIM-1(black) derived CMSMs with 40 wt/wt loading of MOP-18.	84
Figure 3.3: Raman spectra of MOP-18/Matrimid [®] 5218 CMSMs pyrolyzed at 550 °C with (a) 0, (b) 20, (c) 40, and (d) 80 wt/wt loadings of MOP-18.	86
Figure 3.4: Transmission electron microscopy of MOP-18/ Matrimid [®] 5218 derived CMSMs pyrolyzed at 550 °C, 2 h: (a) 20 wt/wt , (b) 40 wt/wt, (c) 80 wt/wt	88
Figure 3.5: Copper particle size distribution within MOP-18/Matrimid [®] 5218 derived CMSMs at pyrolysis conditions (a) 550 °C, 0 h and (b) 550 °C, 2 h as a function of MOP-18 loading: 20 wt/wt (blue), 40 wt/wt (orange), and 80 wt/wt (gray).....	88
Figure 3.6: Transmission electron microscopy images of 40 wt/wt MOP-18/Matrimid [®] 5218 CMSMs pyrolyzed at (a) 550 °C, 0 h, (b) 550 °C, 2 h, (c) 550 °C, 4 h, (d) and 550 °C, 6 h.	89
Figure 3.7: Copper particle size distribution within a 40 wt/wt MOP-18/Matrimid [®] 5218 derived CMSM at 550 °C (a) and 900 °C (b) as a function of soaking duration for 0, 2, 4, and 6 h	90
Figure 3.8: Copper particle size distribution within MOP-18/Matrimid [®] 5218 derived CMSMs as a function of carbonization temperature, 550 °C (blue) versus 900 °C (orange) for: (a) 20 wt/wt, (b) 40 wt/wt, and (c) 80 wt/wt MOP-18 loadings.....	91
Figure 3.9: TEM images of (a) 40 wt/wt MOP-18/Matrimid [®] 5218 CMSM and (b) 40 wt/wt MOP-18/PIM-1 CMSM, and (c) their corresponding histograms.	92
Figure 3.10: (a) Plot of CO ₂ adsorption at 0 °C versus relative pressure for PIM-1-derived CMSMs, and (b) their corresponding pore size distribution calculated from the 2D-NLDFT.	94
Figure 3.11: (a) Plot of CO ₂ adsorption at 0 °C versus relative pressure for Matrimid [®] 5218-derived CMSMs, and (b) their corresponding pore size distribution calculated from the 2D-NLDFT	95
Figure 3.12: Change in CH ₄ permeability upon aging for 0 wt/wt (blue), 20 wt/wt (orange), and 40 wt/wt (black) MOP-18/Matrimid [®] 5218 derived CMSMs at 550-2.	96
Figure 3.13: (a) Plot of normalized CH ₄ permeability versus time for Matrimid [®] 5218 derived CMSMs under reduced pressure, and (b) plot CH ₄ and CO ₂ permeability versus time for a 40 wt/wt MOP-18/Matrimid [®] 5218 CMSM pyrolyzed at 550 °C under a pressure gradient	97

Figure 3.14: (a) FTIR spectra of MOP-18 and Matrimid [®] 5218 derived MMMs, with insets highlighting the (b) C-H, and (c) Cu-O stretch associated with the incorporation of MOP-18	99
Figure 3.15: (a) FTIR spectra of MOP-18 and PIM-1 derived MMMS with insets highlighting (b) -CN stretch associated with PIM-1, along with the (c) C=C alkene and (d) Cu-O stretch associated with the incorporation of MOP-18	100
Figure 3.16: XPS spectra of 40 wt/wt MOP-18/Matrimid [®] 5218 CMSM: (a) survey, and (b) copper.....	100
Figure 3.17: XPS spectra of 40 wt/wt MOP-18/PIM-1 CMSM: (a) survey, and (b) copper.....	101
Figure 3.18: Raman spectra of (a) PIM-1, (b) MOP-18 powder, and (c) 40 wt/wt MOP-18/PIM-1 MMM pyrolyzed at 550-2.....	101
Figure 3.19: Raman spectra of MOP-18/ Matrimid [®] 5218 CMSMs pyrolyzed at 900-2 with (a) 0, (b) 20, (c) 40, and (d) 80 wt/wt loadings of MOP-18.....	101
Figure 3.20: Plot of copper particle size versus particle count (%) within a 20 and 40 wt/wt MOP-18/ PIM-1 derived CMSMs	102
Figure A.1: Schematic of tubular support acquired from Graver technologies.....	107
Figure A.2: Procedure for a-carbon growth on 316L stainless steel.....	107
Figure A.3: Image of a PBI CMSM on a pristine SS tubular support	109
Figure A.4: (a, b) SEM images, and (c) Raman spectra of amorphous carbon grown on 316L stainless steel.....	110
Figure A.5: (a) Stainless steel tubular support following a-carbon growth, (b) and a PBI CMSM adhered to the a-carbon gutter layer.....	110

LIST OF TABLES

Table 1.1: I_D/I_G height ratios of various carbons and CMSMs.	12
Table 1.2: Pore width and pore volume for selected CMSMs pyrolyzed at various temperatures.	21
Table 2.1: I_D/I_G height ratios, corresponding L_a values, and G-band positions for PIM-1, MOP-18, and 40 wt/wt MOP-18/PIM-1 pyrolyzed at 550 °C	57
Table 2.2: Pure gas permeabilities (in Barrers) at 35 °C and 2 bar of fresh and aged carbon molecular sieve membranes.	59
Table 2.3: Mixed gas permeabilities (in Barrers) at 35 °C and 2 bar of a 40 wt/wt MOP-18/PIM-1 carbon molecular sieve membrane.....	60
Table 3.1: I_D/I_G height ratios of CMSMs pyrolyzed at 550 °C and 900 °C along with their corresponding L_a (Å) values and G-band (cm^{-1}) positions	86
Table 3.2: Pure gas permeabilities (in Barrer) of MOP-18 Matrimid® 5218 membranes at 35 °C and 2 bar.....	96
Table A.1: Chemical composition of stainless-steel type 316L	106

CHAPTER 1

INTRODUCTION

Polymeric membranes have been the state of the art for gas separations for several decades due to three primary factors: low material cost, ease of processing, and compact geometry.¹ While polymeric membranes are relatively inexpensive and require less energy than other gas separation techniques, such as pressure swing adsorption and distillation, they are limited by their inherent permeability-selectivity tradeoff.¹⁻⁴ As a consequence, fewer than 10 polymer-based membranes are used industrially for gas separations, even though hundreds of polymers have been investigated.⁵ Polymeric membranes also undergo a process known as plasticization, which occurs when the membrane is exposed to highly soluble species such as CO₂ causing swelling within the matrix.^{3,6} The swelling results in the loss of a membrane's ability to effectively sieve gas molecules.⁶⁻⁸ These limitations suffered by polymeric membranes have encouraged researchers to develop carbon molecular sieve membranes.²

Carbon molecular sieve membranes (CMSMs), which are formed by the pyrolysis of polymer precursors, have the ability to overcome the trade-off associated with polymers and the processability difficulties of inorganic membranes, such as zeolites and metal-organic frameworks (MOFs).¹ CMSMs can be used for separations that occur at elevated temperatures and in harsh chemical environments.⁹⁻¹¹ Carbon membranes are also promising materials that exhibit enhanced gas permeation and gas selectivity compared with polymeric membranes, due to their microporous and amorphous nature.⁹ This allows carbon membranes to surpass the upper bound limits of permeability-selectivity reported for polymer membranes in 1991 and 2008 by Robeson.¹² Also, unlike inorganic membranes, CMSMs are relatively easy to fabricate and less expensive.¹¹

Carbon membranes are being investigated for use in difficult gas separations that require a tailored pore size (e.g., H₂/CO₂, O₂/N₂, CO₂/CH₄, CH₄/N₂, and C₃H₆/C₃H₈).¹⁰ To achieve enhanced separations, both the aperture size and the functionality surrounding the pores of the membrane are important.¹⁰ The pore size of a carbon membrane, usually within the range of 0.2 to 2.0 nm, is formed from imperfectly packed graphene layers.¹⁰ Ultramicropores with apertures of <0.7 nm are two-dimensional passage ways formed from defects within the graphene plates, which provide the membrane's high selectivity.^{11, 13-15} Micropores ranging from 0.7 to 2.0 nm are formed by defects between graphene plates, providing the high permeation values associated with carbon membranes.¹³

The pyrolysis of polymeric precursors under an inert atmosphere result in CMSMs, and the generation of gaseous products creates pores.¹¹ The application of density functional theory (DFT) to analyze N₂ adsorption data results in a bimodal distribution of micropores, i.e., ultramicropores (<0.7 nm) and micropores (0.7-2.0 nm), which has been used to explain the gas separation properties of CMSMs. However, it has been shown by Thommes et al. that DFT analysis yields an artifact at ~1 nm, which results in two pore sizes that are often repeated for CMSMs.¹⁶⁻¹⁸ A more accurate model for the pore size distribution is quenched solid-state density functional theory (QSDFT), which eliminates this artifact, revealing a broad distribution of pores ranging from ultra to macropores.^{11,17-20} Due to CMSMs pore size distribution, the gas transport mechanism takes place according to molecular sieving and sorption-diffusion.^{10,21}

The importance of selecting an appropriate polymer precursor with a high glass transition temperature (T_g) has previously been noted.^{10,11,22} A fundamental knowledge of the precursor chemistry is needed to create carbon membranes with tunable pore structures.¹³ Additionally, the

carbonization protocol, which tailors the pore structure either by adjusting the soak temperature or the ramp rate, is important.^{23,24}

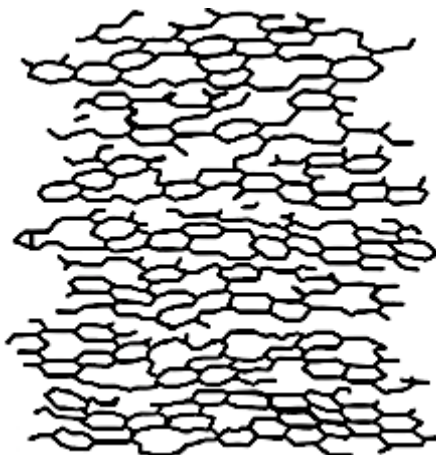


Figure 1.1: Schematic illustration of turbostratic carbon reproduced with permission from Wiley Materials.³³

When forming CMSMs, the final pyrolysis temperature should remain below the graphitization temperature in order to create turbostratic carbon.¹¹ This type of carbon is a mixture of horizontally and t-shaped carbon-graphite domains with regular spacing, but varying stacking order (Figure 1.1).²⁵⁻²⁷ As the pyrolysis temperature increases, the permeability of the CMSM decreases due to a subsequent decrease in pore size (accelerated aging) accompanied by an increase in selectivity.¹¹ Modification of the CMSMs by pre- or post-treatments (e.g., incorporation of oxygen or nitrogen) may serve to functionalize the pores to increase the solubility of penetrants.^{13, 21, 28, 29}

Four challenges must be addressed for CMSMs to be a viable option for industrial applications. The most important challenge is rapid physical aging, which causes a decline in flux and thus productivity over time.¹⁰ The second is hydrophilicity, where environments with high humidity can interact with the pore surface and subsequently chemically interact with permeates.^{10,30}

Thirdly, other contaminants could block pores causing a reduction in both permeability and selectivity.¹⁰ Lastly, the presence of oxygen can reduce the effective size of the pores through the formation of carbon-oxygen surface groups.¹⁰

This chapter addresses physical aging of CMSMs, a factor that poses a threat to their long-term stability, and highlights the importance in finding the optimum processing conditions and/or starting materials. Physical aging is the collapse of a membrane's pores brought on by π - π interactions and/or a transition to a more thermodynamically favorable state (e.g., graphene). Physical aging within CMSMs is analogous to the aging that occurs with glassy polymers,³¹ which is defined as the rearrangement of segments in a polymer from a non-equilibrium state to an equilibrium state.^{31,32} A polymer exists in an equilibrium state above T_g . However, when cooled below its T_g , the movement of polymers chains reduces, allowing for the formation of free volume as shown in Figure 1.2. Below T_g , densification occurs as the polymer approaches a new thermodynamic equilibrium, accompanied by a decrease in free volume (FV).³¹ Such physical aging can result in significant changes in membrane transport properties, observed as a decrease in permeability and increase in selectivity with time.^{3,33-35} This densification process is also observed within CMSMs. Over time, there is a reduction in a membrane's micropore volume, giving rise to an increase in selectivity and subsequent decrease in permeability.^{36,37} The decline in permeability has been determined to be caused by changes in diffusivity rather than solubility.³⁸

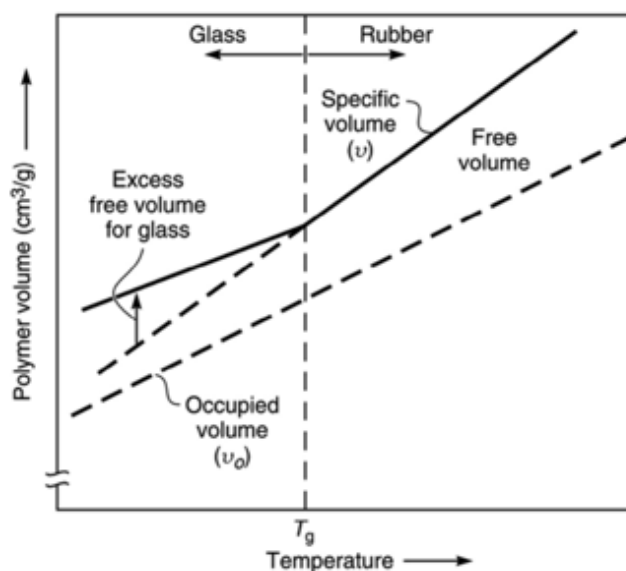


Figure 1.2: Physical aging process of glassy polymers, reproduced with permission from Elsevier.³⁹

Prior studies show that aging drastically impacts membrane performance and is a major concern for CMS membranes. Figure 1.3 illustrates a stylized Robeson upper bound for fresh and aged CMSMs and their corresponding precursor. While CMSMs outperform the precursors at 35°C and 2 atm, these values are short lived. Methods used to maintain these permselectivity values will be discussed within this chapter.

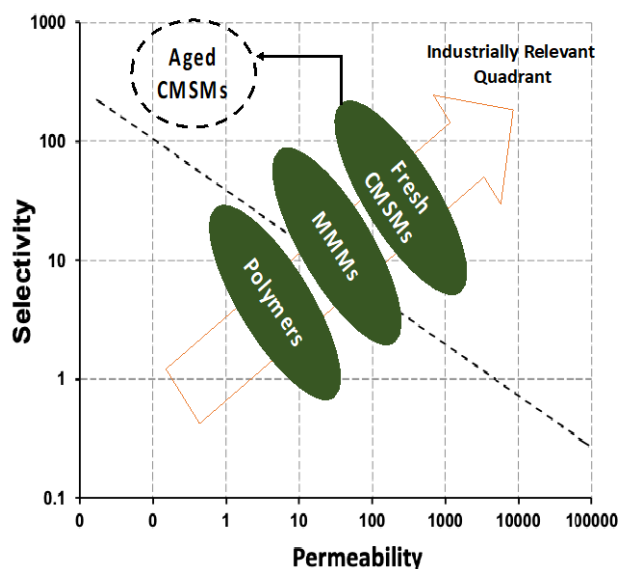


Figure 1.3: Stylized Robeson plot⁴⁷ showing selectivity-permeability trade-off for membrane systems and the effect of physical aging of CMSMs.

1.1 Polymeric membrane precursors used for carbon membranes

Selection of the precursor is one of the most important factors in obtaining a high performance CMSM.¹² Polymers such as polybenzimidazole (PBI) that have excellent thermal stability due to their high T_g and mechanical stability make ideal precursors for forming CMSMs.^{6, 40-43} Similar to PBI, Matrimid[®] 5218^{15,28,40,44-46} and 6FDA-based polyimides^{44,47-50}, have been widely studied for CMSMs. These polymers have higher glass transition temperatures ($>300\text{ }^\circ\text{C}$) than current polymers used industrially ($< 200\text{ }^\circ\text{C}$), making them more rigid and less likely to undergo densification after carbonization.^{6,12}

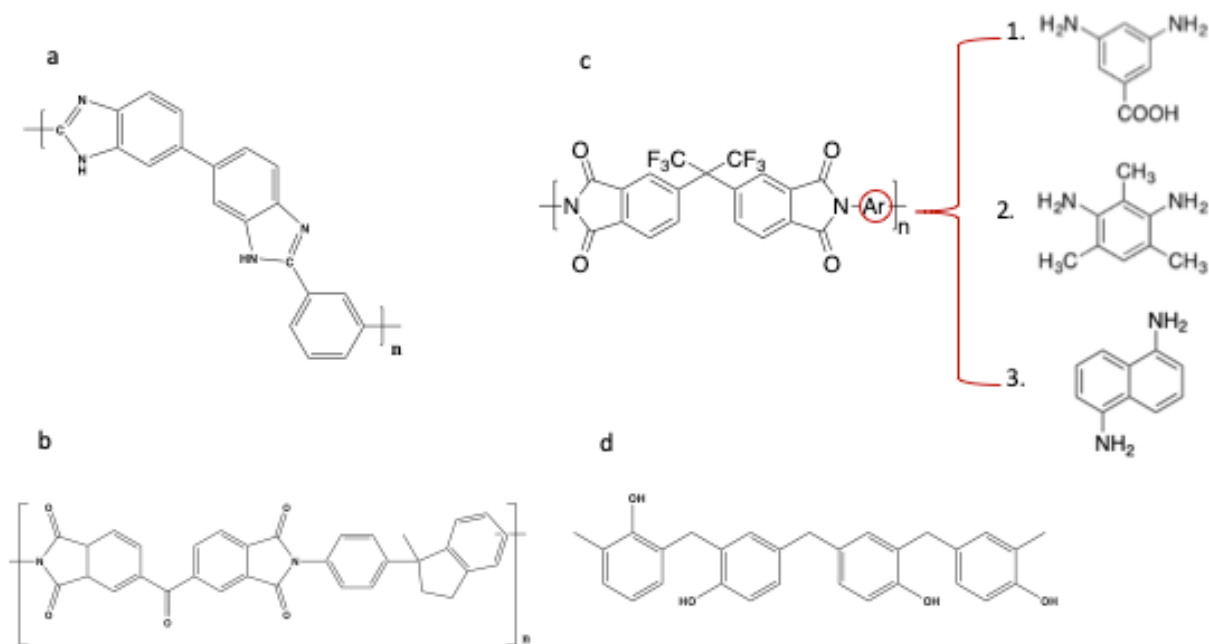


Figure 1.4: Chemical structure of (a) Polybenzimidazole, (b) Matrimid[®] 5218, (c) 6FDA-Ar polymer precursors (Ar=1: 6FDA-DABA, Ar=2: 6FDA-DAM, Ar=3: 6FDA-NDA, Ar=1+2: 6FDD), and (d) Novolac.

The chemical structures of these polymers are shown in Figure 1.4. These precursors generate CMSMs with exceptional permselectivities for difficult separations (e.g., CO₂/CH₄, N₂/CH₄, He/N₂, O₂/N₂, CO₂/N₂, C₃H₈/C₃H₆, and C₂H₆/C₂H₄), placing them above the Robeson upper-bound.^{51,52} However, they are unlikely to ever be employed for industrial applications unless aging is addressed.

The rate of physical aging for CMSMs depends on temperature, gas environment, and polymer precursor structure.³² The FV of precursors is also a key factor to be considered for CMSMs as the rate at which aging/densification occurs is highly dependent upon FV.³¹ A precursor's FV is initially retained after carbonization. Therefore, precursors with bulky side groups, such as the -CF₃ groups present in the 6FDA derivatives, form a CMSM with large pores and thus free volume.

The larger the pores, however, the more rapid physical aging occurs. The FV of the precursor can be altered by modifying the bulkiness of the side groups, and thus the rigidity of the backbone.^{35,53-}
⁵⁶ Physical aging in high FV polymer precursors has been reported by many researchers and is identified by a reduction in gas permeability, thus limiting their potential for gas separation.^{5,33,57,58} Recent studies also show that thin polymer film precursors undergo physical aging more rapidly than thick films,^{7,59-63} leading to a reduction in the membrane's permselectivity with time.^{61,64-67} This reduction has been investigated by positron annihilation lifetime spectroscopy (PALS).^{34,35,68-}
⁷¹ One significant difference between the physical aging that occurs with polymeric membranes and CMSMs is that, although both are time-dependent processes, the aging associated with polymeric membranes is reversible.^{5,7,72} This is not the case with CMSMs. Consequently, an understanding of the structural changes associated with physical aging is important in order to estimate the lifetime and durability of the carbon membrane.^{57,69} While the process of physical aging in polymeric membranes has been heavily investigated,^{32,61} limited aging studies exist for CMSMs. Work done by Schuepfer and colleagues is one of the first articles to elucidate the changes that occur during the carbonization of polymeric materials.⁷³

1.2 General fabrication conditions for carbon membranes

Carbon membranes are generally prepared by pyrolyzing a polymer precursor under inert atmospheric conditions.² The heat treatment occurs incrementally at a slow ramp rate after which the final temperature is held for a period of time, a process known as soaking.¹ During carbonization, functional groups present in the polymeric precursor, such as CO₂ and CF₃, are removed,² producing an amorphous material as shown in Figure 1.1.⁷⁴⁻⁷⁶ The packing

imperfections produce a range of micropores^{21,76-78} that give rise to CMSMs with enhanced permeability and selectivity.² While most polyimide-derived CMSMs pyrolyzed at 550°C have shown permselectivities greater than their precursors, several researchers have shown that increasing the carbonization temperature up to 900°C yields membranes with higher selectivities.⁶¹ However, there is also a subsequent decrease in permeability at higher pyrolysis temperatures^{76, 79-81} that is caused by a decrease in pore aperture (Figure 1.5).²¹

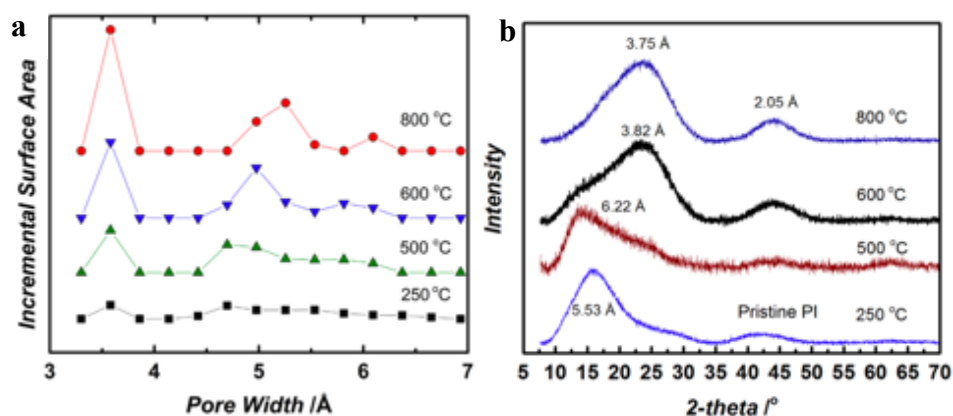


Figure 1.5: (a) Plot of surface area versus pore width for a PIM-6FDA-OH membrane carbonized at various temperatures, and (b) corresponding XRD patterns reproduced with permission from Elsevier.⁷⁸

PIM-6FDA-OH membranes were pyrolyzed at various temperatures to ascertain the effects the pyrolysis temperature has on the pore size distribution of the CMSM.⁷⁸ Figure 1.5 shows the plots comparing CMSMs pore width (Figure 1.5a) as well as the resulting d-spacing obtained from the pyrolysis at specific temperatures (Figure 1.5b). The carbonization of a PIM-6FDA-OH membrane at 800°C yielded more ultramicropores than at 500°C (Figure 1.5a) with a corresponding decrease in the distance between the graphite sheets (Figure 1.5b).⁷⁸ A small change in final pyrolysis temperature, ramp rate, or inert gas composition alters the effective micropore size drastically, altering the permeation and separation properties of the

CMSMs.^{43,50,52,77,82-88} These data highlight why it is important to optimize the method of preparation for each precursor, and also illustrate that the carbonization temperature significantly effects membrane performance. Increasing the final carbonization temperature leads to rapid physical aging, a process that will be discussed further below.

1.3 Challenges with carbon membranes: chemical and physical aging

1.3.1 Chemical aging

CMSMs undergo chemical aging when exposed to air,⁷⁷ organic compounds,³¹ and humid environments.⁷⁷ This form of aging has been investigated by several researchers, as it presents a severe threat to the use of carbon membranes for gas separations and several other applications including water purification. Xu et al. illustrate the result of CMSMs that have undergone chemical aging (Figure 1.6).³¹

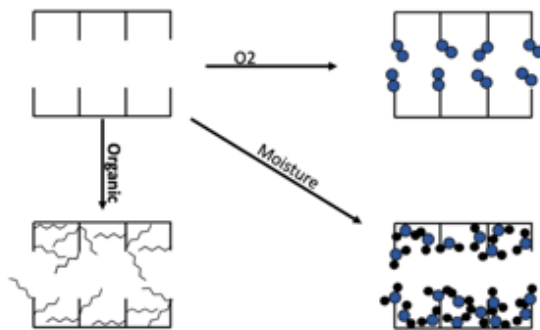


Figure 1.6: Representation of chemical aging in CMSMs, adapted from Xu et al.³¹

Figure 1.6 depicts how micropores can be blocked by large molecules such as hexane, thus causing a decrease in the permeance of CMSMs over time.^{36,37} The decrease in permeance, and subsequent

increase in selectivity, is even more prominent when the CMSM is exposed to water and/or oxygen, due to chemisorption of oxygen to the turbostratic carbon.⁷⁴ The turbostratic carbon (Figure 1.1) is composed of edges that are terminated by stable groups such as C-H. However, some edges are terminated with free radicals, which react with oxygen to form surface oxygen groups. As shown in Figure 1.6, oxygen binds to the edge sites of the CMSM impeding the flow of the penetrant gases. Water also binds to hydrophilic regions of the CMSM, generally in the form of residual functional groups, such as amines, that remain after pyrolysis.^{36,37,79}

The removal of sorbed species from CMSMs has been studied under several different environments, including air, nitrogen, and propylene.⁷⁷ Over a period of 206 days, Novolac phenolic resin (Figure 1.4d) carbonized at 700°C and stored in air showed permeance losses greater than 70% for N₂, O₂, CH₄, and CO₂ (Figure 1.7a).⁷⁷ This decrease in permeance was attributed to the formation of C-O surface groups. In contrast, when stored in nitrogen, only a 15-35% decrease in permeance was observed as shown in Figure 1.7b.⁷⁷

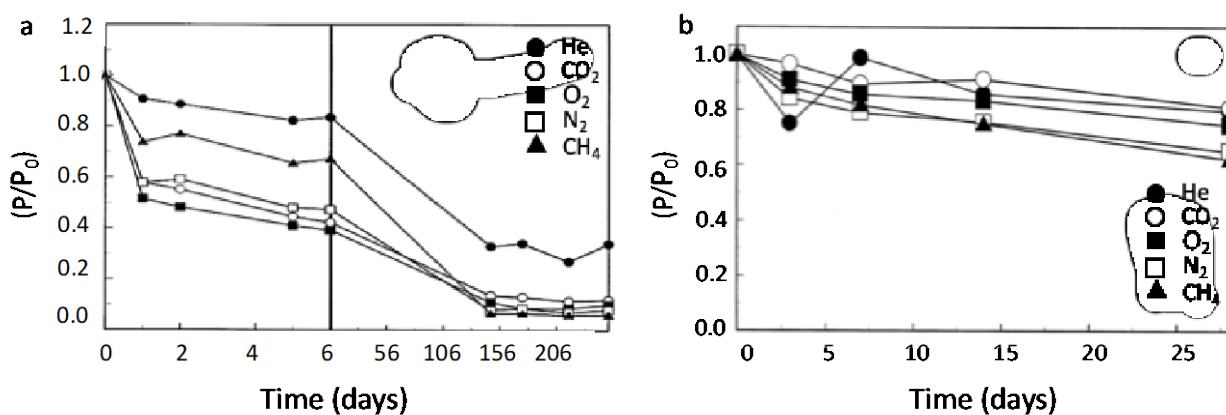


Figure 1.7: (a) Normalized plot of permeance versus time for a CMSM derived from a Novolac phenolic resin stored under (a) air laboratory environment, and (b) under nitrogen, reproduced with permission from Elsevier.⁷⁷

Similar trends were also observed for a polyetherimide membrane carbonized at 600 °C, where, when stored in air for 90 d, an ~80% decrease in permeability occurred for H₂, CO₂, O₂, N₂, and CH₄.⁷⁴ These studies further highlight that, while CMSMs show permselectivity values that are initially greater than their polymeric counterparts, the decline in permeance over time makes them unsuited for industrial applications. They also reveal the importance of storing the membrane in inert conditions to prevent the adsorption of unwanted oxygen-containing species. While chemical aging alters the permselectivity of membranes over time by blocking the pore structure of the CMSMs, it was found that the pore structure of the membrane could be regenerated. It has been shown that heat treatment, which usually entails heating the membrane to ~ 120 °C under vacuum, removed both physisorbed (H₂O) and chemisorbed species (O₂).^{74,77} Liao and coworkers showed through X-ray photoelectron spectroscopy (XPS) that increasing the pyrolysis temperature from 500 to 800 °C resulted in a corresponding decrease in oxygen content.⁸⁹ The efficiency with which the species are desorbed is based on the pore size and FV of the CMSM.

Table 1.1: I_D/I_G height ratios of various carbons and CMSMs.

Carbon or Precursor	I_D/I_G	L_a (nm)	Ref.
High purity graphite	0.11	40.0	90
Polycrystalline graphite	0.20	22.0	90
Graphite powder	0.33	13.3	91
6FDA-NDA	0.40	11.0	92
Crosslinked 6FDA-DABA	0.60	7.3	92
Activated carbon	0.67	6.6	93
Matrimid [®] 5218 (800 °C)	0.70	6.3	33

Coke	0.76	5.8	90
6FDD	0.85	5.2	92
6FDA-DABA	0.85	5.2	92
PAN (900 °C)	0.90	4.9	94
Glassy carbon	1.08	4.1	95
PAN (600 °C)	1.10	4.0	94
Diamond Film (1.5% CH ₄)	1.23	3.6	96
6FDA-DAM	1.50	2.9	92
PIM 1 (1100 °C)	1.84	2.4	97

Carbon membranes with a smaller pore aperture (<0.346 nm, kinetic diameter of O₂) can be regenerated more efficiently.⁷⁴ Wey et al. attributes this phenomenon to the fact that water molecules are smaller than oxygen and thus enter the pore aperture more readily. This decreases the amount of oxygen that can readily bind to the pores.⁷⁴ High fractional free volume (FFV) polymer precursors often yield CMSMs with larger pore apertures, which can be correlated to their I_D/I_G ratios. The I_D/I_G ratio is acquired from Raman analysis of CMSM, by taking the height intensities of the D-band (disordered carbon, 1350 cm⁻¹) and G-band (graphitic carbon, 1550-1600 cm⁻¹). An increase in the D-band, and thus the subsequent increase in I_D/I_G ratio, is a signature for high FFV CMSMs. Table 1 highlights this trend by comparing I_D/I_G ratios obtained for an array of polymer precursors. The crystallite size (L_a, Å) which is inversely proportional to the I_D/I_G ratio (Equation 1) is also displayed in Table 1, small crystallite sizes are known to create defects in the membrane due to an increase in the number of sp³ terminal carbons. These defects contribute to the formation of micropores.

$$L_a = 44(I_D/I_G)^{-1} \quad \text{Equation 1}$$

The high FFV precursors such as PIM-1 and majority of the 6FDA derivatives have I_D/I_G ratios greater than activated carbon (~ 0.7), which is known to be stable over extended periods of time.^{17,93} This increase in the I_D/I_G ratio corresponds to a smaller crystallite size, leading to an increase in the number of edge sites to which species may bind.⁵¹

Several techniques have been reported to stabilize the performance of CMSMs under oxygen environments. Menendez et al.⁷⁷ investigated the thermal regeneration of CMSMs prepared from Novolac resins (see Figure 1.5d), and observed a 2-fold increase in permeance for He, CO₂, O₂, and N₂ after heating the aged membranes (418 days in air) at 120 °C in vacuum for 3 h. However, the increase in permeance does not last. This method of regeneration is better suited to systems with pore apertures less than the kinetic diameter of oxygen (0.346 nm), as heating the system only removes physisorbed water molecules.³⁶

Jones and colleagues⁹⁸ observed a rapid decrease in oxygen permeance at 1.1 psig and 35 °C through a polyimide membrane derived from the reaction of 2,4,6-trimethyl-1,3-phenylene diamine, 5,5-[2,2,2-trifluoro-1-(trifluoromethyl) ethylidene]-1,3-isobenzofurandione and 3,3',4,4'-biphenyl tetra carboxylic acid dianhydride, pyrolyzed at 550 °C following exposure to n-hexane for 9 minutes. Chemical regeneration by purging with propylene was used to regain the original permeance. Regeneration of permeance was achieved by expanding the pores with propylene, allowing for trapped species to escape, thus cleansing the membrane. Partial restoration of the aged membrane's performance was obtained. Earlier studies by Vu et al.⁹⁹ and by Hagg et al.¹⁰ also revealed that organic contaminants (e.g., toluene and n-heptane) can be removed from the CMSM by heating the membrane to 70 °C under a dry N₂ purge. These results are interesting

in themselves as they allow for a partial recovery of the initial flux obtained from the freshly pyrolyzed membrane. However, using “cleansing agents” can be expensive. Lie et al.¹⁰⁰ were able to recover the flux of an aged CMSM by electrothermal regeneration. Pyrolyzing a cellulose acetate membrane at 650 °C, followed by the application of a direct current to the aged membrane to mimic ohmic heat, was hypothesized to remove sorbed species from the CMSM pore structure. Upon applying 30 mA to the aged membrane, indeed roughly 65% of the permeance for CO₂ was regained.¹⁰⁰ However, one downside to the method is the need to continuously regenerate the membrane with current to prevent any further sorption of species during the separation.

It would be much more beneficial to produce a CMSM that has intrinsic properties that prevent and/or minimize the degree to which oxygen and water can bind to the membrane. This perhaps can be investigated and optimized by monitoring the I_D/I_G ratios of the CMSMs. The crystallite size can be calculated from the ratio, providing insight into the number edge sites within the CMSM. Reducing the number of edges minimizes the number of sites to which oxygen and water can bind.

1.3.2 Physical aging

While CMSMs have reported significantly higher permselectivities for gas separations in comparison to polymeric membranes (see Figure 1.3), the longevity of these properties has come under heavy criticism.^{10,35,36,77,92,101} Physical aging is the result of pore collapse to achieve a thermodynamically stable structure. This aging drastically reduces the permeability of some

CMSMs in a matter of days, and is therefore a bottleneck for the implementation of CMSMs in industrial applications.

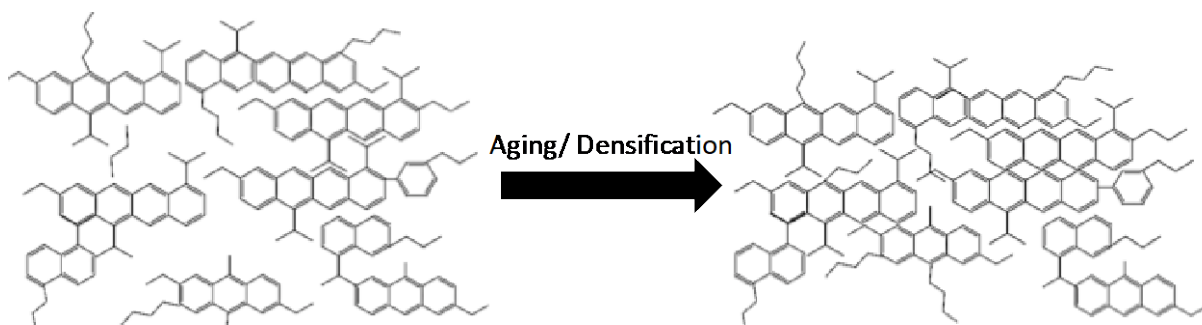


Figure 1.8: Transition from turbostratic carbon to a more thermodynamically stable conformation.

The formation of graphene sheets upon pyrolysis yields a porous structure unique to each precursor that varies based on its FFV and functionality.⁷³ These variances in structure are confirmed by PALS and tracked by permselectivities.^{102,103} This porous structure that is composed of an array of pore sizes collapses, taking on a structure that is more dense and thermodynamically more stable (see Figure 1.8).³⁶ Extended conjugation within CMSMs results in a low I_D/I_G ratio and a large crystallite size (Table 1). The π - π interactions drive the restacking of these graphene-like domains with concomitant pore collapse, and may be the underlying mechanism behind the commonly accepted physical aging model for CMSMs.^{33,38,100,103,111} On the other hand, CMSMs with high I_D/I_G ratios have small unconnected domains, which lead to a rearrangement of the CMSM to a more thermodynamically stable state. This is hypothesized to be a primary cause associated with physical aging observed in CMSMs having an I_D/I_G ratio greater than ~ 0.7 . Further analysis of the literature reveals an ‘ideal’ I_D/I_G ratio centered around Matrimid[®] 5218 and

activated carbon (AC), where carbons with ratios greater or less than ~ 0.7 age more rapidly (< 7 days).^{37, 83,119,120}

While carbon membranes are known for being both chemically stable and thermally resistant, there are still significant problems related to their stability which need to be addressed. In terms of rate of aging, it is well known that carbons derived from polymers of intrinsic microporosity, such as PIM-1, undergo aging rapidly (within hours).^{83,119} This rapid aging is also observed with other high FFV polymers such as the 6FDA-based polymers.^{37,120} These polymers serve as extremes in terms of comparing graphitic content to physical aging, as they are influenced by both thermodynamics and non-covalent interactions. However, when comparing polymer precursors, such as PBI and Matrimid[®] 5218, which have relatively low fractional free volume in comparison to 6FDA, these non-covalent interactions such as π - π interactions play a prominent role in the collapse of the carbon membranes pore structure.

To maintain the permeability of carbon molecular sieve membranes, a method to prevent the collapse of pores must be implemented, while managing to maintain selectivity. Rigid polymers that have high glass transition temperatures, such as PBI ($T_g = 417$ °C),⁵² 6FDA-DAM ($T_g = 424$ °C)³³, and Matrimid[®] 5218 ($T_g = 323$ °C),⁵² are selected for this reason.¹³ Polymer precursors with high T_g values have a more rigid backbone which should remain intact upon pyrolysis, yielding CMSMs that can withstand pore structure collapse.^{13,104} Even so, it has been observed that high FFV precursors (e.g., 6FDA-derivatives) collapse faster and to a greater extent than Matrimid[®] 5218.³¹

Polymers with higher FFV generally provide higher permselectivities when carbonized, allowing for great strides in olefin separations.^{15,87,92,104} This is due to their high rigidity and larger

micropores.³¹ Functional groups such as $-CF_3$ which minimizes movement, preserves the membranes FV following pyrolysis, thus yielding large pores. While the permselectivity values obtained for a freshly carbonized membrane lie in the industrially relevant quadrant of the Robeson upper bound plot for many gas separations (Figure 1.3), the severe decline in flux still renders them insufficient for commercial applications.

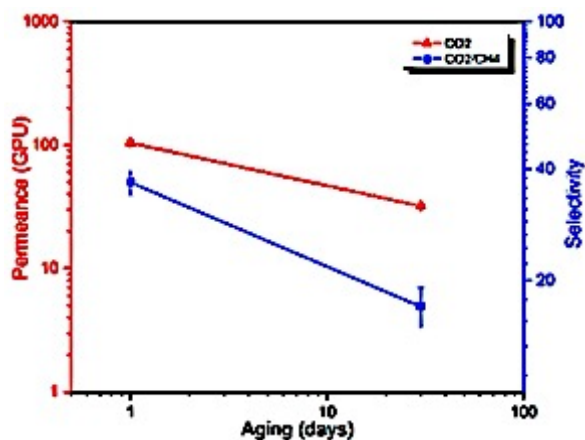


Figure 1.9: Plot of CO₂ permeance and CO₂/CH₄ selectivity against time for a 6FDA-DETDA:DABA CMS fiber, reproduced with permission from Elsevier.⁴⁷

Figure 1.9 shows results typical for high FFV polymers, in which a CMSM undergoes rapid physical aging over a period of 30 d.⁴⁷ The 6FDA-DETDA:DABA hollow fiber membrane has a T_g of 388 °C. After pyrolysis at 550 °C, the CMS fiber's initial CO₂ permeance of 100 GPU decreased by 60%.⁴⁷ The authors also reported a decrease in selectivity, which is highly unusual given that a decrease in permeance is usually accompanied by an increase in selectivity as a result of physical aging. This phenomenon was attributed to a non-standard skin formation.

Xu and co-workers³¹ investigated a Matrimid® 5218 derived CMSM at 100 psia and 35 °C. The polymer precursor's T_g (323 °C) is lower than the above mentioned 6FDA polymer precursor. While it has been suggested that polymer precursors with high T_g have a more rigid backbone, a

60% decrease in permeance is still observed within the first 5 d. However, the gases being investigated in this study were ethane/ethylene whose kinetic diameters are 0.41 nm and 0.44 nm, respectively. These larger molecules are restricted much faster than smaller gas molecules due to the collapse of the pores. For example, ethylene (0.44 nm) is less likely to pass through a dense membrane than carbon dioxide, which has a kinetic diameter of 0.33 nm.

While the mechanisms behind physical aging for high and low FV polymer precursors are believed to differ, one parameter which may influence both types of precursors equally is the gas feed pressure. Kim et al. investigated the effects of feed pressure on CMSMs long term stability. It was observed that by increasing the feed pressure the rate at which aging occurs is increased. As shown in Figure 1.10 a Matrimid[®] 5218 CMSM carbonized at 650 °C decreased in permeance over time for both operating pressures.¹⁰⁵ This data would suggest that the standard operating pressure of 2 bar is optimal for preserving the membranes permselectivity.

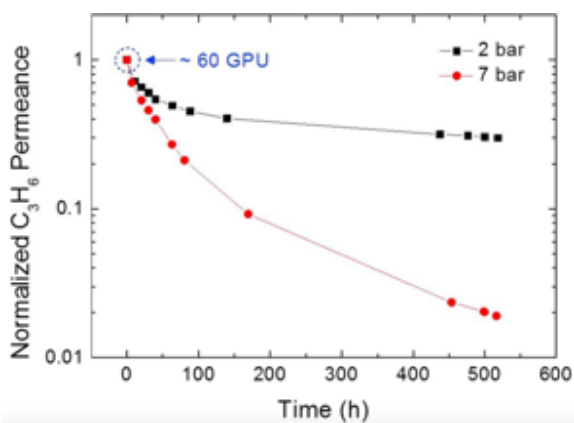


Figure 1.10: Plot of normalized propylene permeance versus time for a Matrimid[®] 5218-derived CMSM operated at 2 and 7 bar at 50 °C, reproduced with permission from Elsevier.¹⁰⁵

Ma et al.¹⁰⁶ investigated a proprietary 6FDA-based CMSM and observed similar results with a 1:1 propylene:propane feed at an operating pressure of 2 bar. The permeance of propylene and propane decreased as a function of time and the propylene/propane selectivity increased slightly (Figure 1.11).

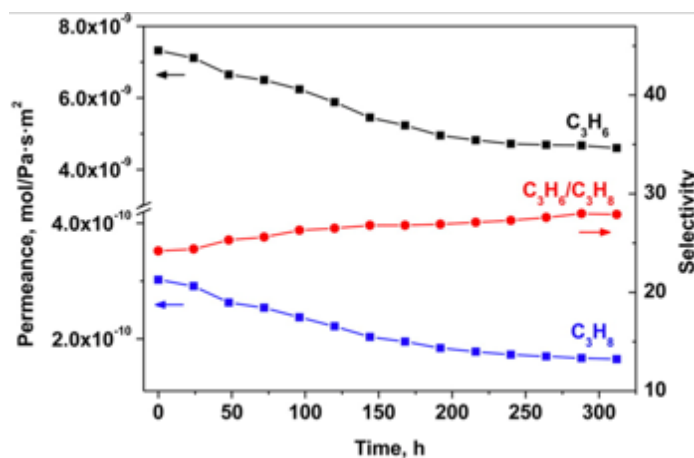


Figure 1.11: Time dependence of the on-stream separation performance of a CMSM for a 50:50 C₃H₆/C₃H₈ gas mixture with a feed pressure of 2 bar at room temperature. Reprinted with permission from (Ma, X.; Williams, S.; Wei, X.; Kniep, J.; Lin, Y. S., *Ind. Eng. Chem. Res.* **2015**, *54* (40), 9824-9831.). Copyright (2015) American Chemical Society.¹⁰⁶

While the densification of carbon membranes over time is similar to the physical aging of glassy polymers, one of the fundamental differences is that it is an irreversible process.²¹ The graphene-like sheets form a tunable structure that is highly dependent on the precursor composition and pyrolysis conditions. Further knowledge is required to correlate how the precursor structure and pyrolysis temperature influence the packing of the graphene sheets and thus the final pore aperture obtained.

Table 1.2: Pore width and pore volume for selected CMSMs pyrolyzed at various temperatures.

Carbon precursor	Pyrolysis temperature (°C)	Pore width (Å)	Pore volume (cm ³ /g)	Reference
Matrimid® 5218	550	2.8 - 10	0.1041	107, 108
PIM-1	250	3.6 - 4.7	-	95
PIM-1	400	3.6 - 4.7	-	95
PIM-1	600	3.5 - 5	-	95
PIM-1	800	3.5 - 5	-	95
6FDA/DETDA	550	5.5 - 8.8	0.1342	107
6FDA/DETDA:DABA (3:2)	550	5.5 - 8.8	0.2458	107
6FDA/DETDA:DABA (3:2)	800	5.5 - 8.8	0.1738	56
6FDA:BPDA-DAM	550	6 - 8.9	0.169	101
6FDA:BPDA-DAM	600	5.9 - 8.9	0.163	101
6FDA:BPDA-DAM	675	5.7 - 8.9	0.156	101
6FDA:BPDA-DAM	800	5.7 - 8.9	0.157	101
PAN	600	~10.2	0.032	109
PAN	700	~12.4	0.04	109
PAN	800	~13.1	0.034	109

The investigation into the graphitic content of the CMSMs (Table 1.1) and the pore size distribution (Table 1.2) may allow predictions to be made about the rate of physical aging. Tracking the pore size after altering conditions, such as soak temperature, will also provide insight on how to effectively tune a CMSM while minimizing physical aging. As shown in Table 1.2 for high FFV polymer precursors, increasing the soak temperature fine tunes the pore aperture and volume. Perhaps there is a unique temperature for every precursor that would allow for both enhanced permselectivity and minimal aging.

1.4 Current methods to reduce physical aging

The long-term stability of CMSMs is of great importance not only for the future of membrane technology, but also for industrial (e.g., CH₄ purification) and environmental (e.g., reduction of

CO₂ emissions in power plants) applications. The investigation into chemical aging associated with CMSMs has led to plausible methods for the regeneration of aged carbon membranes. However, advances in preventing physical aging are limited.

Studies performed by Hays et al. have shown that physical aging can be prevented during transport by storing the membranes under 7 bar CO₂.³⁸ However, further studies will be needed to identify conditions to prevent long-term physical aging. Physical aging affects not only the permselectivity of the membrane but also its mechanical properties. For example, carbon membranes fabricated by pyrolysis of a polymeric precursor at temperatures ranging from 750 to 1000 °C exhibit extreme brittleness, which is another factor that prevents their commercialization.¹¹⁰ It has been reported that the elastic modulus increases as the carbonization temperature increases, due to densification. Therefore, while increasing final pyrolysis temperature of CMSMs yields a more selective membrane, the densification that occurs also compromises the membranes' mechanical properties.¹¹⁰⁻¹¹³ Haraya and colleagues investigated sulfonated poly (phenylene oxide) as a carbon membrane precursor. They found that hollow fiber membranes carbonized at 450 to 600 °C were more flexible compared to those pyrolyzed at 900 °C.¹¹⁰ Specifically, membranes pyrolyzed at 450 °C had an elastic modulus of ~500 MPa, whereas membranes pyrolyzed at 900 °C had an elastic modulus of ~900 MPa. However, there are very few reported studies on the mechanical stability of carbon membranes due to their inherent brittleness.¹¹¹

A comparison of physical aging in CMSMs with that in glassy polymers has led researchers to apply approaches that improve resistance to physical aging in polymers to CMSMs. These approaches, which include polymer backbone design,¹¹³ post-synthetic modification, cross-

linking,^{4, 114-116} heat treatment, blending of nanomaterials,¹¹⁷⁻¹²⁰ and combinations of the above methods,^{4,5,8,52,121-123} can be separated into two primary classes, one which targets the interchain spacing/interactions and the other which alters the rigidity of the polymer chain. However, few have made significant improvements in the degree of aging for the CMSMs being investigated.

One of the aforementioned approaches that made great strides in the reduction of aging in glassy polymers was the incorporation of additives.⁷⁰ For example, the addition of porous additives, such as porous aromatic frameworks (PAFs), prevented aging in poly(1-trimethylsilyl-1-propyne) (PTMSP) and poly(methylpentyne) (PMP).¹²⁴ Bahktin and colleagues showed that portions of the polymer chains were absorbed into the PAF, thus reducing the mobility of the chains and freezing the structure in place. It is well known that aging occurs in glassy polymers due to the rearrangement of polymer segments, which subsequently removes excess FV from within the matrix.^{5,66} It is this reason that led researchers to apply such methods to CMSMs, as the issue involves the collapse of its pore structure, which thereby removes excess FV reducing the membranes performance over time.

Similar to the incorporation of PAFs, zeolitic imidazolate frameworks (ZIFs) and metal organic frameworks (MOFs) have been added to polymeric membranes to reduce aging. Zhang et al. dispersed silica particles in Matrimid[®] 5218 to prevent support densification in CMS hollow fiber membranes.¹³ The permselectivity value obtained for the standard hollow fiber membrane was compared to the membrane containing silica nano-particles. A 580% increase in CO₂ permeance was obtained for the CMSM containing silica nano-particles. The results reveal that the carbon membrane was successfully stabilized against aging through the incorporation of silica particles.¹³ These data suggest that incorporating additives to support the porous structure of CMSMs yields

membranes that not only are resistant to physical aging, but also have superior permeability properties in comparison to pure Matrimid[®] 5218 hollow fiber CMSMs. This approach is one that can be implemented in several systems and may be the key to eliminating physical aging in CMSMs.

A second approach, which involves altering the polymer backbone, has been investigated by several researchers. Amine doping, a form of crosslinking, is an example of this method. Graham et al.¹²⁵ investigated aging associated with a 6FDA:BPDA-DAM precursor, where paraphenylenediamine (PPDA) formed bonds between adjacent carbons, providing the CMSM with a more rigid structure. The incorporation of an amine crosslink was hypothesized to impede the densification of the membrane by preventing relaxation of the CMS structure. However, the permeation data revealed a decrease in permeability and an increase in selectivity (Figure 1.12). It was concluded that while incorporating PPDA changes the permselectivity of the membrane as shown in Figure 1.12, physical aging is still observed. This is most likely due to the reversible nature of the imide to amide bond when heated.

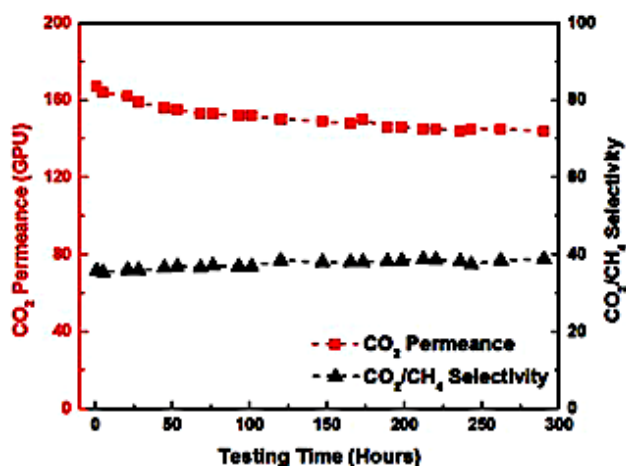


Figure 1.12: Plot of CO₂ permeance and CO₂/CH₄ selectivity against time for a 10 ppm PPDA treated 6FDA:BPDA-DAM CMS fiber, reproduced with permission from Wiley Materials.¹²⁵

Similar results to those observed above are also obtained by doping the pores with oxygen. The dopant blocks the pore structure resulting in a decrease in permeability.¹⁴ This is simply accelerated chemical aging and would not be beneficial for CMSMs in the long term.

A second attempt at crosslinking a CMSM precursor was investigated, the incorporation of a carbon-carbon crosslink versus the carbon-nitrogen crosslink described by Graham et al. revealed much more promising results. Karunaweera et al.⁹² investigated a cross-linkable 6FDA-DABA polyimide (Figure 1.4c) made from the condensation polymerization of (4,4'-hexafluoroisopropylidene) diphthalic anhydride (6FDA) and 3,5-diaminobenzoic acid (DABA). Crosslinking prior to carbonization was hypothesized to yield a more rigid structure in comparison to the pristine polymer.^{122, 127-129} Figure 1.13a,b shows plots of the permselectivities for the non-crosslinked and crosslinked carbon membranes, respectively, over a period of 20 d. The non-crosslinked CMSM showed a 25% decrease in propylene permeability and a 50% decrease for propane. The resulting decrease in permeability was coupled with a 146% increase in

propylene/propane selectivity. In stark comparison, the pre-crosslinked carbon membrane showed only a 2% decrease in propylene permeability with a constant selectivity.

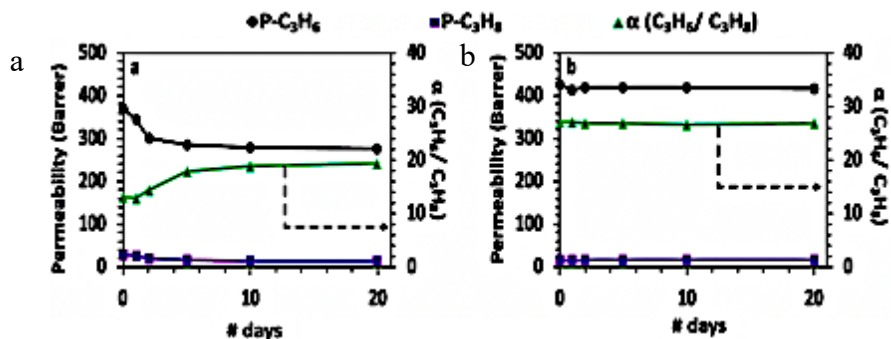


Figure 1.13: Plot of propane (purple) and propylene (black) permeability alongside propane/propylene selectivity against time for (a) 6FDA-DABA, and (b) crosslinked 6FDA-DABA CMSMs, reproduced with permission from Elsevier.⁹²

This anti-aging behavior was attributed to the added rigidity due to crosslinking the polymeric precursor prior to pyrolysis. This is one of the few successes in terms of reducing physical aging. However, it is only applicable for precursors which can be crosslinked, and specifically forming a C-C crosslink. It was previously observed that amine crosslinking did little to prevent the collapse of a porous structure (see Figure 1.12). Therefore, the strength of the bond plays a prominent role.

Lastly, increasing the pyrolysis temperature to fine tune the pore aperture in an effort to target a specific gas pair is also an approach being pursued to reduce physical aging. However, this method is simply another form of accelerated physical aging (Table 1.2). It is believed that by tightening the pores, the rate at which aging occurs will decrease.⁴⁹ However, upon pyrolysis at higher temperatures between 700 and 1000 °C, the CMSM becomes dense, rendering a membrane with permselectivity unacceptably low for gas separations. Recent studies by Qiu et al. purposely

hyperaged CMSMs by heating the membranes between 90 and 250°C.¹²⁶ Their results provide a method to fine tune the macropores (“slit like” pores) of the CMSM by shrinking them through heat treatment.¹²⁶ This post pyrolysis technique allowed for moderate control over the CMSMs pore structure without rendering a dense film, but proved to only benefit small molecules such as hydrogen.¹²⁶

Tracking changes within CMSM structure when transitioning from a freshly carbonized membrane to an aged membrane can prove enlightening. By understanding the mechanism behind physical aging, alternative methods to addressing the issue might be revealed. Lin et al.¹⁰⁶ conducted stability tests on “fresh” CMSMs prepared by pyrolyzing 6FDA-based polyimide polymer films. A 50/50 He/N₂ mixture was used to investigate membrane permeability over a period of 10 days. The permeance for both gases decreased, and the He/N₂ selectivity increased. The changes in permeance were attributed to a reduction in the membrane effective pore size.¹⁰⁶ It was observed that a change in ratio of disordered carbon (D, 1360 cm⁻¹) to graphitic carbon (G, 1580 cm⁻¹) from 1.81 to 1.58 occurred following aging. The results suggested the presence of more graphitic like carbon, however upon aging a CMSM, the carbon and its relative amount of sp² and sp³ carbons will not change. The authors tried to regenerate the membrane’s permeance by heating it to 300 °C for 24 h in a 5% H₂/95% Argon atmosphere.¹⁰⁶ As a result, 83% of the permeance for nitrogen was regained due to the presence of hydrogen which served to reduce the oxygen groups present on the surface. However, a permanent change in the pore structure prevented the full recovery of permeance from occurring.¹⁰⁶

1.5 Future direction in carbon membrane research

Membrane-based separations have been successfully incorporated into several applications. With a heavy focus being placed on natural gas separations, membrane-based technology has made several advancements. CMSMs prepared from a wide range of polymeric precursors have shown permselectivities that surpass current commercially used polymeric membranes such as ethyl cellulose and polysulfone. It is this reason that has led researchers to explore and develop CMSMs that can be used commercially. However, it is through this intensive research and development that several concerns and limitations for CMSMs have come to light.

While CMSMs have high thermal and chemical stability, they undergo several forms of aging quite rapidly. The polymeric precursors used, such as polyimides, have shown astounding permselectivities for multiple gases when converted to CMSMs, however the values obtained begin to alter over time. This change in permselectivity has been attributed to two forms of aging, chemical and physical. While chemical aging has been investigated by researchers leading to promising methods for membrane regeneration after aging, this is not the case for physical aging. Thus, further studies on the development of CMSMs that are resistant to physical aging would be a major breakthrough for membrane-based gas separations and would provide an opportunity for commercialization.

There are some modified polymer precursors that have the potential to overcome physical aging. However, they often come at the expense of the membrane's mechanical stability and/or productivity. It has been hypothesized that carbon membranes that have been prepared at higher pyrolysis temperatures yield smaller pore apertures, making them less susceptible to physical

aging.⁷⁸ However, while this may be true, the brittleness of the membrane, as well as the decline in permeability, all affect its usefulness in terms of being commercialized.

It has also been cited by many researchers in the membrane field that, while the final pyrolysis temperature is important, additional parameters such as the soaking time and heating rate are important as well.¹³⁰ All of the above mentioned parameters can considerably alter the pore structure of the CMSMs, hence altering the rate of physical aging.^{43, 50, 52, 77, 82-88, 131}

Current work has shown the effects of physical aging to be of great concern, with permeabilities for most gases decreasing by roughly 60%. While the effects of physical aging are clear and observed for most carbon membranes, the mechanism by which it occurs is not well understood. Understanding the relationship between polymer precursors and their resulting CMSM, as well as the mechanism by which the unique pore structure is obtained, would greatly enhance the ability to address physical aging.

The use of blended polymers, and the incorporation of inorganic materials, such as carbon nanotubes, zeolitic imidazolate frameworks (ZIFs), and silica, are also methods that show promise in addressing physical aging.¹³²⁻¹³⁵ The incorporation of additives is a method which many have used to address aging within polymeric membranes, and since the aging of carbon membranes is often compared to that of glassy polymers, the concept may yield promising results. The use of additives proved to prevent the collapse of the pore structure thus minimizing the degree of aging. With current carbon membranes showing permeabilities that are significantly higher than the polymeric precursor, a small decrease in the permeability of CMSMs due to physical aging would not prevent them from being commercialized.

The performance of CMSMs is affected by many factors, such as storage environment (e.g., air, humidity, vacuum, inert gas), method of aging (e.g., vacuum, bench top, under pressure), relative humidity, and the length of time between CMSM preparation and testing. These parameters allow for membraneologist to make informed decisions on the preparation of CMSMs.

There are advantages to using CMSMs for gas separation, including their ability to overcome the Robeson upper bound and their exceptional thermal and chemical stability. These attributes will lead to advances in several applications within the gas separation industry. Currently, literature regarding the formation of carbon membranes and how the precursor influences the resulting membrane is limited, as are studies investigating stability and durability. By understanding the mechanism(s) by which physical aging in CMSMs occurs, and overcoming this challenge, it is believed that CMSMs will surpass the limitations of current commercially available polymeric membranes. It is anticipated that the data and results presented within this dissertation will lead researchers to develop a practical carbon membrane for gas separation that will be commercially viable and cost effective for future processes.

1.6 References

1. Lee, P.; Kim, D.; Nam, S.-E.; Bhave, R. R., Carbon molecular sieve membranes on porous composite tubular supports for high performance gas separations. *Microporous and Mesoporous Mater.* 2016, **224**, 332-338.
2. Sazali, N.; Salleh, W. N. W.; Nordin, N. A. H. M.; Ismail, A. F., Matrimid-based carbon tubular membrane: Effect of carbonization environment. *J. Ind. Eng. Chem.* 2015, **32**, 167-171.
3. Cheng, Y.; Wang, Z.; Zhao, D., Mixed matrix membranes for natural gas upgrading: Current status and opportunities. *Ind. Eng. Chem. Res.* 2018, **57** (12), 4139-4169.
4. Smith, S. J. D. et al., Aging in glassy mixed matrix membranes; tuning particle interaction for mechanically robust nanocomposite films. *J. Mater. Chem. A* 2016, **4** (27), 10627-10634.

5. Low, Z.-X.; Budd, P. M.; McKeown, N. B.; Patterson, D. A., Gas permeation properties, physical aging, and its mitigation in high free volume glassy polymers. *Chem. Rev.* 2018, **118** (12), 5871-5911.
6. Galizia, M. et al., 50th anniversary perspective: polymers and mixed matrix membranes for gas and vapor separation: A review and prospective opportunities. *Macromolecules* 2017, **50** (20), 7809-7843.
7. Horn, N. R.; Paul, D. R., Carbon dioxide plasticization and conditioning effects in thick vs. thin glassy polymer films. *Polymer* 2011, **52** (7), 1619-1627.
8. Brunetti, A. et al., Thermally rearranged mixed matrix membranes for CO₂ separation: An aging study. *Int. J. Greenh.* 2017, **61**, 16-26.
9. Sazali, N. et al., Influence of intermediate layers in tubular carbon membrane for gas separation performance. *Int. J. Hydrog. Energy* 2019, **44** (37), 20914-20923.
10. HÄGg, M. B.; Lie, J. A.; LindbrÅThen, A., Carbon molecular sieve membranes. *Ann.. N. Y. Acad. Sci.* 2003, **984** (1), 329-345.
11. Llosa Tanco, M., ; Pacheco Tanaka, David, Recent advances on carbon molecular sieve membranes (CMSMs) and reactors. *Processes* 2016, **4** (29), 2227-9719.
12. Llosa Tanco, M. A.; Pacheco Tanaka, D. A.; Rodrigues, S. C.; Texeira, M.; Mendes, A., Composite-alumina-carbon molecular sieve membranes prepared from novolac resin and boehmite. Part I: Preparation, characterization and gas permeation studies. *Int. J. Hydrog. Energy* 2015, **40** (16), 5653-5663.
13. Zhang, C.; Zhang, K.; Cao, Y.; Koros, W. J., Composite Carbon Molecular Sieve Hollow Fiber Membranes: Resisting Support Densification via Silica Particle Stabilization. *Ind. Eng. Chem. Res.* 2018, **57** (47), 16051-16058.
14. Singh, R.; Koros, W. J., Carbon molecular sieve membrane performance tuning by dual temperature secondary oxygen doping (DTSOD). *J. Membr. Sci.* 2013, **427**, 472-478.
15. Xu, L.; Rungta, M.; Koros, W. J., Matrimid[®] derived carbon molecular sieve hollow fiber membranes for ethylene/ethane separation. *J. Membr. Sci.* 2011, **380** (1), 138-147.
16. Gor, G. Y.; Thommes, M.; Cychosz, K. A.; Neimark, A. V., Quenched solid density functional theory method for characterization of mesoporous carbons by nitrogen adsorption. *Carbon* 2012, **50** (4), 1583-1590.
17. Silvestre-Albero, J.; Silvestre-Albero, A.; Rodríguez-Reinoso, F.; Thommes, M., Physical characterization of activated carbons with narrow microporosity by nitrogen (77.4K), carbon

dioxide (273K) and argon (87.3K) adsorption in combination with immersion calorimetry. *Carbon* 2012, **50** (9), 3128-3133.

18. Neimark, A. V.; Lin, Y.; Ravikovitch, P. I.; Thommes, M., Quenched solid density functional theory and pore size analysis of micro-mesoporous carbons. *Carbon* 2009, **47** (7), 1617-1628.

19. Rao, M. B.; Sircar, S., Performance and pore characterization of nanoporous carbon membranes for gas separation. *J. Membr. Sci.* 1996, **110** (1), 109-118.

20. Sedigh, M. G.; Jahangiri, M.; Liu, P. K. T.; Sahimi, M.; Tsotsis, T. T., Structural characterization of polyetherimide-based carbon molecular sieve membranes. *AIChE Journal* 2000, **46** (11), 2245-2255.

21. Sanyal, O. et al., Next generation membranes —using tailored carbon. *Carbon* 2018, **127**, 688-698.

22. Saufi, S. M.; Ismail, A. F., Fabrication of carbon membranes for gas separation—a review. *Carbon* 2004, **42** (2), 241-259.

23. Geiszler, V. C.; Koros, W. J., Effects of polyimide pyrolysis conditions on carbon molecular sieve membrane properties. *Ind. Eng. Chem. Res.* 1996, **35** (9), 2999-3003.

24. Centeno, T. A.; Vilas, J. L.; Fuertes, A. B., Effects of phenolic resin pyrolysis conditions on carbon membrane performance for gas separation. *J. Membr. Sci.* 2004, **228** (1), 45-54.

25. Schimmelpfennig, S.; Glaser, B., One step forward toward characterization: some important material properties to distinguish biochars. *J. Environ. Qual.* 2012, **41** (4), 1001-1013.

26. Ruz, P.; et al., Structural evolution of turbostratic carbon: Implications in H₂ storage. *Solid State Sci.* 2016, **62**, 105-111.

27. Wollbrink, A. et al., Amorphous, turbostratic and crystalline carbon membranes with hydrogen selectivity. *Carbon* 2016, **106**, 93-105.

28. Barsema, J. N. et al., Intermediate polymer to carbon gas separation membranes based on Matrimid PI. *J. Membr. Sci.* 2004, **238** (1), 93-102.

29. Han, S. H.; Kim, G. W.; Jung, C. H.; Lee, Y. M., Control of pore characteristics in carbon molecular sieve membranes (CMSM) using organic/inorganic hybrid materials. *Desalination* 2008, **233** (1), 88-95.

30. Lagorsse, S.; Campo, M. C.; Magalhães, F. D.; Mendes, A., Water adsorption on carbon molecular sieve membranes: Experimental data and isotherm model. *Carbon* 2005, **43** (13), 2769-2779.

31. Xu, L. et al., Physical aging in carbon molecular sieve membranes. *Carbon* 2014, **80**, 155-166.
32. Rowe, B. W.; Freeman, B. D.; Paul, D. R., Influence of previous history on physical aging in thin glassy polymer films as gas separation membranes. *Polymer* 2010, **51** (16), 3784-3792.
33. Wieneke, J. U.; Staudt, C., Thermal stability of 6FDA-(co-)polyimides containing carboxylic acid groups. *Polym. Degrad. Stab.* 2010, **95** (4), 684-693.
34. Luo, S.; Wiegand, J. R.; Gao, P.; Doherty, C. M.; Hill, A. J.; Guo, R., Molecular origins of fast and selective gas transport in pentiptycene-containing polyimide membranes and their physical aging behavior. *J. Membr. Sci.* 2016, **518**, 100-109.
35. Staiger, C. L.; Pas, S. J.; Hill, A. J.; Cornelius, C. J., Gas separation, free volume distribution, and physical aging of a highly microporous spirobisindane polymer. *Chem. Mater.* 2008, **20** (8), 2606-2608.
36. Lagorsse, S.; Magalhães, F. D.; Mendes, A., Aging study of carbon molecular sieve membranes. *J. Membr. Sci.* 2008, **310** (1), 494-502.
37. Verma, S. K.; Walker Jr, P. L., Carbon molecular sieves with stable hydrophobic surfaces. *Carbon* 1992, **30** (6), 837-844.
38. Hays, S. S.; Sanyal, O.; Leon, N. E.; Arab, P.; Koros, W. J., Envisioned role of slit bypass pores in physical aging of carbon molecular sieve membranes. *Carbon* 2020, **157**, 385-394.
39. Robeson, L. M., The upper bound revisited. *J. Membr. Sci.* 2008, **320** (1), 390-400.
40. Behnia, N.; Pirouzfard, V., Effect of operating pressure and pyrolysis conditions on the performance of carbon membranes for CO₂/CH₄ and O₂/N₂ separation derived from polybenzimidazole/Matrimid and UIP-S precursor blends. *Polym. Bull. (Heidelberg, Ger.)* 2018, **75** (10), 4341-4358.
41. Jiao, W.; Ban, Y.; Shi, Z.; Jiang, X.; Li, Y.; Yang, W., Gas separation performance of supported carbon molecular sieve membranes based on soluble polybenzimidazole. *J. Membr. Sci.* 2017, **533**, 1-10.
42. Karunaweera, C.; Ferraris, J. P.; Balkus, K. J.; Musselman, I. H.; Panapitiya, N. P., Compatibilized immiscible polymer blends and their carbonization for gas separation applications. *J. Am. Chem. Soc.* 2016, **9** (8), 643.
43. Hosseini, S. S. et al., Enhancing the properties and gas separation performance of PBI-polyimides blend carbon molecular sieve membranes via optimization of the pyrolysis process. *Sep. Purif. Technol.* 2014, **122**, 278-289.

44. Rungta, M. et al., Carbon molecular sieve structure development and membrane performance relationships. *Carbon* 2017, **115**, 237-248.
45. Sazali, N.; Salleh, W. N. W.; Nordin, N. A. H. M.; Harun, Z.; Ismail, A. F., Matrimid-based carbon tubular membranes: The effect of the polymer composition. *J. Appl. Polym. Sci.* 2015, **132** (33), 42394.
46. Ning, X.; Koros, W. J., Carbon molecular sieve membranes derived from Matrimid[®] polyimide for nitrogen/methane separation. *Carbon* 2014, **66**, 511-522.
47. Kamath, M. G.; Fu, S.; Itta, A. K.; Qiu, W.; Liu, G.; Swaidan, R.; Koros, W. J., 6FDA-DETDA: DABE polyimide-derived carbon molecular sieve hollow fiber membranes: Circumventing unusual aging phenomena. *J. Membr. Sci.* 2018, **546**, 197-205.
48. Fu, S. et al., The significance of entropic selectivity in carbon molecular sieve membranes derived from 6FDA/DETDA:DABA(3:2) polyimide. *J. Membr. Sci.* 2017, **539**, 329-343.
49. Fu, S.; Wenz, G. B.; Sanders, E. S.; Kulkarni, S. S.; Qiu, W.; Ma, C.; Koros, W. J., Effects of pyrolysis conditions on gas separation properties of 6FDA/DETDA:DABA(3:2) derived carbon molecular sieve membranes. *J. Membr. Sci.* 2016, **520**, 699-711.
50. Bhuwania, N. et al., Engineering substructure morphology of asymmetric carbon molecular sieve hollow fiber membranes. *Carbon* 2014, **76**, 417-434.
51. Salleh, W. N. W.; Ismail, A. F., Carbon membranes for gas separation processes: Recent progress and future perspective. *J. Membr. Sci.* 2015, **1** (Issue 1), 2-15.
52. Hosseini, S. S.; Chung, T. S., Carbon membranes from blends of PBI and polyimides for N₂/CH₄ and CO₂/CH₄ separation and hydrogen purification. *J. Membr. Sci.* 2009, **328** (1), 174-185.
53. Murphy, T. M.; Freeman, B. D.; Paul, D. R., Physical aging of polystyrene films tracked by gas permeability. *Polymer* 2013, **54** (2), 873-880.
54. Kumar, S. K.; Benicewicz, B. C.; Vaia, R. A.; Winey, K. I., 50th anniversary perspective: Are polymer nanocomposites practical for applications? *Macromolecules* 2017, **50** (3), 714-731.
55. Lau, C. H. et al., Ending aging in super glassy polymer membranes. *Angew. Chem., Int. Ed.* 2014, **53** (21), 5322-5326.
56. Hayashi, J.-i.; Mizuta, H.; Yamamoto, M.; Kusakabe, K.; Morooka, S., Pore size control of carbonized BPDA-pp' ODA polyimide membrane by chemical vapor deposition of carbon. *J. Membr. Sci.* 1997, **124** (2), 243-251.

57. Shamsabadi, A. A.; Behbahani, R. M.; Seidi, F.; Soroush, M., Physical aging of polyetherimide membranes. *J. Nat. Gas Sci. Eng.* 2015, **27**, 651-660.
58. Yong, W. F.; Kwek, K. H. A.; Liao, K.-S.; Chung, T.-S., Suppression of aging and plasticization in highly permeable polymers. *Polymer* 2015, **77**, 377-386.
59. Mueller, N.; Handge, U. A.; Abetz, V., Physical ageing and lifetime prediction of polymer membranes for gas separation processes. *J. Membr. Sci.* 2016, **516**, 33-46.
60. Xia, J.; Chung, T.-S.; Paul, D. R., Physical aging and carbon dioxide plasticization of thin polyimide films in mixed gas permeation. *J. Membr. Sci.* 2014, **450**, 457-468.
61. Rezac, M. E.; Pfromm, P. H.; Costello, L. M.; Koros, W. J., Aging of thin polyimide-ceramic and polycarbonate-ceramic composite membranes. *Ind. Eng. Chem. Res.* 1993, **32** (9), 1921-6.
62. Ogieglo, W.; Puspasari, T.; Ma, X.; Pinnau, I., Sub-100 nm carbon molecular sieve membranes from a polymer of intrinsic microporosity precursor: Physical aging and near-equilibrium gas separation properties. *J. Membr. Sci.* 2020, **597**, 117752.
63. Ogieglo, W.; Furchner, A.; Ma, X.; Hazazi, K.; Alhazmi, A. T.; Pinnau, I., Thin composite carbon molecular sieve membranes from a polymer of intrinsic microporosity precursor. *ACS Appl. Mater. Interfaces* 2019, **11** (20), 18770-18781.
64. Ma, X.; Pinnau, I., Effect of film thickness and physical aging on “intrinsic” gas permeation properties of microporous ethanoanthracene-based polyimides. *Macromolecules* 2018, **51** (3), 1069-1076.
65. Kocherlakota, L. S.; Knorr, D. B.; Foster, L.; Overney, R. M., Enhanced gas transport properties and molecular mobilities in nano-constrained poly[1-(trimethylsilyl)-1-propyne] membranes. *Polymer* 2012, **53** (12), 2394-2401.
66. Yavari, M.; Maruf, S.; Ding, Y.; Lin, H., Physical aging of glassy perfluoropolymers in thin film composite membranes. Part II. Glass transition temperature and the free volume model. *J. Membr. Sci.* 2017, **525**, 399-408.
67. Russell, T. P.; Chai, Y., 50th anniversary perspective: putting the squeeze on polymers: A perspective on polymer thin films and interfaces. *Macromolecules* 2017, **50** (12), 4597-4609.
68. Zhuang, G.-L.; Wey, M.-Y.; Tseng, H.-H., Effect of copolymer microphase-separated structures on the gas separation performance and aging properties of SBC-derived membranes. *J. Membr. Sci.* 2017, **529**, 63-71.
69. McKenna, G. B.; Simon, S. L., 50th anniversary perspective: challenges in the dynamics and kinetics of glass-forming polymers. *Macromolecules* 2017, **50** (17), 6333-6361.

70. Kocherlakota, L. S.; Pham, T.; Overney, R. M., Transport and stability enhancement in interfacially and dimensionally constrained CO₂ selective polymers embedded in nanoporous sieve membranes. *Polymer* 2013, **54** (21), 5986-5992.
71. Omidvar, M. et al., Unexpectedly strong size-sieving ability in carbonized polybenzimidazole for membrane H₂/CO₂ Separation. *ACS Appl. Mater. Interfaces* 2019, **11** (50), 47365-47372.
72. Murphy, T. M. et al., Physical aging of layered glassy polymer films via gas permeability tracking. *Polymer* 2011, **52** (26), 6117-6125.
73. Schuepfer, D. B. et al., Assessing the structural properties of graphitic and non-graphitic carbons by Raman spectroscopy. *Carbon* 2020, **161**, 359-372.
74. Tseng, H.-H.; Zhuang, G.-L.; Lin, M.-D.; Chang, S.-H.; Wey, M.-Y., The influence of matrix structure and thermal annealing-hydrophobic layer on the performance and durability of carbon molecular sieving membrane during physical aging. *J. Membr. Sci.* 2015, **495**, 294-304.
75. Campo, M. C.; Magalhães, F. D.; Mendes, A., Carbon molecular sieve membranes from cellophane paper. *J. Membr. Sci.* 2010, **350** (1), 180-188.
76. Haider, S.; Lindbråthen, A.; Lie, J. A.; Hägg, M.-B., Carbon membranes for oxygen enriched air – Part I: Synthesis, performance and preventive regeneration. *Sep. Purif. Technol.* 2018, **204**, 290-297.
77. Menendez, I.; Fuertes, A. B., Aging of carbon membranes under different environments. *Carbon* 2001, **39** (5), 733-740.
78. Salinas, O.; Ma, X.; Litwiller, E.; Pinnau, I., High-performance carbon molecular sieve membranes for ethylene/ethane separation derived from an intrinsically microporous polyimide. *J. Membr. Sci.* 2016, **500**, 115-123.
79. Koresh, J.; Soffer, A., Study of molecular sieve carbons. Part 1.—Pore structure, gradual pore opening and mechanism of molecular sieving. *J. Chem. Soci., Faraday Transactions 1: Phys. Chem.* 1980, **76** (0), 2457-2471.
80. Suda, H.; Haraya, K., Molecular sieving effect of carbonized kapton polyimide membrane. *J. Chem. Soci. Chem. Comm.* 1995, **11**, 1179-1180.
81. Petersen, J.; Matsuda, M.; Haraya, K., Capillary carbon molecular sieve membranes derived from Kapton for high temperature gas separation. *J. Membr. Sci.* 1997, **131** (1), 85-94.
82. Shao, L.; Chung, T. S.; Pramoda, K. P., The evolution of physicochemical and transport properties of 6FDA-durene toward carbon membranes; from polymer, intermediate to carbon. *Microporous and Mesoporous Mater.* 2005, **84** (1-3), 59-68.

83. Shao, L.; Chung, T.-S.; Wensley, G.; Goh, S. H.; Pramoda, K. P., Casting solvent effects on morphologies, gas transport properties of a novel 6FDA/PMDA–TMMDA copolyimide membrane and its derived carbon membranes. *J. Membr. Sci.* 2004, **244** (1), 77-87.
84. Tin, P. S.; Chung, T.-S.; Liu, Y.; Wang, R., Separation of CO₂/CH₄ through carbon molecular sieve membranes derived from P84 polyimide. *Carbon* 2004, **42** (15), 3123-3131.
85. Suda, H.; Haraya, K., Gas permeation through micropores of carbon molecular sieve membranes derived from Kapton polyimide. *J. Phys. Chem. B* 1997, **101** (20), 3988-3994.
86. Schindler, E.; Maier, F., Manufacture of porous carbon membranes. United States Patent 4919860, 1990.
87. Salinas, O.; Ma, X.; Litwiller, E.; Pinnau, I., Ethylene/ethane permeation, diffusion and gas sorption properties of carbon molecular sieve membranes derived from the prototype ladder polymer of intrinsic microporosity (PIM-1). *J. Membr. Sci.* 2016, **504**, 133-140.
88. Steel, K. M.; Koros, W. J., Investigation of porosity of carbon materials and related effects on gas separation properties. *Carbon* 2003, **41** (2), 253-266.
89. Liao, K.-S. et al., Microstructure of carbon molecular sieve membranes and their application to separation of aqueous bioethanol. *Carbon* 2012, **50** (11), 4220-4227.
90. Knight, D. S.; White, W. B., Characterization of diamond films by Raman spectroscopy. *J. Mater. Res.* 2011, **4** (2), 385-393.
91. Wang, Y.; Alsmeyer, D. C.; McCreery, R. L., Raman spectroscopy of carbon materials: structural basis of observed spectra. *Chem. Mater.* 1990, **2** (5), 557-563.
92. Karunaweera, C.; Musselman, I. H.; Balkus, K. J.; Ferraris, J. P., Fabrication and characterization of aging resistant carbon molecular sieve membranes for C₃ separation using high molecular weight crosslinkable polyimide, 6FDA-DABA. *J. Membr. Sci.* 2019, **581**, 430-438.
93. Shimodaira, N.; Masui, A., Raman spectroscopic investigations of activated carbon materials. *J. Appl. Phys.* 2002, **92** (2), 902-909.
94. Song, C.; Wang, T.; Qiu, Y.; Qiu, J.; Cheng, H., Effect of carbonization atmosphere on the structure changes of PAN carbon membranes. *J. Porous Mater.* 2009, **16** (2), 197-203.
95. Escribano, R.; Sloan, J. J.; Siddique, N.; Sze, N.; Dudev, T., Raman spectroscopy of carbon-containing particles. *Vib. Spectrosc.* 2001, **26** (2), 179-186.
96. Knight, D. S.; White, W. B., Characterization of diamond films by Raman spectroscopy. *J. Mater. Res.* 1989, **4** (2), 385-93.

97. Kim, H. J. et al., A carbonaceous membrane based on a polymer of intrinsic microporosity (PIM-1) for water treatment. *Sci. Rep.* 2016, **6**, 36078.
98. Jones, C. W.; Koros, W. J., Carbon molecular sieve gas separation membranes-II. Regeneration following organic exposure. *Carbon* 1994, **32** (8), 1427-1432.
99. Vu, D. Q.; Koros, W. J.; Miller, S. J., Effect of condensable impurity in CO₂/CH₄ gas feeds on performance of mixed matrix membranes using carbon molecular sieves. *J. Membr. Sci.* 2003, **221** (1), 233-239.
100. Lie, J. A.; Hägg, M. B., Carbon membranes from cellulose: Synthesis, performance and regeneration. *J. Membr. Sci.* 2006, **284** (1-2), 79-86.
101. Adams, J. S. et al., New insights into structural evolution in carbon molecular sieve membranes during pyrolysis. *Carbon* 2019, **141**, 238-246.
102. Tin, P. S.; Chung, T.-S.; Hill, A. J., Advanced fabrication of carbon molecular sieve membranes by nonsolvent pretreatment of precursor polymers. *Ind. Eng. Chem. Res.* 2004, **43** (20), 6476-6483.
103. Hu, C.-P. et al., The gas separation performance adjustment of carbon molecular sieve membrane depending on the chain rigidity and free volume characteristic of the polymeric precursor. *Carbon* 2018, **143**, 343-351.
104. Xu, L.; Rungta, M.; Brayden, M. K.; Martinez, M. V.; Stears, B. A.; Barbay, G. A.; Koros, W. J., Olefins-selective asymmetric carbon molecular sieve hollow fiber membranes for hybrid membrane-distillation processes for olefin/paraffin separations. *J. Membr. Sci.* 2012, **424**, 314-323.
105. Kim, S.-J.; Lee, P. S.; Chang, J.-S.; Nam, S.-E.; Park, Y.-I., Preparation of carbon molecular sieve membranes on low-cost alumina hollow fibers for use in C₃H₆/C₃H₈ separation. *Sep. Purif. Technol.* 2018, **194**, 443-450.
106. Ma, X.; Williams, S.; Wei, X.; Kniep, J.; Lin, Y. S., Propylene/propane mixture separation characteristics and stability of carbon molecular sieve membranes. *Ind. Eng. Chem. Res.* 2015, **54** (40), 9824-9831.
107. Fu, S.; Sanders, E. S.; Kulkarni, S. S.; Wenz, G. B.; Koros, W. J., Temperature dependence of gas transport and sorption in carbon molecular sieve membranes derived from four 6FDA based polyimides: Entropic selectivity evaluation. *Carbon* 2015, **95**, 995-1006.
108. Hu, C.-P.; Polintan, C. K.; Tayo, L. L.; Chou, S.-C.; Tsai, H.-A.; Hung, W.-S.; Hu, C.-C.; Lee, K.-R.; Lai, J.-Y., The gas separation performance adjustment of carbon molecular sieve

membrane depending on the chain rigidity and free volume characteristic of the polymeric precursor. *Carbon* 2019, **143**, 343-351.

109. Saufi, S. M.; Ismail, A. F., Development and characterization of polyacrylonitrile (PAN) based carbon hollow fiber membrane. *Songklanakarin J. Sci. Technol* 2002, **24**, 843-854.

110. Yoshimune, M.; Haraya, K., Flexible carbon hollow fiber membranes derived from sulfonated poly(phenylene oxide). *Sep. Purif. Technol.* 2010, **75** (2), 193-197.

111. Tanihara, N. et al., Gas permeation properties of asymmetric carbon hollow fiber membranes prepared from asymmetric polyimide hollow fiber. *J. Membr. Sci.* 1999, **160** (2), 179-186.

112. Yao, J.; Yu, W., Tensile strength and its variation for PAN-based carbon fibers. II. calibration of the variation from testing. *J. Appl. Polym. Sci.* 2007, **104** (4), 2625-2632.

113. Sedghi, A.; Farsani, R. E.; Shokuhfar, A., The effect of commercial polyacrylonitrile fibers characterizations on the produced carbon fibers properties. *J. Mater. Process. Technol.* 2008, **198** (1), 60-67.

114. Hernández-Martínez, H.; et al., Simultaneous thermal cross-linking and decomposition of side groups to mitigate physical aging in poly(oxyindole biphenylene) gas separation membranes. *Ind. Eng. Chem. Res.* 2018, **57** (13), 4640-4650.

115. Cao, P.-F. et al., Robust and elastic polymer membranes with tunable properties for gas separation. *ACS Appl. Mater. Interfaces* 2017, **9** (31), 26483-26491.

116. Liu, S. et al., Gas permeation properties of carbon molecular sieve membranes derived from novel poly(phthalazinone ether sulfone ketone). *Ind. Eng. Chem. Res.* 2008, **47** (3), 876-880.

117. Olivieri, L. et al., Reducing ageing of thin PTMSP films by incorporating graphene and graphene oxide: Effect of thickness, gas type and temperature. *J. Membr. Sci.* 2018, **555**, 258-267.

118. Mitra, T.; Bhavsar, R. S.; Adams, D. J.; Budd, P. M.; Cooper, A. I., PIM-1 mixed matrix membranes for gas separations using cost-effective hypercrosslinked nanoparticle fillers. *Chem. Commun. (Cambridge, U. K.)* 2016, **52** (32), 5581-5584.

119. Rao, P. S.; Wey, M.-Y.; Tseng, H.-H.; Kumar, I. A.; Weng, T.-H., A comparison of carbon/nanotube molecular sieve membranes with polymer blend carbon molecular sieve membranes for the gas permeation application. *Microporous and Mesoporous Mater.* 2008, **113** (1-3), 499-510.

120. Park, H. B.; Suh, I. Y.; Lee, Y. M., Novel pyrolytic carbon membranes containing silica: preparation and characterization. *Chem. Mater.* 2002, **14** (7), 3034-3046.

121. Wang, Z.; Ren, H.; Zhang, S.; Zhang, F.; Jin, J., Polymers of intrinsic microporosity/metal-organic framework hybrid membranes with improved interfacial interaction for high-performance CO₂ separation. *J. Mater. Chem. A* 2017, **5** (22), 10968-10977.
122. Qiu, W.; et al., Sub-T_g cross-linking of a polyimide membrane for enhanced CO₂ plasticization resistance for natural gas separation. *Macromolecules* 2011, **44** (15), 6046-6056.
123. Kim, Y. K.; Park, H. B.; Lee, Y. M., Carbon molecular sieve membranes derived from thermally labile polymer containing blend polymers and their gas separation properties. *J. Membr. Sci.* 2004, **243** (1), 9-17.
124. Golubev, G. S.; et al., A novel hybrid material based on polytrimethylsilylpropyne and hypercrosslinked polystyrene for membrane gas separation and thermopervaporation. *Pet. Chem.* 2017, **57** (6), 498-510.
125. Wenz, G. B.; Koros, W. J., Tuning carbon molecular sieves for natural gas separations: A diamine molecular approach. *AIChE Journal* 2017, **63** (2), 751-760.
126. Qiu, W.; et al., Hyperaging tuning of a carbon molecular sieve hollow fiber membrane with extraordinary gas separation performance and stability. *Angew. Chem. Int. Ed.* 2019, **58**, 11700.
127. Kratochvil, A. M.; Koros, W. J., Decarboxylation-induced cross-linking of a polyimide for enhanced CO₂ plasticization resistance. *Macromolecules* 2008, **41** (21), 7920-7927.
128. Qiu, W.; Zhang, K.; Li, F. S.; Zhang, K.; Koros, W. J., Gas separation performance of carbon molecular sieve membranes based on 6FDA-mPDA/DABA (3: 2) Polyimide. *Sus. Chem.* 2014, **7** (4), 1186-1194.
129. Tian, Z.; Cao, B.; Li, P., Effects of sub-T_g cross-linking of triptycene-based polyimides on gas permeation, plasticization resistance and physical aging properties. *J. Membr. Sci.* 2018, **560**, 87-96.
130. Shin, J. H. et al., Fluorine-containing polyimide/polysilsesquioxane carbon molecular sieve membranes and techno-economic evaluation thereof for C₃H₆/C₃H₈ separation. *J. Membr. Sci.* 2020, **598**, 117660.
131. Fitzer, E.; Frohs, W.; Heine, M., Optimization of stabilization and carbonization treatment of PAN fibres and structural characterization of the resulting carbon fibres. *Carbon* 1986, **24** (4), 387-395.
132. Park, H. B.; Lee, Y. M., Pyrolytic carbon-silica membrane: a promising membrane material for improved gas separation. *J. Membr. Sci.* 2003, **213** (1), 263-272.

133. Kratzer, D. W.; Kosuri, M. R.; Ma, C. Composite carbon molecular sieve membranes having anti-substructure collapse particles loaded in a core thereof. WO2016085974A1, 2016.
134. Hulicova, D.; Oya, A., The polymer blend technique as a method for designing fine carbon materials. *Carbon* 2003, **41** (7), 1443-1450.
135. Lee, H.-J.; Suda, H.; Haraya, K.; Moon, S.-H., Gas permeation properties of carbon molecular sieving membranes derived from the polymer blend of polyphenylene oxide (PPO)/polyvinylpyrrolidone (PVP). *J. Membr. Sci.* 2007, **296** (1), 139-146.

CHAPTER 2
AGE REDUCTION IN HIGHLY POROUS CARBON MOLECULAR
SIEVE MEMBRANES

Authors- Whitney K. Cosey, Kenneth J. Balkus, Jr. , John P. Ferraris, Inga H. Musselman*

Department of Chemistry and Biochemistry, BE 26

The University of Texas at Dallas

800 W. Campbell Road

Richardson, TX 75080-3021

¹ Manuscript title 'Age Reduction in Highly Porous Carbon Molecular Sieve Membranes' is in preparation to submit to *Journal of the American Chemical Society*

2.1 Abstract

Carbon molecular sieve membranes (CMSMs) commonly lose permeability over time due to the collapse of micropores. This decline in permeability, due to the densification of the membrane, is known as physical aging. CMSMs derived from polymers of intrinsic microporosity (PIM-1) are highly affected by physical aging, with declines in permeability greater than 60% over time. It is hypothesized that the densification of CMSMs derived from this high free volume polymer precursor is thermodynamically driven by the collapse of large unconnected graphene domains to reach a more stable conformation (i.e., graphite). This study describes a novel strategy to mitigate physical aging by pillaring the CMSM using copper nanoparticles. Highly soluble metal organic polyhedra-18 (MOP-18) was introduced into polymer of intrinsic microporosity-1 (PIM-1) with loadings up to 40 wt/wt to form a mixed-matrix membrane (MMM). Pyrolysis of the MMM at 550 °C resulted in the in-situ formation of copper metal nanoparticles that acted as pillars for the graphene sheets within the CMSM, preventing the collapse of the micropores thus minimizing the aging of the CMSM. Single gas permeation measurements of CO₂ and CH₄ were made on the pristine polymer derived CMSM and the copper-pillared CMSM at 35 °C and 2 bar to confirm the membranes' resistance to physical aging. The CH₄ permeability for the PIM-1 CMSM decreased by 70%, from 93 to 27 Barrers, over a period of 7 d, while remarkably the pillared PIM-1 CMSM showed essentially no decline in CH₄ permeability. This research demonstrates a universal approach to reducing physical aging in CMSMs.

2.2 Introduction

Current CO₂ emissions from fossil fuels and natural gas processing make up approximately 65% of the total greenhouse gases emitted globally.^{1,2} In recent years, more focus has been placed on the separation and capture of CO₂ in order to combat the effects of global warming. Membrane-based gas separation provides a cost-effective method to separate CO₂. However, with CO₂ emissions steadily rising each year, it is imperative that the efficiency of these separations is improved. Carbon molecular sieve membranes (CMSMs) have gained attention in this regard, due to their unique pore structure and surface area.^{3,4} CMSMs are composed of both ultra-micropores (<0.7 nm) and micropores (0.7-2 nm), which provide the membrane with high selectivity and permeability, respectively.⁵ Their inherent pore size distribution also allows them to surpass the performance of polymeric membranes used for gas separations.⁶ Despite this improved permselectivity^{4,5,7}, CMSMs are subject to physical and chemical aging.^{4,8-10} Chemical aging is the result of chemisorption and physisorption of unwanted species in and on the membrane, causing a decline in permeability.^{11,12} In contrast, physical aging results from the collapse of the membrane pore structure and subsequent densification.^{12,13} Physical aging, unlike chemical aging, cannot be reversed to regenerate the initial or “fresh” permselectivity.^{11,14} Therefore, controlling the CMSM pore structure following pyrolysis has become the focus of several research groups. Altering the carbonization procedure by either adjusting the final pyrolysis temperature or the soak time allows for a reduction in physical aging, however it also results in a subsequent decline in the permeability.¹⁵⁻¹⁷ This method also tends to cause a decline in the mechanical stability of the membrane, resulting in more brittle materials. A second approach, which has shown promising results is to crosslink the polymer precursor prior to carbonization.¹⁸ However, this method is

dependent on, and thus limited by, the polymer's functionality. A more efficient approach would be to stabilize the pore structure of the CMSM by incorporating a support system that would remain after pyrolysis. Nakagawa and colleagues' tactic of crosslinking ion exchange resins using metal cations provides a pathway to stabilize CMSMs by introducing metal pillars.¹⁹ The approach described below incorporates an additive into the polymer precursor, which forms metal nanoparticles after pyrolysis to pillar the pore structure, preventing the densification of the membrane. This technique provides a means to reduce physical aging without sacrificing the permselectivity of the membrane. It also has the benefit of being independent of the polymer precursor's functionality, making it a more general approach to stabilizing CMSMs.

A mixed-matrix membrane (MMM) composed of metal organic polyhedra-18 (MOP-18) and PIM-1 was prepared.²⁰ The rigid backbone of PIM-1 reduces the flexibility of the polymer, preventing the polymer from packing efficiently.²¹⁻²³ This rigidity translates to an inability to stack into graphitic sheets upon carbonization, which results in turbostratic carbon with a higher content of sp^3 terminal sites. This is a common feature for CMSMs derived from high free volume polymers, and is accompanied by high, but unstable, permeability due to physical aging.²⁵ PIM-1 is comprised of fused rings with spiro-centers as shown in Fig. 1a.^{21,26} The metal-organic polyhedra-18 (MOP-18) is composed of discrete porous molecular cages making it easily dispersed in a polymer matrix (Figure 2.1b).^{21,27,28} MOP-18 has an alkyl chain-to-chain diameter of ~ 50 Å. The center-to-center distance between neighboring polyhedra is ~ 24 Å. Unlike simple metal salts, MOP-18 does not crosslink the polymer to become insoluble. The pyrolysis of the PIM-1-based

MMM results in the in-situ formation of copper nanoparticles, which provide a stable scaffold for the inherent pore structure of the resultant CMSM.

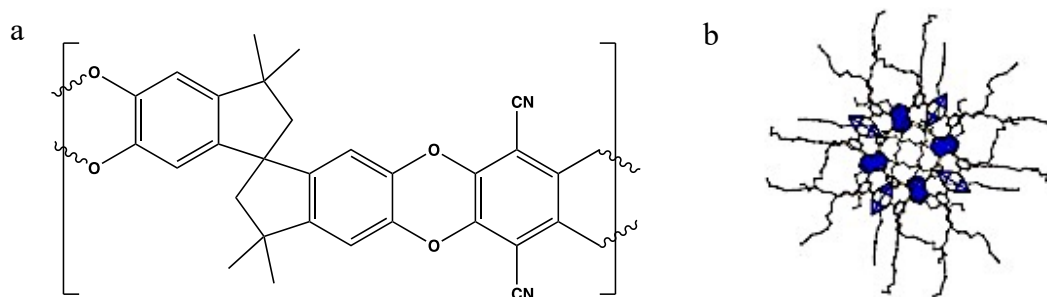


Figure 2.1: (a) Chemical structure of PIM-1, and (b) MOP-18
Blue represents the copper paddle wheels, and the black and red spheres denotes the 12 C-chain and oxygen, respectively.

In this study, the CMSM was prepared by the pyrolysis of a 40 wt/wt MOP-18/PIM-1 MMM (details in methods). We show that uniformly dispersed copper nanoparticles (CuNPs) are capable of suppressing physical aging within CMSMs. We believe that this result provides a significant contribution to the membrane field, as it represents a more general approach to stabilizing CMSMs.

2.3 Experimental

2.3.1 Materials

PIM-1: 5,5',6,6'-tetrahydroxy-3,3,3',3'-tetramethyl-1,1'-spirobisindane (TTSBI) (96%, Sigma Aldrich) was recrystallized using methanol and dichloromethane to purify the material. Tetrafluoroterephthalonitrile (99%, Sigma Aldrich) was purified by vacuum sublimation at 140°C. DMF (99.8%, Sigma Aldrich) was dried over 4A 4-8 mesh (Sigma-Aldrich) molecular sieves, and anhydrous potassium carbonate (98%, Sigma Aldrich) was dried at 60°C for 1 d to ensure no water was present. Purification procedures are described in detail elsewhere.²⁶

MOP-18: The following materials were purchased from Sigma Aldrich with purities greater than 97%: sodium bicarbonate, 1-iodododecane, 5-hydroxyisophthalic acid, copper acetate monohydrate, ethyl acetate, acetonitrile, potassium hydroxide, methanol, tetrachloroethane, and chloroform. Ethyl ether (99.9%), and hydrochloric acid were purchased from J.T. Baker. Concentrated sulfuric acid was purchased from Mallinckrodt. Methanol, acetonitrile, and DMF were dried prior to use over 4A molecular sieves.

2.3.2 Polymer Synthesis

PIM-1 was synthesized using reported procedures.²⁶ Producing a high molecular weight PIM-1 required a reactant ratio for tetrahydroxytetramethylspirobisindane (TTSBI), 1,4-dicyanotetrafluorobenzene, (DCTB), and anhydrous K_2CO_3 of 1:1:2, respectively. The monomers were purified prior to synthesis as described above in the materials section. Anhydrous K_2CO_3 (4.2 g, 30 mmol), TTSBI (5.1 g, 15 mmol), and DCTB (3.0 g, 15 mmol) were dissolved in anhydrous DMF (100 mL) and magnetically stirred in a 250 mL flask. The reaction flask was sealed with a septum so that air could be removed by application of vacuum and replaced with N_2 gas; this process was repeated 4x. The reaction flask was then stirred magnetically (810 rpm) at 55°C for 23 h. Upon cooling, 150 mL of deionized water was added to the mixture, and the product was collected by filtration. A 75% yield of the neon yellow polymer (PIM-1) was obtained after drying at 90°C for 1 d (M_w 60, 000 and PDI of 2 by GPC).

2.3.3 MOP-18 synthesis

First, the MOP-18 linker, 5-dodecoxyisophthalic acid, was prepared by esterifying 5-hydroxyisophthalic acid with ethanol. Alkylation of the hydroxyl group of the diester, followed

by hydrolysis, yielded 5-dodecoxyisophthalic acid. Then, two solutions were prepared. The linker (2.7 g) was dissolved in 100 mL of hot (80 °C) DMF and stirred until a clear solution was obtained. Copper acetate (1.5 g) was dissolved in 50 mL of DMF and stirred at room temperature until fully dissolved. The two solutions were combined, and 100 mL of methanol was added. The precipitate was allowed to crystallize for 24 h at room temperature, and then was washed 2x with methanol, filtered, and dried in a vacuum oven at 60 °C for 24 h to yield blue MOP-18 crystals (93% yield). A more detailed synthesis may be found elsewhere.^{20, 27}

2.3.4 Membrane preparation

Fabrication of precursor polymeric membranes- Solutions for 40 wt/wt MOP-18/PIM-1 MMMs membranes were prepared by first dissolving 0.5 g of PIM-1 in 4 g of C₂H₂Cl₄ and 0.2 g of MOP-18 in 3 g of C₂H₂Cl₄ in separate scintillation vials. These solutions were stirred for 24 h and then combined. The combined solution was stirred for an additional 24 h. After thorough mixing (clear blue/green solution), the solution was concentrated by evaporating solvent until the polymer concentration reached 15 wt%. Pristine PIM-1 membranes were prepared by dissolving 0.5 g of PIM-1 into 3.3 g C₂H₂Cl₄. The solution was stirred for 24 h at room temperature. A Sheen 1133N automatic applicator with a doctor blade was used to cast the membranes onto a glass substrate. After 48 h, the membranes were carefully removed using methanol and annealed in a vacuum oven at 150°C for 1 d. The average thickness for the 40 wt/wt MOP-18 /PIM-1 MMMs and pristine PIM-1 films was 90 μm.

Formation of carbon molecular sieve membranes- The CMSMs were formed by pyrolysis of flat precursor PIM-1 membranes and MMMs. A three-zone tube furnace (MSI-1200X-III) with a quartz tube (National Scientific Company, GE Type 214 Quartz) was fitted with a PID temperature controller (Omega Engineering, Inc., model CN1507TC). Precursor membranes were placed on a graphite plate inside the quartz tube. Pyrolysis was carried out using the temperature protocol displayed below, under a continuous flow of Ultra High Purity Nitrogen (UHP, 200 cm³/min). The CMSMs were removed from the furnace after cooling to room temperature under nitrogen and characterized.

Carbonization Protocol⁸

1. 20 – 250 °C at a ramp rate of 15 °C/min
2. 250 – 535 °C at a ramp rate of 3.85 °C/min
4. 535 – 550 °C at a ramp rate of 0.25 °C/min
5. 120 min soak at 550 °C

2.3.5 Characterization

Polymer: The molecular weight and molecular weight distribution of PIM-1 were characterized by size exclusion chromatography (SEC) using a Viscotek VE 3580 system equipped with a Viscotek column (T6000M) and UV-Vis detector. The SEC solvent/sample module (GPCmax) used HPLC grade THF as the eluent, and calibration was based on polystyrene standards.

Membrane: Cross-sections of polymer membranes were imaged using a Zeiss SUPRA 40 scanning electron microscope (SEM). Polymer membrane cross-sections were prepared by freeze fracturing the samples submerged in liquid nitrogen. Thermal gravimetric analysis (TGA) of the polymer

membranes was completed using a PerkinElmer Pyris 1 TGA thermogravimetric analyzer under a UHP N₂ flow (20 cm³/min) and a ramp rate of 10 °C/min. A Nicolet 360 FTIR instrument equipped with a diamond crystal single bounce ATR attachment was used to acquire attenuated total reflectance-Fourier transform infrared (ATR-FTIR) spectra of the polymer films.

CMSM: Raman analysis of the CMSMs was obtained using a DXR Raman spectrophotometer with a 532 nm laser. X-ray analysis of the CMSMs as well as the MOP-18 was accomplished using a Rigaku Ultima III diffractometer with Cu K α X-ray radiation. X-ray photoelectron spectroscopy of the CMSMs was performed at $\leq 5 \times 10^{-10}$ mbar using a PHI VersaProbe II with Al-K α (1486.7 eV) as the X-ray source. Spectra were acquired using a pass energy of 23.5 eV and a step energy of 0.1 eV and with charge compensation using an electron beam positioned incident to the sample. Spectra were collected before and after sputtering for 2 min using a gas cluster ion beam at 20 kV with a 2x2 sq. mm spot size to ensure oxygen was removed from the surface. All spectra were then analyzed using CasaXPS software.

Cu particles: A JEOL 1400+ transmission electron microscope (TEM) operating at 200 kV was used to image the copper particles present within the CMSM. Samples for TEM were prepared by micronizing the flat carbon membranes using a Resodyn LabRAM Acoustic Mixer at 30 G for 30 min. The powder was then dispersed in methanol. Copper particles were adhered to stainless steel grids (200 mesh, Ted Pella) by immersing the grids in the methanol solution. The sizes of the copper particles in the TEM images were quantified using ImageJ.

2.3.6 Gas permeability testing

The pure gas permeability of each membrane was determined using custom-built permeameters with a LabVIEW 16.0 software interface (National Instruments), previously described by Perez et al.⁴⁹ Flat membranes with known surface areas and thicknesses were mounted into permeation cells and degassed for 12 h before testing at 35°C. A gas leak test was also performed prior to each experiment to ensure accurate permeabilities were obtained. During these experiments, the upstream side of the permeation cell was maintained at 35°C and 2 bar with the respective gas (CO₂ or CH₄ in this study). Pressure transducers were used to monitor the upstream and downstream pressures over time. Equation 1 was used to calculate the permeability of each membrane, utilizing permeability of gas (P_i), flux of gas (n_i), thickness of the membrane (l) and the transmembrane partial pressure difference (Δp_i).⁵⁰ Ideal selectivity was calculated using the permeability ratio of carbon dioxide (P-CO₂) and methane (P-CH₄) for each membrane.

$$P_i = \frac{(n_i)(l)}{\Delta p_i} \quad \text{Equation 1}$$

2.3.7 Aging experiments

The apparatus described above (gas permeability testing) was used for these measurements. Membranes remained in the permeation cell for the entire duration of the experiment. The aging of a membrane was performed by evacuating both the upstream and downstream sides of the membrane for an extended period of time (1 d, 2 d, etc.). Between each run of the same gas, the upstream and downstream sides were degassed for 4 h to remove adsorbed gas molecules. The aging experiments for both the Cu-pillared CMSM and the PIM-1 derived CMSM lasted for a period of 21 d.

Mixed gas experiments- A custom-built permeameter⁵¹ in conjunction with an SRI-3610 gas chromatograph (GC) equipped with a thermal conductivity detector was used for mixed gas (carbon dioxide: methane = 50:50) experiments. Calibration of the GC was carried out by injecting pure CO₂ and CH₄ samples at pressures between 0.01 and 1.0 bar into the sampling loop. The detector signal versus pressure was plotted to obtain the calibration curves. Prior to each experiment, the upstream and downstream sides of the permeation cell were degassed for 12 h. A gas leak test performed prior to each experiment revealed leak rates of less than 0.04 mbar/h. For mixed gas experiments, the cell was maintained at 35 °C with an upstream pressure of 3.0 bar. Pressure transducers were used to monitor the upstream and downstream pressures over time. A stage cut (\emptyset) (Equation 2) of 0.1 was used for this experiment, by determining the retentate purge rate (Q_R). This was calculated by using the mixed gas flow rate across the membrane (Q_P) without a stage cut.⁵¹ The retentate purge rate was controlled by a mass flow controller connected to the feed side.

$$\emptyset = \frac{(Q_P)}{(Q_P + Q_R)} \quad \text{Equation 2}$$

Upon obtaining sufficient pressure in the downstream side, the permeate was then injected into the GC (500 torr). The mixed gas selectivity was acquired by calculating the ratio of the detector signals for each gas, using their calibration curves. The permeabilities for CO₂ and CH₄ were then back calculated from the experimentally determined selectivity.

2.4 Results and discussion

2.4.1 In-situ formation of copper nanoparticles

Thermal analysis of the pristine PIM-1 and the 40 wt/wt MOP-18/PIM-1 MMMs showed a major weight loss of 40% at 500 °C due to the decomposition of PIM-1. The MMM also exhibited a smaller weight loss of 20% at 260 °C due to the decomposition of the coordinating linkers of MOP-18 (Figure 2.2a).²⁹ The weight loss observed at 500 °C for both membranes suggests that the incorporation of MOP-18 into the matrix does not reduce the membranes' thermal stability. Upon the thermal degradation of MOP-18 at 260 °C, copper nanoparticles are formed in-situ. The melting temperature of these nanoparticles was determined using DSC.³⁰ Figure 2.2b shows a melting temperature near 450 °C for the copper particles present within the CMSM, which agrees with theoretical calculations for copper particles less than 20 nm.³¹⁻³³ Particles less than 20 nm are known to show a depressed melting temperature in comparison to the bulk melting temperature of the metal (Cu⁰, 1083 °C), and play a role in the ability of nanoparticles to agglomerate.³¹⁻³³ The instantaneous formation of particles after reaching 260 °C, along with the diffusion controlled growth when in the liquid phase, influences the average size of particles.³⁴ Therefore, parameters such as the pyrolysis temperature, soaking duration, and polymeric precursor (free volume content), allow for control over the size distribution of the copper nanoparticles.

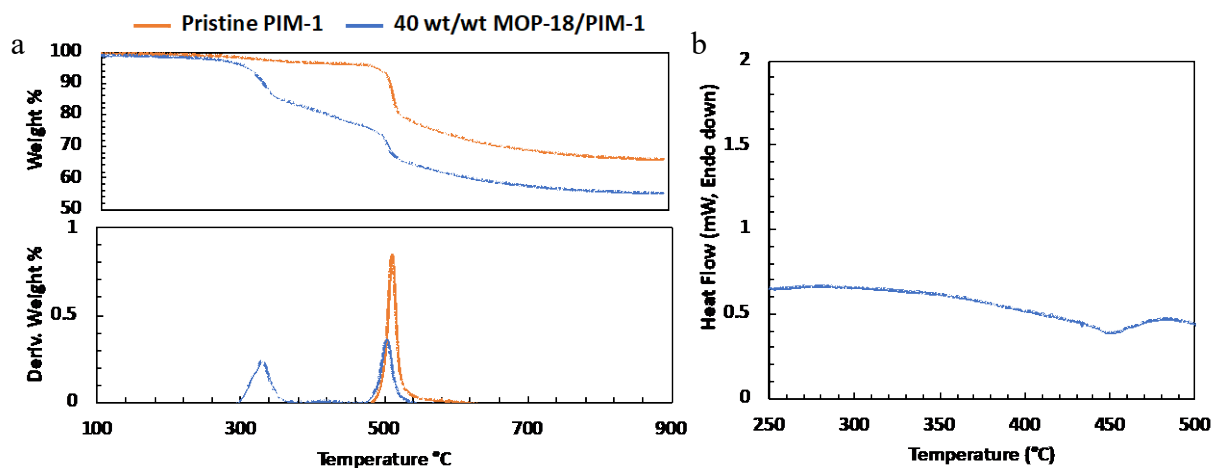


Figure 2.2: (a) TGA and derivative TGA curves of pristine PIM-1 (orange) and 40 wt/wt MOP-18/PIM-1 MMM (blue), and (b) DSC curve of 40 wt/wt MOP-18/PIM-1 MMM.

2.4.2 Tuning copper nanoparticle size distribution

Transmission electron microscopy of the copper nanoparticles show an average particle size between 1 and 20 nm with an aspect ratio of 1 (Figure 2.3a-c). The particle size distribution obtained suggest that agglomeration of the copper particles was impeded after approaching 20nm. This is due to the drastic increase in T_m of the larger particles (>20 nm), minimizing diffusion-controlled growth. Particles >20 nm are a result of Ostwald ripening, which dictates that the larger particles will grow at the expense of the smaller ones.³⁵ Thus, interactions due to the disruptive pyrolysis procedure can bring about a growth in particle size. Minimizing agglomeration is a key factor in obtaining copper nanoparticles with sizes less than 10nm. The size range obtained after pyrolysis at 550°C of the MMM yielded copper nanoparticles which proved to be optimal for this high free volume system. The turbostratic carbon produced as well as its resultant degree of disorder will be discussed further in the following section.

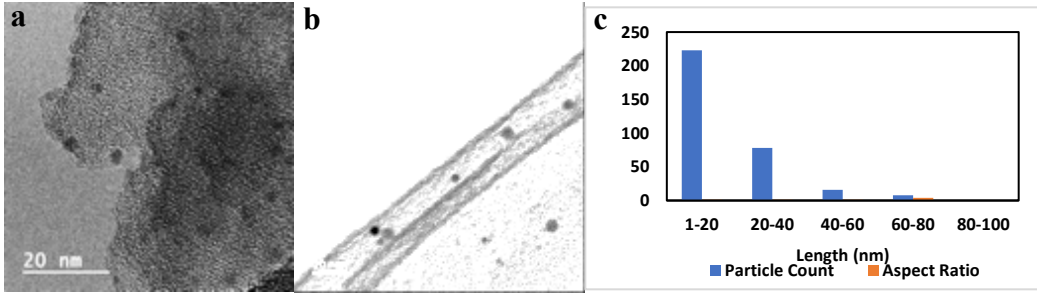


Figure 2.3: (a, b) TEM images of 40 wt/wt MOP-18/PIM-1 CMSM, and (c) its corresponding histogram.

2.4.3 Impact of turbostratic carbon on CMSM stability

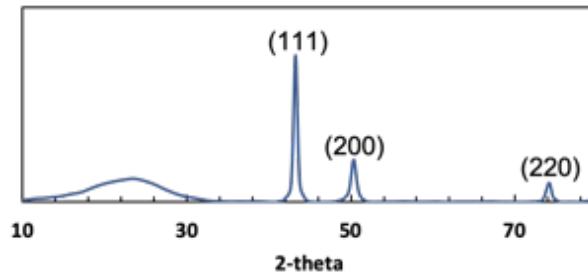


Figure 2.4: X-ray diffraction pattern of a 40 wt/wt MOP-18/PIM-1 derived CMSM.

Figure 2.4 shows an XRD pattern for a 40 wt/wt MOP-18/PIM-1 CMSM with three peaks at 43, 50, and 74 degrees 2-theta corresponding to the 111, 200, and 220 reflections of copper metal. A crystallite size of 14 nm was calculated by applying the Scherrer equation (Equation 3), where D_p is the average crystallite size, λ is the x-ray wavelength (Cu- $K\alpha$), and β is line broadening in radians (peak full width at half maximum, FWHM). The value calculated (14 nm) agrees with the TEM images shown in Figure 2.3.

$$D_p = \frac{(0.94 \times \lambda)}{(\beta \times \cos\theta)} \quad \text{Equation 3}$$

Raman spectroscopy provides a convenient tool to predict the rate of decline in permeability due to physical aging as well as its underlying causes. The Raman spectrum of crystalline graphite is

defined by the presence of two strong peaks labeled disorder (D-band) and graphitic (G-band) at 1350 cm^{-1} and 1580 cm^{-1} , respectively.³⁶ The height ratio of the D-band to G-band provides a measure of disorder within the $\text{sp}^2\text{-sp}^3$ bonded carbons. Based on Equation 4, the I_D/I_G ratio can be used to determine the graphite crystallite size (L_a), where L_a is inversely proportional to the I_D/I_G ratio.³⁷ The G-band position can also be used to monitor changes in disorder associated with graphitic carbon.^{36,38} A blue shift in the G-band corresponds to an increase in sp^3 carbons as well as to a transition from sp^2 carbon rings to sp^2 carbon chains.^{36,38}

$$L_a = 44(I_D/I_G)^{-1} \quad \text{Equation 4}$$

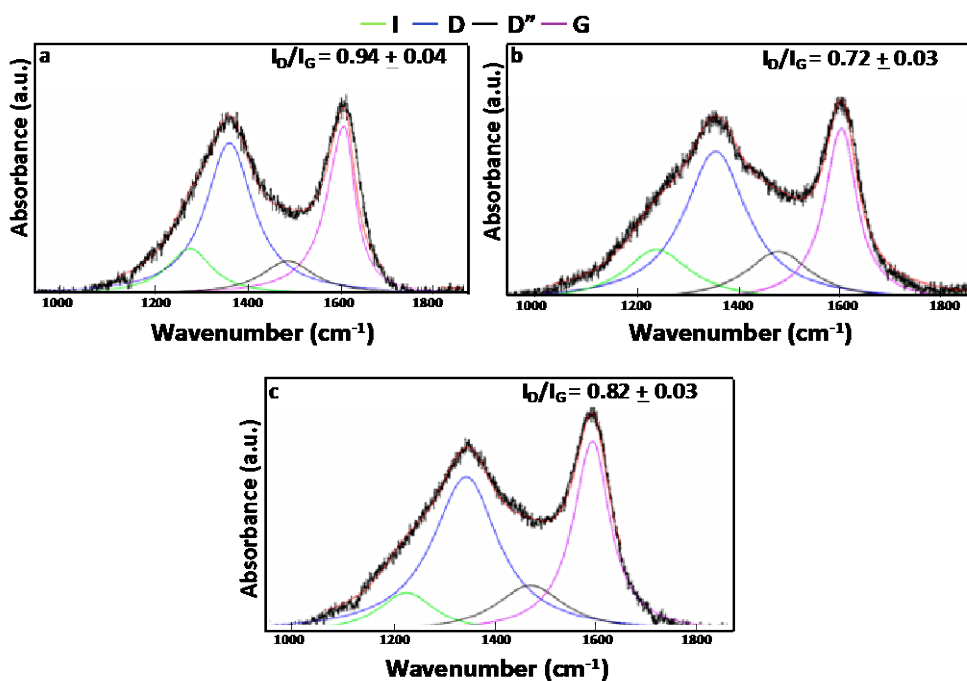


Figure 2.5: Raman spectra of carbon: (a) PIM-1, (b) MOP-18, and (c) 40 wt/wt MOP-18/PIM-1. Raman analysis was used to determine the effect that the 12-C chain of MOP-18 has on the graphitic nature of the CMSM. As shown in Figure 2.5a, the I_D/I_G ratio of pyrolyzed PIM-1 is 0.94. The small unconnected domains are hypothesized to be the reason behind the rapid aging of

PIM-1. However, upon incorporation of MOP-18, a 0.12 decrease in the I_D/I_G ratio is observed (Figure 2.5c). This decrease is most likely due to the carbon associated with MOP-18, as the pyrolysis of MOP-18 itself yields a fairly graphitic material (Figure 2.5b, $I_D/I_G = 0.72$). This secondary source of graphitic carbon in the 40 wt/wt MOP-18/PIM-1 derived CMSM (Figure 2.5c) may be a factor contributing to the stabilization of the carbon membrane. The increase in graphite crystallite size for the pillared CMSM ($L_a = 5.4$ nm), compared to that for the PIM-1 derived CMSM ($L_a = 4.7$ nm), corresponds to a reduction in the number of terminal sp^3 carbon sites,³⁹ which may minimize distortions in the CMSM. When comparing the pristine derived PIM-1 CMSM to the 40 wt/wt MOP-18/ PIM-1 CMSM, a red shift in the G-band position from 1590 cm^{-1} to 1585 cm^{-1} is observed. This suggests that the Cu-pillared CMSM is more stable than PIM-1 due to it having fewer sp^3 carbons (Table 2.1). The data acquired from Raman analysis is summarized in Table 2.1, averages were obtained from three separate CMSMs.

Table 2.1: I_D/I_G height ratios, corresponding L_a values, and G-band positions for PIM-1, MOP-18, and 40 wt/wt MOP-18/PIM-1 pyrolyzed at $550\text{ }^\circ\text{C}$

Carbon	I_D/I_G (Height)	L_a (nm) 550-2	G-Band 550-2
PIM-1	0.94 ± 0.04	4.7	1590
MOP-18	0.72 ± 0.03	6.1	1588
40 wt/wt MOP-18/PIM-1	0.82 ± 0.03	5.4	1585

While stabilizing graphitic sheets by means of increasing the crystallite size, and thus decreasing distortions due to sp^3 terminal carbons is important, it should be stated that this alone is not sufficient to eliminate physical aging. For example, Xu et al. showed a decline in ethylene permeance by 40% over a period of 6 days for a Matrimid[®] 5218 derived CMSM that was pyrolyzed at 550°C .¹² The Matrimid[®] 5218 derived CMSM had an I_D/I_G ratio of 0.6 and a

corresponding crystallite size of 7.3 nm. Therefore, while CMSMs with larger crystallite sizes derived from low free volume polymer precursors may not show declines in permeability >60%¹², as is observed with high fractional free volume polymer precursors, they are still subject to physical aging. Therefore, by increasing the graphite crystallite size along with the incorporation of copper pillars, physical aging within the CMSM can be impeded.

2.4.4 Stability measurements of CMSMs over time

A universally accepted upper bound for CMSM performance has yet to be reported for any gas pair. However, the Robeson upper bound for polymers⁴⁰ allows researchers to compare carbon membrane systems with their polymer precursors. Figure 2.6a shows a plot of CO₂/CH₄ selectivity versus CO₂ permeability for carbon membranes that target CO₂/CH₄ separations. A 40 wt/wt MOP-18/PIM-1 derived CMSM that was aged for 21 d under vacuum (details in methods) not only shows enhanced permselectivity values in comparison to CMSMs reported in literature, but also displays resistance to physical aging.

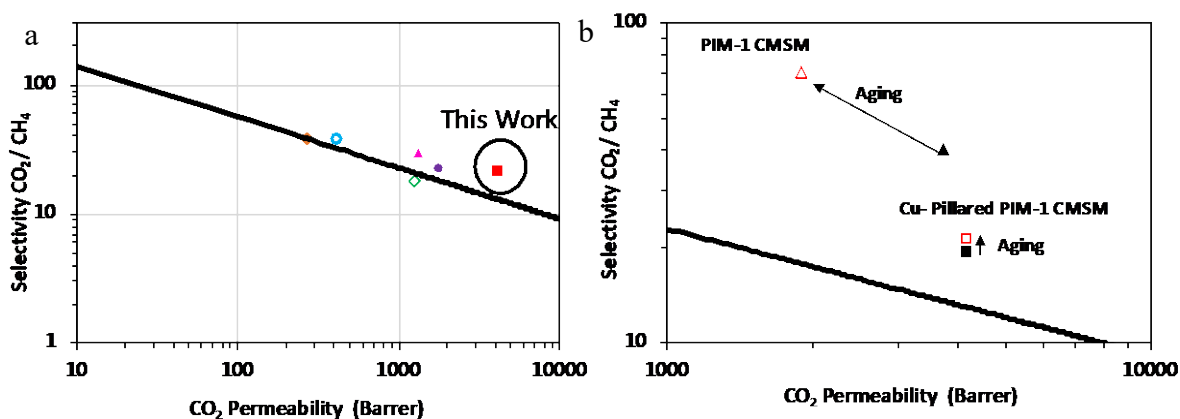


Figure 2.6: (a) Plot of CO₂/CH₄ selectivity versus CO₂ permeability for a 21-day aged 40 wt/wt MOP-18/PIM-1 CMSM, alongside CMSMs reported in literature on Robeson's CO₂/CH₄ upperbound.⁴⁰ PBI/Matrimid (▲),⁴¹ PBI/UIP-S (○),⁴¹ P84 (●),⁴² 6FDA/PMDA-TMMDA (◆),⁴³ PIM-PI (◇).⁴⁴ (b) Plot of CO₂/CH₄ selectivity versus CO₂ permeability for fresh (●, ■) and aged

(b, \square) 40 wt/wt MOP-18/PIM-1 CMSMs alongside fresh (b, \blacktriangle) and aged (b, \blacktriangle) PIM-1 derived CMSMs.

Figure 2.6b shows a plot of CO₂/CH₄ selectivity versus CO₂ permeability for fresh (\blacktriangle) and aged (\blacktriangle) PIM-1 derived CMSMs along with fresh (\blacksquare) and aged (\square) 40 wt/wt MOP-18/PIM-1 derived CMSMs. The Cu-pillared CMSM astonishingly showed minimal change in permselectivity, with a modest 20% decline in methane permeability. This is a drastic improvement over the 70% decline in methane permeability observed for the pristine PIM-1 derived CMSM. The retention in permeability as well as selectivity are in stark contrast to other CMSMs whose permeability declines over time due to physical aging.^{18, 44, 45}

Table 2.2: Pure gas permeabilities (in Barrers) at 35 °C and 2 bar of fresh and aged carbon molecular sieve membranes.

Membrane source	Fresh P-CH ₄ (Barrers)	Fresh P-CO ₂ (Barrers)	Fresh CO ₂ /CH ₄ α	Aged P-CH ₄ (Barrers)	Aged P-CO ₂ (Barrers)	Aged CO ₂ /CH ₄ α
40 wt/wt MOP-18/ PIM-1	252 \pm 4%	4176 \pm 5%	17	200 \pm 2%	4187 \pm 1%	21
PIM-1	93 \pm 6%	3742 \pm 2%	40	27 \pm 0%	1902 \pm 1%	70

Table 2.2 summarizes the pure gas permeabilities of fresh and aged CMSMs (aging protocol in Methods). Average permeabilities and standard deviations were calculated from one piece each of two different membranes. Each membrane surpassed the upper bound, with the Cu-pillared CMSMs showing not only enhanced permeability, but also enhanced resistance to physical aging.

2.4.5 Performance of CMSMs under gas mixture

While pure gas permeability values and ideal selectivities provide research labs with a means to compare membranes based on the Robeson upper bounds,⁴⁰ mixed gas permselectivities reflect results which are obtained under industrially relevant conditions. The 40 wt/wt MOP-18/PIM-1

CMSM under a 50:50 mixture of CO₂ and CH₄ yielded a selectivity of 20, with methane and carbon dioxide permeabilities of 192 and 4,121 Barrers, respectively (Figure 2.7b). There are few articles in the literature that discuss the effects that environmental conditions have on the rate of physical aging (e.g., in air, under vacuum, under pressure gradient, etc.).^{46, 47} Interestingly, the results shown in Figure 2.7a and 2.7b reveal that the pillared CMSM maintains its permselectivity values under both vacuum and a pressure gradient, which is most similar to real world conditions. When comparing pure gas permeabilities to mixed gas permeabilities (Table 2.3), the data acquired for the gas mixture showed no decline in permeability, unlike the 20% decrease observed with pure methane gas. This result is attributed to the time delay in gas chromatograph (GC) injections, where approximately 3 d are needed to acquire ~500 torr within the downstream to inject into the GC (details in Methods). During this time period, the 20% decline in methane permeability which was observed with pure gases, had already occurred. However, the initial decline in permeability over 3 d becomes irrelevant when utilizing CMSMs commercially over a period of months.

Table 2.3: Mixed gas permeabilities (in Barrers) at 35 °C and 2 bar of a 40 wt/wt MOP-18/PIM-1 carbon molecular sieve membrane.

Membrane source	Fresh P-CH ₄ (Barrers)	Fresh P-CO ₂ (Barrers)	Fresh CO ₂ /CH ₄ α	Aged P-CH ₄ (Barrers)	Aged P-CO ₂ (Barrers)	Aged CO ₂ /CH ₄ α
40 wt/wt MOP-18/PIM-1	191	4,121	20	200	4,119	21

2.4.6 Aging resistance of carbon membranes

Physical aging impedes carbon molecular sieve membranes from reaching their full potential.^{4, 12} As shown in Table 2.2 (fresh vs aged), physical aging is characterized by a decline in permeability and increase in selectivity due to the collapse of pore structure.^{9, 48} We have found that pillaring

with copper nanoparticles produces aging resistant carbon membranes. Figure 2.7 shows aging studies of pristine PIM-1 derived and 40 wt/wt MOP-18/PIM-1 MMM derived CMSMs. The pillared CMSM (shown in blue, Figure 2.7a) remains stable over time, whereas the pore structure of the pristine PIM-1 CMSM collapses after 6 days (shown in green, Figure 2.7a), resulting in a loss of permeability. The aging data can be compared to permeability values found in the literature for ultrathin PIM-1 CMSMs (shown in black, Figure 2.7a).⁴⁴ While it is known that thinner (submicron) membranes age the quickest,^{24, 44} the decline in permeability for the bulk PIM-1 CMSM used in this study (90 μm) still showed a decline of greater than 60% in less than 1 week. This decline was not observed for the Cu-pillared CMSM, however, where the resistance to physical aging is attributed to the copper nanoparticles creating a scaffold for the membrane's pore structure. The novel approach described in this study allows for the CMSM to be stabilized against physical aging, without sacrificing permeability.

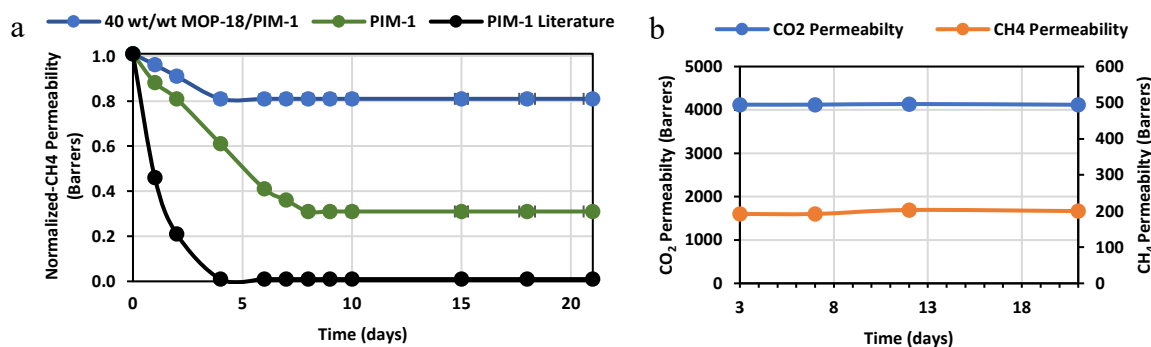


Figure 2.7: (a) Plot of normalized methane permeability versus time acquired under vacuum, and (b) plot of CO₂ and CH₄ permeability versus time acquired under a pressure gradient with a 50:50 CO₂:CH₄ gas mixture. (a) 40 wt/wt MOP-18/PIM-1 (blue), PIM-1 bulk (green), PIM-1 submicron (black, from literature⁴⁴); (b) CO₂ permeability (blue) and CH₄ permeability (red) of 40 wt/wt MOP-18/ PIM-1 CMSM.

2.5 Conclusions

For the first time, copper metal nanoparticles derived from the pyrolytic carbonization of MOP-18 in PIM-1 have been used as pillars to prevent physical aging in CMSMs. The pyrolysis of the precursor MMM yielded copper nanoparticles with sizes between 1 and 20 nm, which served as a scaffold for the highly porous CMSM. DSC confirmed the melting temperature of the copper to be 450°C, which affirms the size distribution measured from TEM images. Single gas permeation data revealed that the copper-pillared CMSM displayed enhanced resistance to physical aging in comparison to pristine PIM-1 derived CMSM. The reduction in permeability of PIM-1-derived CMSMs is hypothesized to be caused by the collapse of unconnected domains. Thus, the copper pillars preserve the micropore structure of the CMSM, resulting in carbon membranes that resist physical aging while maintaining permselective performance. If this promising method is successful for other polymer systems, it could prove to be a powerful approach to mitigate physical aging while maintaining the membranes “fresh” permselectivity.

2.6 Acknowledgments

The technical assistance of Dr. Edson Perez is gratefully acknowledged. Dr. Melissa Wunch is acknowledged for performing XPS analysis.

Financial support from the NSF (CBET-1917747) is gratefully acknowledged.

2.7 Appendix- Supporting information

ATR-FTIR spectroscopy (Figure 2.8) was used to confirm the incorporation of MOP-18 into the polymeric precursor PIM-1. The 40 wt/wt MOP-18/ PIM-1 MMM spectra was normalized to the C-O alkoxy stretch at 1000 cm^{-1} associated with PIM-1. Pristine PIM-1 shows an intense peak at

2240 cm^{-1} corresponding to the -CN functional group present in the backbone, this peak is also observed in the mixed matrix membrane containing 40 wt/wt MOP-18 (Figure 2.8A). The retention of this peak indicates that there is no modification to the polymer precursor in the form of crosslinking due to the incorporation of the additive. The two peaks present at 1580 and 1630 were used to track the C=C stretch associated with the MOP-18 linker (Figure 2.8B). These two peaks as well as the peak present at 730 cm^{-1} which is attributed to the C-O stretch (Figure 2.8C) indicate a successful incorporation of the additive.

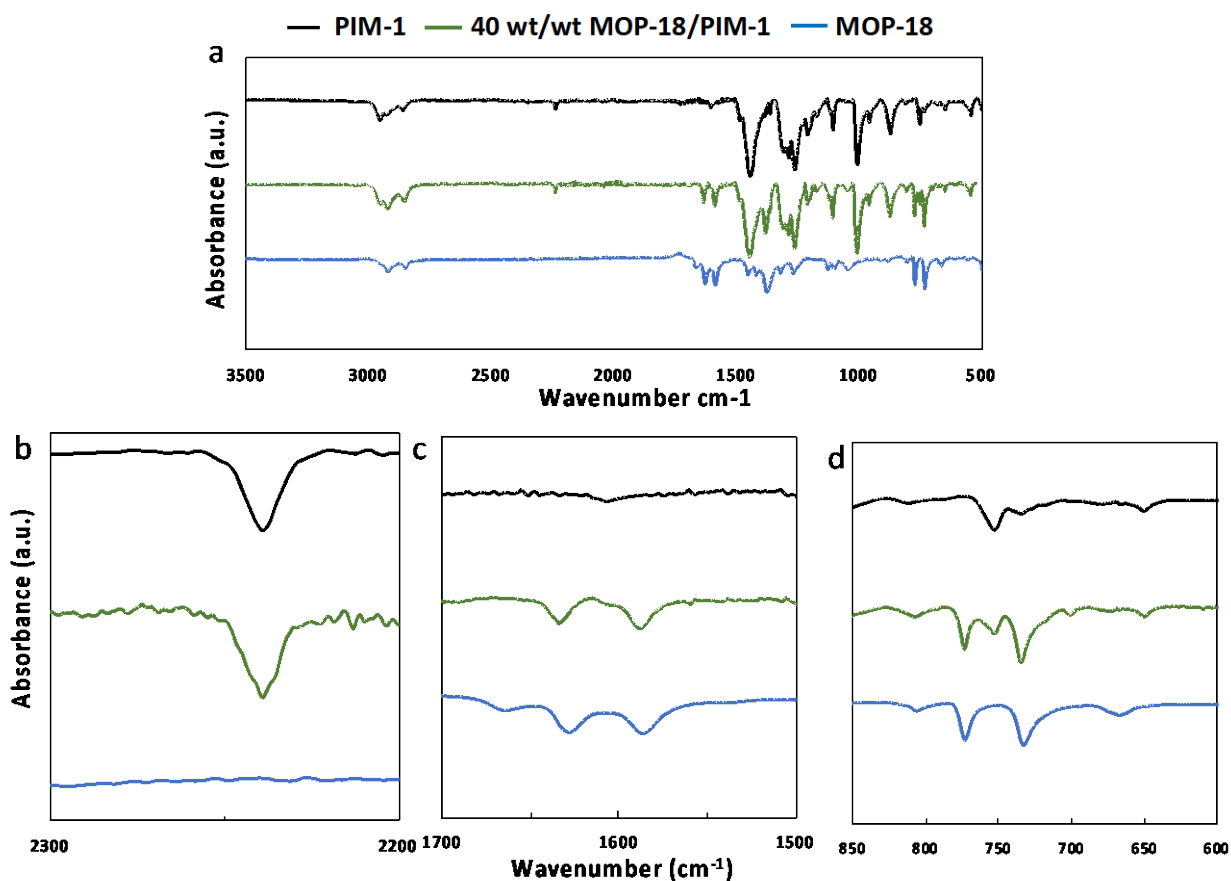


Figure 2.8: ATR-FTIR spectra of membranes: (a) Full spectra of PIM-1 (black), 40 wt/wt MOP-18/PIM-1 MMM (green), and MOP-18 powder (blue) along with Insets. (b) -CN stretch (c) C=C alkene stretch, and (d) C-O stretch

Images obtained of PIM-1 and the 40 wt/wt MOP-18/PIM-1 MMM using SEM are shown in Figure 2.9. The nodular morphology of the pristine PIM-1 polymer cross-section remains intact upon the incorporation of the MOP-18. This is due to the strong interaction between the additive and the polymer, preventing voids which are often observed when inorganic materials are blended with polymers.^{130, 131}

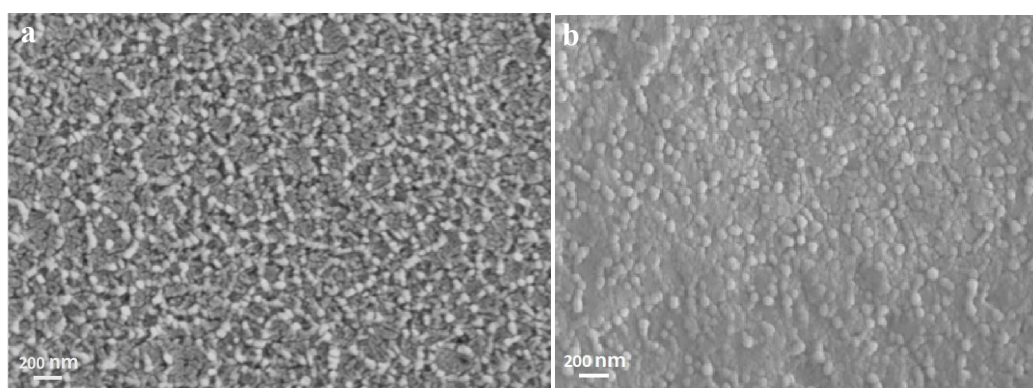


Figure 2.9: SEM images of polymer membrane cross-sections: (a) PIM-1, and (b) 40 wt/wt MOP-18/PIM-1 MMM

X-ray analysis of the CMSMs revealed essentially no change in 2-theta, when PIM-1 was compared to the pillared CMSM a d-spacing of 0.36 was calculated for both membranes (Figure 2.10)

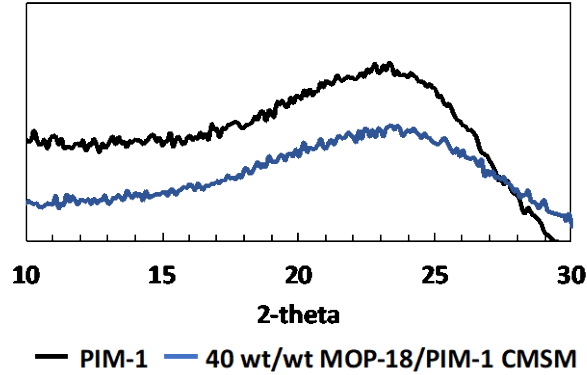


Figure 2.10: X-ray diffractions of PIM-1 (black), and 40 wt/wt MOP-18/ PIM-1 derived (blue) CMSMs

XPS analysis of the 40 wt/wt MOP-18/ PIM-1 CMSM (Figure 2.11) showed two peaks at 932.7 and 952.5 eV, corresponding to copper metal. The lack of the satellite peak in the range of 940-950 eV, commonly associated with CuO, confirms the formation of copper metal and not copper oxide.

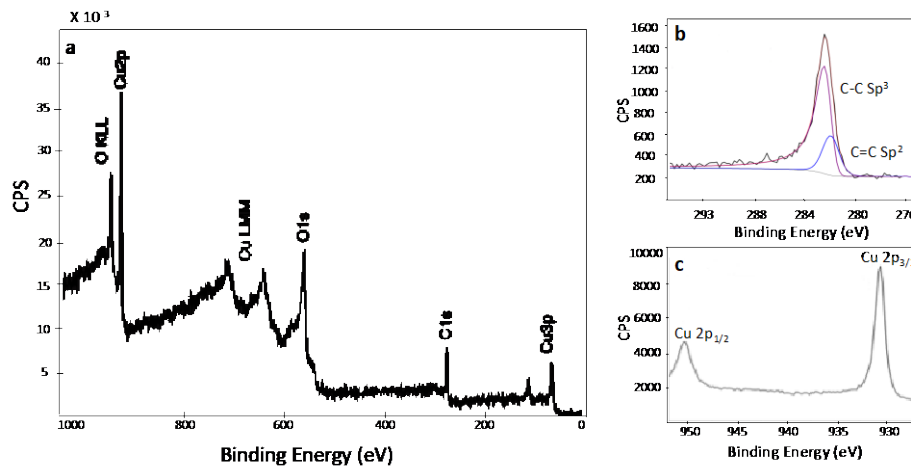


Figure 2.11: XPS spectra of 40 wt/wt MOP-18/PIM-1 CMSM: (a) survey, (b) carbon, and (c) copper

2.8 References

1. Koytsoumpa, E. I.; Bergins, C.; Kakaras, E., The CO₂ economy: Review of CO₂ capture and reuse technologies. *J. Supercrit. Fluids* 2018, **132**, 3-16.

2. Withey, P.; Johnston, C.; Guo, J., Quantifying the global warming potential of carbon dioxide emissions from bioenergy with carbon capture and storage. *Renewable Sustainable Energy Rev.* 2019, **115**, 109408.
3. Jiang, L. Y.; Chung, T.-S.; Rajagopalan, R., Dual-layer hollow carbon fiber membranes for gas separation consisting of carbon and mixed matrix layers. *Carbon* 2007, **45** (1), 166-172.
4. HÄGg, M. B.; Lie, J. A.; LindbrÅThen, A., Carbon Molecular Sieve Membranes. *Ann. N. Y. Acad. Sci* 2003, **984** (1), 329-345.
5. Llosa Tanco, M.; Pacheco Tanaka, David, Recent advances on carbon molecular sieve membranes (CMSMs) and reactors. *Processes* 2016, **4** (29), 2227-9719.
6. Lee, P.-S.; Kim, D.; Nam, S.-E.; Bhave, R. R., Carbon molecular sieve membranes on porous composite tubular supports for high performance gas separations. *Microporous and Mesoporous Mater.* 2016, **224**, 332-338.
7. Sazali, N.; Salleh, W. N. W.; Ismail, A. F.; Ismail, N. H.; Yusof, N.; Aziz, F.; Jaafar, J.; Kadirgama, K., Influence of intermediate layers in tubular carbon membrane for gas separation performance. *Int. J. Hydrog. Energy.* 2019, **44** (37), 20914-20923.
8. Adams, J. S.; Itta, A. K.; Zhang, C.; Wenz, G. B.; Sanyal, O.; Koros, W. J., New insights into structural evolution in carbon molecular sieve membranes during pyrolysis. *Carbon* 2019, **141**, 238-246.
9. Staiger, C. L.; Pas, S. J.; Hill, A. J.; Cornelius, C. J., Gas separation, free volume distribution, and physical aging of a highly microporous spirobisindane polymer. *Chem. Mater.* 2008, **20** (8), 2606-2608.
10. Lagorsse, S.; Magalhães, F. D.; Mendes, A., Aging study of carbon molecular sieve membranes. *J. Membr. Sci.* 2008, **310** (1), 494-502.
11. Menendez, I.; Fuertes, A. B., Aging of carbon membranes under different environments. *Carbon* 2001, **39** (5), 733-740.
12. Xu, L.; Rungta, M.; Hessler, J.; Qiu, W.; Brayden, M.; Martinez, M.; Barbay, G.; Koros, W. J., Physical aging in carbon molecular sieve membranes. *Carbon* 2014, **80**, 155-166.
13. Lagorsse, S.; Campo, M. C.; Magalhães, F. D.; Mendes, A., Water adsorption on carbon molecular sieve membranes: Experimental data and isotherm model. *Carbon* 2005, **43** (13), 2769-2779.

14. Tseng, H.-H.; Zhuang, G.-L.; Lin, M.-D.; Chang, S.-H.; Wey, M.-Y., The influence of matrix structure and thermal annealing-hydrophobic layer on the performance and durability of carbon molecular sieving membrane during physical aging. *J. Membr. Sci.* 2015, **495**, 294-304.
15. Geiszler, V. C.; Koros, W. J., Effects of polyimide pyrolysis conditions on carbon molecular sieve membrane properties. *Ind. Eng. Chem. Res.* 1996, **35** (9), 2999-3003.
16. Centeno, T. A.; Vilas, J. L.; Fuertes, A. B., Effects of phenolic resin pyrolysis conditions on carbon membrane performance for gas separation. *J. Membr. Sci.* 2004, **228** (1), 45-54.
17. Yoshimune, M.; Haraya, K., Flexible carbon hollow fiber membranes derived from sulfonated poly(phenylene oxide). *Sep. Purif. Technol.* 2010, **75** (2), 193-197.
18. Karunaweera, C.; Musselman, I. H.; Balkus, K. J.; Ferraris, J. P., Fabrication and characterization of aging resistant carbon molecular sieve membranes for C3 separation using high molecular weight crosslinkable polyimide, 6FDA-DABA. *J. Membr. Sci.* 2019, **581**, 430-438.
19. Nakagawa, H.; Watanabe, K.; Harada, Y.; Miura, K., Control of micropore formation in the carbonized ion exchange resin by utilizing pillar effect. *Carbon* 1999, **37** (9), 1455-1461.
20. Lu, Z.; Knobler, C. B.; Furukawa, H.; Wang, B.; Liu, G.; Yaghi, O. M., Synthesis and structure of chemically stable Metal–Organic Polyhedra. *J. Am. Chem. Soc.* 2009, **131** (35), 12532-12533.
21. Mason, C. R.; Maynard-Atem, L.; Heard, K. W. J.; Satilmis, B.; Budd, P. M.; Friess, K.; Lanč, M.; Bernardo, P.; Clarizia, G.; Jansen, J. C., Enhancement of CO₂ affinity in a polymer of intrinsic microporosity by amine modification. *Macromolecules* 2014, **47** (3), 1021-1029.
22. Kim, H. J.; Kim, D.-G.; Lee, K.; Baek, Y.; Yoo, Y.; Kim, Y. S.; Kim, B. G.; Lee, J.-C., A carbonaceous membrane based on a polymer of intrinsic microporosity (PIM-1) for water treatment. *Sci. Rep.* 2016, **6**, 36078.
23. Mitra, T.; Bhavsar, R. S.; Adams, D. J.; Budd, P. M.; Cooper, A. I., PIM-1 mixed matrix membranes for gas separations using cost-effective hypercrosslinked nanoparticle fillers. *Chem. Commun. (Cambridge, U. K.)* 2016, **52** (32), 5581-5584.
24. Ogieglo, W.; Furchner, A.; Ma, X.; Hazazi, K.; Alhazmi, A. T.; Pinnau, I., Thin composite carbon molecular sieve membranes from a polymer of intrinsic microporosity precursor. *ACS Appl. Mater. Interfaces* 2019, **11** (20), 18770-18781.
25. Salinas, O.; Ma, X.; Litwiller, E.; Pinnau, I., Ethylene/ethane permeation, diffusion and gas sorption properties of carbon molecular sieve membranes derived from the prototype ladder polymer of intrinsic microporosity (PIM-1). *J. Membr. Sci.* 2016, **504**, 133-140.

26. Song, J.; Du, N.; Dai, Y.; Robertson, G. P.; Guiver, M. D.; Thomas, S.; Pinnau, I., Linear high molecular weight ladder polymers by optimized polycondensation of tetrahydroxytetramethylspirobisindane and 1,4-dicyanotetrafluorobenzene. *Macromolecules* 2008, **41** (20), 7411-7417.
27. Perez, E. V.; Balkus, K. J.; Ferraris, J. P.; Musselman, I. H., Metal-organic polyhedra 18 mixed-matrix membranes for gas separation. *J. Membr. Sci.* 2014, **463**, 82-93.
28. Cheng, Y.; Ying, Y.; Japip, S.; Jiang, S.-D.; Chung, T.-S.; Zhang, S.; Zhao, D., Advanced porous materials in mixed-matrix membranes. *Adv. Mater.* 2018, **30**, 1802401.
29. Furukawa, H.; Kim, J.; Plass, K. E.; Yaghi, O. M., Crystal structure, dissolution, and deposition of a 5 nm functionalized metal-organic great rhombicuboctahedron. *J. Am. Chem. Soc.* 2006, **128** (26), 8398-8399.
30. Gill, P.; Moghadam, T. T.; Ranjbar, B., Differential scanning calorimetry techniques: applications in biology and nanoscience. *J. Bio. Tech.* 2010, **21** (4), 167-193.
31. Ryu, J.; Kim, H.-S.; Hahn, H. T., Reactive sintering of copper nanoparticles using intense pulsed light for printed electronics. *J. Electron. Mater.* 2011, **40** (1), 42-50.
32. Mott, D.; Galkowski, J.; Wang, L.; Luo, J.; Zhong, C.-J., Synthesis of size-controlled and shaped copper nanoparticles. *Langmuir* 2007, **23** (10), 5740-5745.
33. Yeshchenko, O. A.; Dmitruk, I. M.; Alexeenko, A. A.; Dmytruk, A. M., Size-dependent melting of spherical copper nanoparticles embedded in a silica matrix. *Phys. Rev. B* 2007, **75** (8), 085434.
34. Whitehead, C. B.; Özkar, S.; Finke, R. G., LaMer's 1950 model for particle formation of instantaneous nucleation and diffusion-controlled growth: A historical look at the model's origins, assumptions, equations, and underlying sulfur sol formation kinetics data. *Chem. Mater.* 2019, **31** (18), 7116-7132.
35. Ouyang, R.; Liu, J.-X.; Li, W.-X., Atomistic theory of Ostwald ripening and disintegration of supported metal particles under reaction conditions. *J. Am. Chem. Soc.* 2013, **135** (5), 1760-1771.
36. Ferrari, A. C.; Robertson, J., Raman spectroscopy of amorphous, nanostructured, diamond-like carbon, and nanodiamond. *Phys. Eng. Sci.* 2004, **362** (1824), 2477-2512.
37. Knight, D. S.; White, W. B., Characterization of diamond films by Raman spectroscopy. *J. Mater.* 2011, **4** (2), 385-393.

38. Tsaneva, V. N.; Kwapinski, W.; Teng, X.; Glowacki, B. A., Assessment of the structural evolution of carbons from microwave plasma natural gas reforming and biomass pyrolysis using Raman spectroscopy. *Carbon* 2014, **80**, 617-628.
39. Ferrari, A. C.; Robertson, J., Interpretation of Raman spectra of disordered and amorphous carbon. *Phys. Rev. B* 2000, **61** (20), 14095.
40. Robeson, L. M., The upper bound revisited. *J. Membr. Sci.* 2008, **320** (1), 390-400.
41. Behnia, N.; Pirouzfard, V., Effect of operating pressure and pyrolysis conditions on the performance of carbon membranes for CO₂/CH₄ and O₂/N₂ separation derived from polybenzimidazole/Matrimid and UIP-S precursor blends. *Polym. Bull. (Heidelberg, Ger.)* 2018, **75** (10), 4341-4358.
42. Tin, P. S.; Chung, T.-S.; Liu, Y.; Wang, R., Separation of CO₂/CH₄ through carbon molecular sieve membranes derived from P84 polyimide. *Carbon* 2004, **42** (15), 3123-3131.
43. Shao, L.; Chung, T.-S.; Wensley, G.; Goh, S. H.; Pramoda, K. P., Casting solvent effects on morphologies, gas transport properties of a novel 6FDA/PMDA-TMMDA copolyimide membrane and its derived carbon membranes. *J. Membr. Sci.* 2004, **244** (1), 77-87.
44. Ogieglo, W.; Puspasari, T.; Ma, X.; Pinnau, I., Sub-100 nm carbon molecular sieve membranes from a polymer of intrinsic microporosity precursor: Physical aging and near-equilibrium gas separation properties. *J. Membr. Sci.* 2020, **597**, 117752.
45. Hays, S. S.; Sanyal, O.; Leon, N. E.; Arab, P.; Koros, W. J., Envisioned role of slit bypass pores in physical aging of carbon molecular sieve membranes. *Carbon* 2020, **157**, 385-394.
46. Kim, S.-J.; Lee, P. S.; Chang, J.-S.; Nam, S.-E.; Park, Y.-I., Preparation of carbon molecular sieve membranes on low-cost alumina hollow fibers for use in C₃H₆/C₃H₈ separation. *Sep. Purif. Tech.* 2018, **194**, 443-450.
47. Ma, X.; Williams, S.; Wei, X.; Kniep, J.; Lin, Y. S., Propylene/propane mixture separation characteristics and stability of carbon molecular sieve membranes. *Ind. Chem. Res.* 2015, **54** (40), 9824-9831.
48. Wieneke, J. U.; Staudt, C., Thermal stability of 6FDA-(co-)polyimides containing carboxylic acid groups. *Polym. Degrad. Stab.* 2010, **95** (4), 684-693.
49. Reid, B. D.; Ruiz-Treviño, F. A.; Musselman, I. H.; Balkus, K. J.; Ferraris, J. P., Gas permeability properties of polysulfone membranes containing the mesoporous molecular sieve MCM-41. *Chem. Mater.* 2001, **13** (7), 2366-2373.

50. Koros, W. J.; Fleming, G. K., Membrane-based gas separation. *J. Membr. Sci.* 1993, **83** (1), 1-80.

51. Perez, E. V.; Kalaw, G. J. D.; Ferraris, J. P.; Balkus Jr, K. J.; Musselman, I. H., Amine-functionalized (Al) MIL-53/VTEC™ mixed-matrix membranes for H₂/CO₂ mixture separations at high pressure and high temperature. *J. Membr. Sci.* 2017, **530**, 201-212.

CHAPTER 3
TAILORING COPPER PILLARS TO PREVENT PHYSICAL AGING IN CARBON
MOLECULAR SIEVE MEMBRANES

Authors- Whitney K. Cosey, Kenneth J. Balkus, Jr. , John P. Ferraris, Inga H. Musselman*

Department of Chemistry and Biochemistry, BE 26

The University of Texas at Dallas

800 W. Campbell Road

Richardson, TX 75080-3021

² Manuscript title 'Tailoring Copper Pillars to Prevent Physical Aging in Carbon Molecular Sieve Membranes' is in preparation to submit to *Journal of the American Chemical Society*

3.1 Abstract

Carbon molecular sieve membranes (CMSMs) for gas separations provide a means to greatly improve CO₂ separations and subsequent sequestration. CMSMs have a pore size distribution, comprised of micropores (0.7- 2.0 nm) and ultramicropores (<0.7 nm), which provide high flux and high selectivity, respectively. This inherent pore structure has enabled them to outperform polymeric membranes in terms of permselectivity. CMSMs, like polymer membranes, suffer from aging, leading to a decline in membrane performance over time. In the case of CMSMs, physical aging results from the collapse of pores. Improving the longevity of CMSMs by reducing physical aging would transform membrane-based separations, providing a path for their commercialization.

In this work, a method for reducing physical aging through the incorporation of metal nanoparticles that serve as a structural scaffold for membrane pore structure is presented. The pore structure in CMSMs is dependent upon the polymeric precursor, and thus the support system incorporated must be tailored. Copper nanoparticles were formed from soluble, copper-based metal-organic polyhedra 18 (MOP-18) that were dispersed into Matrimid[®] 5218, a low free volume polymer, and polymer of intrinsic microporosity PIM-1, a high free volume polymer. The size (2 to 20 nm) and shape (sphere, rods) of the copper particles that form in-situ are refined by adjusting three experimental parameters: MOP-18 loading, pyrolysis temperature, and soaking time. The ability to tailor the physical properties of copper pillars allows for an approach to maintain free volume in CMSMs derived from various polymer precursors. The Cu-pillared Matrimid[®] 5218 CMSM showed no decline in permeability or selectivity for methane and carbon dioxide. The Cu-pillared PIM-1 CMSM revealed a minimal (20%) decline in methane permeability and no decline in carbon

dioxide permeability. These results suggest that tailored metal pillars can suppress physical aging in CMSMs, thereby enhancing their long-term stability and applicability for gas separations.

3.2 Introduction

The highly developed internal surface area and porosity of carbon molecular sieve membranes (CMSMs) make them excellent candidates to surpass currently used polymeric membranes for gas separations.¹ CMSMs are composed of ultramicropores and micropores, providing the membrane with high selectivity and high permeability, respectively. While carbon membranes are known for enhanced permselectivity compared to their precursors, as well as high chemical and thermal stability, they have two flaws that prevent commercialization, chemical aging and physical aging. Chemical aging, the chemisorption and physisorption of unwanted species, impedes a membrane's permeability. Physical aging, the collapse of a membrane's inherent pore structure, results in the densification of the membrane. Of these two, physical aging is drawing much attention because methods for its reduction, prevention, or regeneration have not been developed. Thus, preparing carbon materials with a strictly controlled and stable pore structure is of great interest to the membrane field.

Physical aging within CMSMs is driven by two factors. The first is noncovalent forces, such as π - π interactions, which are most significant for large graphitic domains. The thermodynamic driving force of graphitic domains to restack leads to pore collapse. The second factor results from the carbonization of high free volume polymer precursors, which yields smaller graphitic domains with a higher density of sp^3 carbons. The open structures of these carbons are not fully connected and collapse with time. Almost all efforts to control micropores in carbon membranes have been

directed toward altering the final pyrolysis temperature.²⁻⁵ Researchers have observed that increasing the final pyrolysis temperature narrows the pore structure, which may play a role in minimizing the effects of physical aging. However, this approach tends to yield membranes that are excessively brittle, impeding their applicability for industrial use. An alternative method is to incorporate an additive into the precursor polymer that will remain upon pyrolysis to support the pore structure, preventing densification of the membrane. Metal nanoparticles can be used to scaffold the microstructure of carbon, and their high thermal stability and tunability make them an ideal material to be used in CMSMs.

Several methods for the synthesis of metal nanoparticles (NPs) have been reported. In addition, protocols have been developed that focus on the fine tuning of NP physical and chemical properties, including producing progressively smaller NP sizes.⁶⁻⁸ Thus, tailoring the size of the metal nanoparticles to preserve a CMSM's free volume is a plausible method that can be used to minimize physical aging. The synthesis of metal pillars with sizes ranging from 2 to 10 nm would be ideal for supporting low free volume polymer precursors such as Matrimid[®] 5218 and polybenzimidazole (PBI). On the other hand, high free volume polymer precursors, such as polymer of intrinsic microporosity 1 (PIM-1) and 6FDA-DAM whose resulting CMSM framework is composed of large unconnected domains, would benefit from larger 10 to 20 nm pillars.

The literature addresses several experimental parameters in the chemical syntheses of metal NPs which alters their shape and size distribution, including temperature, concentration of chemicals, and use of capping agents.⁶ While these experimental parameters can be monitored and controlled, there is still the need to consider two principles. The first is LaMer's model for particle formation,

where metal particles are produced via instantaneous nucleation and their growth is controlled by diffusion.⁹ After the formation of a metal nanoparticle, growth is then influenced by sintering and/or Ostwald ripening. This model predicts that smaller NPs would preferentially adsorb onto larger NPs due to their higher surface energy.¹⁰ With increasing time, the size distribution of particles would increase as the larger particles would grow at the expense of the smaller ones.¹¹ Thus, by minimizing particle–particle encounters, it may be possible to achieve smaller particles as well as a more uniform distribution of particle sizes.

Based on these studies focused on the synthesis of metal NPs, it is clear that metal nanoparticle size and dispersion can be controlled and optimized to accommodate carbon membranes with specific pore size distributions. In this work, the pore structures in CMSMs are pillared with copper nanoparticles derived from soluble, copper-based metal-organic polyhedra 18 (MOP-18). MOP-18 was dispersed into Matrimid[®] 5218 at loadings ranging from 0 to 80 wt/wt, allowing for the in-situ formation of copper nanoparticles during pyrolysis. The size (2 to 20 nm) and shape (sphere, rods) of the copper particles are refined by adjusting three parameters: MOP-18 loading, pyrolysis temperature, and soaking time. An optimal particle size distribution and quantity was achieved with 40 wt/wt loading of MOP-18 (7% Cu) in Matrimid[®] 5218. This loading was therefore used to determine the effect the polymer precursor would have on the metal nanoparticles distribution. PIM-1 was selected as an alternative precursor due to its higher free volume content.

3.3 Experimental

3.3.1 Materials

PIM-1: 5,5',6,6'-tetrahydroxy-3,3,3',3'-tetramethyl-1,1'-spirobisindane (TTSBI) (96%, Sigma Aldrich) was recrystallized using methanol and dichloromethane to purify the material. Tetrafluoroterephthalonitrile (DCTB) (99%, Sigma Aldrich) was purified by vacuum sublimation at 140 °C. DMF (99.8%, Sigma Aldrich) was dried over 4A 4-8 mesh (Sigma-Aldrich) molecular sieves, and anhydrous potassium carbonate (98%, Sigma Aldrich) was dried at 60 °C for 1 d to ensure no water was present. Purification procedures are described in detail elsewhere.¹²

Matrimid[®] 5218: Matrimid[®] 5218 (Ciba Specialty Chemicals) was dried at 120 °C for 1 d in a vacuum oven.

MOP-18: Sodium bicarbonate, 1-iodododecane, 5-hydroxyisophthalic acid, copper acetate monohydrate, ethyl acetate, acetonitrile, potassium hydroxide, methanol, tetrachloroethane, and chloroform, all with purities greater than 97%, were purchased from Sigma Aldrich. Ethyl ether (99.9%) and hydrochloric acid were purchased from J.T. Baker. Concentrated sulfuric acid was purchased from Mallinckrodt. Methanol, acetonitrile, and DMF were dried over 4A molecular sieves prior to use.

3.3.2 Polymer synthesis

PIM-1 was synthesized using reported procedures.¹³ Producing a high molecular weight PIM-1 required a reactant ratio for tetrahydroxytetramethylspirobisindane (TTSBI), 1,4-dicyanotetrafluorobenzene, (DCTB), and anhydrous K₂CO₃ of 1:1:2, respectively. The monomers

were purified prior to synthesis as described above in the materials section. Anhydrous K_2CO_3 (4.2 g, 30 mmol), TTSBI (5.1 g, 15 mmol), and DCTB (3.0 g, 15 mmol) were dissolved in anhydrous DMF (100 mL) and magnetically stirred in a 250 mL flask. The reaction flask was sealed with a septum so that air could be removed by application of vacuum and replaced with N_2 gas; this process was repeated 4x. The reaction flask was then stirred magnetically (810 rpm) at $55^\circ C$ for 23 h. Upon cooling, 150 mL of deionized water was added to the mixture, and the product was collected by filtration. A 75% yield of a neon yellow polymer (PIM-1) was obtained after drying at $90^\circ C$ for 1 d (M_w 60, 000 and PDI of 2 by SEC).

3.3.3 MOP-18 synthesis

The MOP-18 linker, 5-dodecoxyisophthalic acid, was prepared by esterifying 5-hydroxyisophthalic acid with ethanol. Alkylation of the hydroxyl group of the diester, followed by hydrolysis, yielded 5-dodecoxyisophthalic acid. Then, two solutions were prepared. The linker (2.7 g, 7.6 mmol) was dissolved in 100 mL of hot ($80^\circ C$) DMF and stirred until a clear solution was obtained. Copper acetate (1.5 g, 7.6 mmol) was dissolved in 50 mL of DMF and stirred at room temperature until fully dissolved. The two solutions were combined, and 100 mL of methanol was added. The precipitate was allowed to crystallize for 24 h at room temperature, and then was washed 2x with methanol, filtered, and dried in a vacuum oven at $60^\circ C$ for 24 h to yield blue MOP-18 crystals (93% yield). A more detailed synthesis may be found elsewhere.¹⁴

3.3.4 Membrane preparation

MOP-18 was incorporated into two different polymer precursors, Matrimid[®] 5218 and PIM-1, to form mixed-matrix membranes (MMMs). MMM solutions for membrane casting were prepared

by dissolving 0.5 g of the polymeric precursor in 4 g of $C_2H_2Cl_4$, and by dissolving 0.2 g (40 wt/wt) of MOP-18 in 3 g of $C_2H_2Cl_4$. The solutions were stirred for 24 h independently and then combined. The 40 wt/wt MOP-18/polymer clear blue/green solution was stirred for an additional 24h. Pristine Matrimid[®] 5218 and PIM-1 membranes were prepared by dissolving 0.5 g of polymer into 3 g $C_2H_2Cl_4$, the solution was stirred for 24 h at room temperature. After thorough mixing, the pure polymer and MMM solutions were concentrated by evaporating solvent until the polymer concentration reached 12 wt%. A Sheen 1133N automatic applicator with a doctor blade in a laminar flow hood was used to cast the membranes on a glass substrate. After 48 h, the membranes were removed from the substrate, PIM-1 membranes and MOP-18/PIM-1 MMMs required the use of methanol for removal. The membranes were then annealed in a vacuum oven at 150 C for 1 d. The average membrane thickness for MMMs derived from Matrimid[®] 5218 and the pure polymer was 80 μm . The pristine PIM-1, and PIM-1 derived MMMs had an average membrane thickness of 90 μm .

The CMSMs were formed by pyrolyzing flat precursor membranes. A 3-zone tube furnace (MSI-1200X-III) with a quartz tube (National Scientific Company, GE Type 214 Quartz) was fitted with a PID temperature controller (Omega Engineering, Inc., model CN1507TC). Precursor membranes were placed on a graphite plate inside the quartz tube. Pyrolysis was carried out using the two temperature protocols shown below, under a continuous flow of Ultra High Purity Nitrogen (UHP, 200 cm^3/min). The CMSMs were removed from the furnace after cooling to room temperature under nitrogen and characterized.

Protocol 1	Protocol 2
1. 20 – 250 °C at a ramp rate of 15 °C/min	1. 20 – 250 °C at a ramp rate of 15 °C/ min
2. 250 – 535 °C at a ramp rate of 3.85 °C/min	2. 250 – 535 °C at a ramp rate of 3.85 °C/ min
3. 535 – 550 °C at a ramp rate of 0.25 °C/min	3. 535 – 550 °C at a ramp rate of 0.25 °C/ min
4. 0, 2, 4, or 6 h soak at 550 °C	4. 550-875 °C at a ramp rate of 3.85 °C/ min
	5. 875-900 °C at a ramp rate of 0.25 °C/ min
	6. 0, 2, 4, or 6 hr. soak at 900 °C

3.3.5 Characterization

Polymer: The molecular weight and molecular weight distribution of PIM-1 were characterized by size exclusion chromatography (SEC) using a Viscotek VE 3580 system equipped with a Viscotek column (T6000M) and UV-Vis detector. The SEC solvent/sample module (GPCmax) used HPLC grade THF as the eluent, and calibration was based on polystyrene standards.

Membrane: Cross-sections of polymer membranes were imaged using a Zeiss SUPRA 40 scanning electron microscope (SEM). Polymer membrane cross-sections were prepared by freeze fracturing the samples submerged in liquid nitrogen. Thermal gravimetric analysis (TGA) of the polymer membranes was performed using a PerkinElmer Pyris 1 TGA thermogravimetric analyzer under a UHP N₂ flow (20 cm³/min) and a ramp rate of 10 °C/min. A Nicolet 360 FTIR instrument equipped with a diamond crystal single bounce ATR attachment was used to acquire attenuated total reflectance-Fourier transform infrared (ATR-FTIR) spectra of the polymer films.

CMSM: Raman analysis of the CMSMs was obtained using a DXR Raman spectrophotometer with a 532 nm laser. X-ray analysis of the CMSMs as well as the MOP-18 was accomplished using a Rigaku Ultima III diffractometer with Cu K_α X-ray radiation. X-ray photoelectron

spectroscopy of the CMSMs was performed at $\leq 5 \times 10^{-10}$ mbar using a PHI VersaProbe II with Al-K α (1486.7 eV) as the X-ray source. Spectra were acquired using a pass energy of 23.5 eV and a step energy of 0.1 eV and with charge compensation using an electron beam positioned incident to the sample. Spectra were collected before and after sputtering for 2 min using a gas cluster ion beam at 20 kV with a 2x2 sq. mm spot size to ensure oxygen was removed from the surface. All spectra were then analyzed using CasaXPS software. CO₂ and N₂ gas adsorption data was obtained using a micromeritics ASAP 2020 plus version 2.00. The CMSMs pore size distribution were calculated using the 2D-NLDFT method implemented in the SAIEUS software (Micromeritics).

Cu particles: A JEOL 1400+ transmission electron microscope (TEM) operating at 200 kV was used to image the copper particles present within the CMSM. Samples for TEM were prepared by micronizing the flat carbon membranes using a Resodyn LabRAM Acoustic Mixer at 30 G for 30 min. The powder was then dispersed in methanol. Copper particles were adhered to stainless steel grids (200 mesh, Ted Pella) by immersing the grids in the methanol solution. The sizes of the copper particles in the TEM images were quantified using ImageJ.

3.3.6 Pure gas permeation measurements

Pure gas permeability of the membranes was measured using custom-built permeameters with LabVIEW 16.0 software interface (National Instruments), previously described by Perez et al.¹⁵ Flat membranes with known areas and thicknesses were mounted into permeation cells and degassed for 12 h before testing at 35 °C. A gas leak test was also performed prior to each experiment to ensure accurate permeabilities were obtained. During these experiments, the upstream side of the permeation cell was maintained at 35°C and at 2 bar with the respective gas

(CO₂ or CH₄ in this study). Pressure transducers monitored the upstream and downstream pressures as a function of time. Equation 1 was used to calculate the membrane's permeability (P_i), utilizing the flux of the gas (n_i), membrane thickness (l), and the transmembrane pressure difference (Δp).¹⁶ Ideal selectivity was calculated as the ratio of the permeabilities of carbon dioxide (P-CO₂) and methane (P-CH₄).

$$P_i = \frac{(n_i)l}{\Delta p_i} \quad \text{Equation 1}$$

3.3.7 Aging under reduced pressure

The apparatus described in section 3.2.6 was used to measure membrane aging in pristine polymer-derived CMSMs and Cu-pillared CMSMs. The membrane remained in the permeation cell for the entire duration of the 21-day experiment. Aging in the presence of CO₂ and of CH₄ was performed by first evacuating the upstream and downstream sides of the membrane for an extended period of time (e.g., 1 d, 2 d, etc.). Before each run of the same gas, and when switching to a different gas, the upstream and downstream sides were degassed for 4 h to remove adsorbed gas molecules.

Custom built permeameters,¹⁵ in conjunction with an SRI-3610 gas chromatograph (GC) equipped with a thermal conductivity detector, was used for mixed gas (CO₂:CH₄ = 50:50) experiments. Calibration of the GC was carried out by injecting pure CO₂ and CH₄ gas samples, at pressures between 0.01 and 1.0 bar, into the sampling loop. The detector signal was plotted versus pressure to obtain calibration curves. Prior to each experiment, the upstream and downstream sides of the permeation cell were degassed for 12 hrs. A gas leak test was also performed prior to each experiment; the leak rates were less than 0.04 mbar/h. For mixed gas experiments, the cell was maintained at 35°C with an upstream pressure of 3.0 bar. Pressure transducers were used to

monitor the upstream and downstream pressures as a function of time. A stage cut (Θ) of 0.1 was used for this experiment (Equation 2). The retentate purge rate (Q_R) was calculated by using the mixed gas flow rate across the membrane (Q_P) without a stage cut.¹⁷ The retentate purge rate was controlled by a mass flow controller connected to the feed side.

$$\Theta = \frac{(Q_P)}{(Q_P + Q_R)} \quad \text{Equation 2}$$

Upon obtaining sufficient pressure in the downstream side, the permeate was injected into the GC at 500 torr. The mixed gas selectivity was determined by calculating the ratio of the detector signals for each gas, using their calibration curves. The permeabilities for CO₂ and CH₄ were then back calculated from the experimentally determined selectivity.

3.4 Results and discussion

3.4.1 Spectroscopic characterization of mixed matrix membranes

ATR-FTIR spectroscopy was used to confirm the incorporation of MOP-18 into the polymeric precursors Matrimid[®] 5218 (Figure 3.12, supporting information) and PIM-1 (Figure 3.13, supporting information). ATR-FTIR spectra of MMMs prepared from Matrimid[®] 5218 and MOP-18 show peaks at 1580 cm⁻¹ and 1630 cm⁻¹, associated with the C=C alkene stretch of the MOP-18 linker, that increase in intensity with increasing MOP-18 loading. The peak at 730 cm⁻¹, which is attributed to the Cu-O stretch, also indicates successful incorporation of the additive. These three peaks are also observed in the 40 wt/wt MOP-18/PIM-1 MMM (Figure 3.13, Supporting information). Pristine PIM-1 also shows an intense peak at 2240 cm⁻¹ corresponding to the -CN functional group. The retention of this peak in the 40 wt/wt MOP-18/PIM-1 MMM suggests there

is no alteration of the PIM-1 backbone, in the form of crosslinking through this group, due to the incorporation of MOP-18.

3.4.2 Thermal (TGA, DSC) and X-ray analysis of CMSMs derived from MOP-18/Matrimid[®] 5218, and MOP-18/PIM-1 MMMs

Figure 3.1a shows TGA curves of pristine Matrimid[®] 5218, MOP-18, and a 40 wt/wt MOP-18/Matrimid[®] 5218 MMM. The membranes exhibit a major weight loss at 450 °C due to the decomposition of the polymer. The MMM also shows a small weight loss at 300 °C due to the decomposition of MOP-18. Similar trends in weight loss are also observed for the PIM-1 MMM (Figure 3.1b), with MOP-18 decomposing at 300 °C and PIM-1 decomposing at 500 °C.

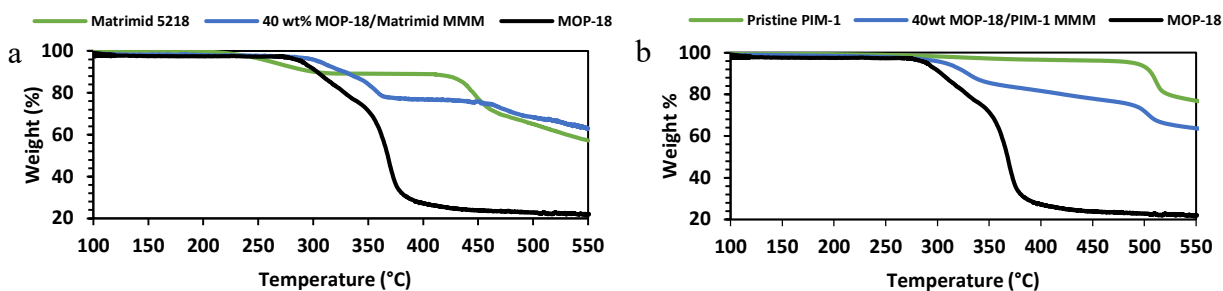


Figure 3.1: TGA of pristine polymers (orange), their corresponding MMMs (Blue), and MOP-18 (Black): (a) PIM-1, and (b) Matrimid[®] 5218

Copper nanoparticles are produced in-situ upon the thermal degradation of MOP-18 at 300 °C. Figure 3.2a shows XRD patterns for the 40 wt/wt MOP-18/Matrimid[®] 5218 and 40 wt/wt MOP-18/PIM-1 derived CMSMs. Three peaks at 43, 50, and 74 degrees 2-theta correspond to the 111, 200, and 220 reflections of copper metal. Figure 3.2b shows a melting temperature of ~450°C for the copper particles present within the CMSMs. A depression in melting temperature (T_m) is a common phenomenon observed for nanoparticles compared to that of the bulk metal.^{6,18,19} This

phenomenon plays a role in the ability of nanoparticles to migrate and agglomerate within the CMSM. It has been theoretically and experimentally determined that particles smaller than 20 nm can exhibit a phase transition from solid to liquid at temperatures less than 550 °C, the pyrolysis temperature of the membrane.^{18,19} The migration of nanoparticles in the liquid state within the membrane is described by LaMer's model,⁹ where the growth of metal particles is driven by diffusion. However, upon approaching the diameter of 20 nm, particles transition back to the solid state and are then influenced by Ostwald ripening.¹⁰ Factors contributing to particle growth will be discussed further in section 3.3.4.

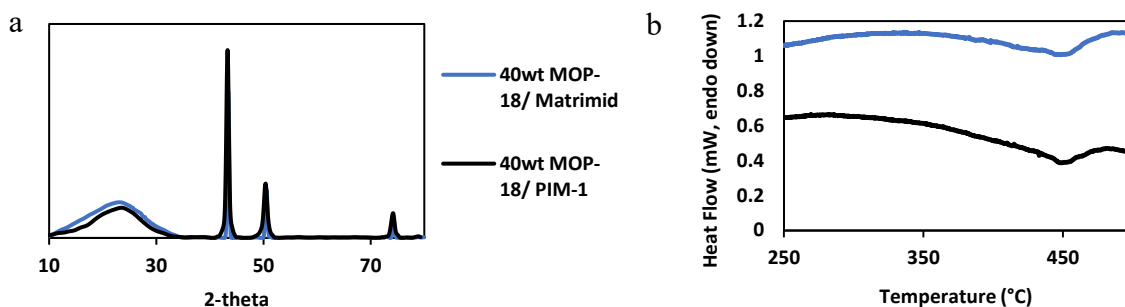


Figure 3.2: (a) XRD pattern and (b) DSC trace of Matrimid[®] 5218 (blue), and PIM-1 (black) derived CMSMs with 40 wt/wt loading of MOP-18.

Based on XRD, a crystallite size of 20 nm and 14 nm was calculated by applying the Scherrer equation (Equation 3) for the 40 wt/wt MOP-18/Matrimid[®] 5218 and 40 wt/wt MOP-18/PIM-1 derived CMSMs, respectively. Here, D_p is the average crystallite size (nm), λ is the X-ray wavelength (Cu-K α , 1.54 Å), and β is line broadening in radians. XPS spectra of the CMSMs (Figure 3.14, supporting information) show two peaks at 932.7 eV (Cu 2p^{3/2}) and 952.5 eV (Cu 2p^{1/2}) corresponding to copper metal. The average particle size calculated from the Scherrer

equation for the two systems shows that the 40 wt/wt MOP-18/PIM-1 membrane, with higher free volume, produces smaller particles. This is hypothesized to be caused by the resulting porous structure of the CMSM, where the disorder of the membrane and its stacking efficiency impacts the migration of Cu particles.

$$D_p = \frac{(0.94 \lambda)}{(\beta \cos \theta)} \quad \text{Equation 3}$$

3.4.3 Raman spectroscopic analysis of CMSMs

Raman spectroscopy was used to analyze the turbostratic carbon and to determine the effect the 12-C chain of MOP-18 has on the graphitic nature of the CMSMs. As shown in Figure 3.3a, the I_D/I_G ratio of pyrolyzed Matrimid[®] 5218 was determined to be 0.82. However, upon incorporation of MOP-18, there is a 0.09 decrease in the I_D/I_G ratio due to the carbon associated with MOP-18. The pyrolysis of MOP-18 alone yields an I_D/I_G ratio of 0.73 (Figure 3.16b, supporting information), which alters the carbon of the MOP-18/Matrimid[®] 5218 derived CMSMs. This shift in Raman to a lower I_D/I_G ratio is a trend that holds for PIM-1 as well. As shown in Table 3.1, a decline in the I_D/I_G ratio by 0.12 is observed for the PIM-1 system. The deconvoluted Raman spectra for the MOP-18/PIM-1 system can be found in the supplemental information (Figure 3.17c).

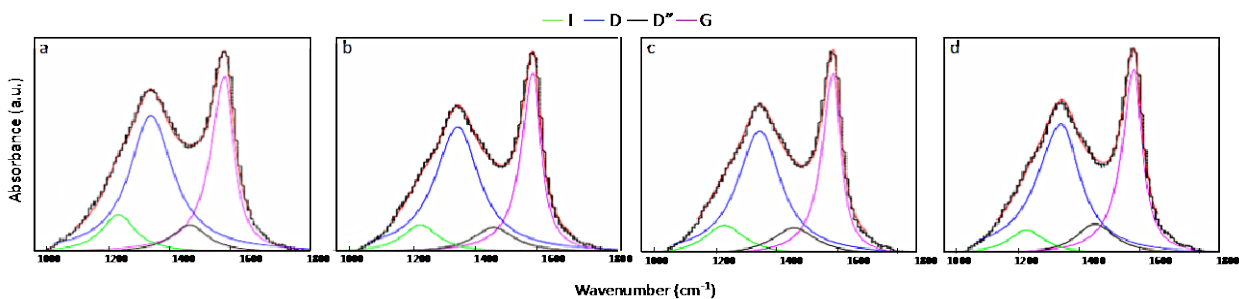


Figure 3.3: Raman spectra of MOP-18/Matrimid[®] 5218 CMSMs pyrolyzed at 550 °C with (a) 0, (b) 20, (c) 40, and (d) 80 wt/wt loadings of MOP-18.

Table 3.1: I_D/I_G height ratios of CMSMs pyrolyzed at 550 °C and 900 °C along with their corresponding L_a (Å) values and G-band (cm^{-1}) positions

CMSM	I_D/I_G	L_a	G-Band	I_D/I_G	L_a	G-Band
	550 °C	550 °C	550 °C	900 °C	900 °C	900 °C
Matrimid [®] 5218	0.82	54	1588	1.03	43	1586
40 wt/wt MOP-18/Matrimid [®] 5218	0.73	62	1590	1.09	40	1589
PIM-1	0.94	47	1590	1.14	39	1590
40 wt/wt MOP-18/PIM-1	0.82	54	1585	1.09	40	1586

The change in the I_D/I_G ratio is of importance because the value can be used to characterize the carbon and to calculate the graphite crystallite size (L_a , Å). The degree of sp^2 clustering is proportional to the crystallite size (L_a), where decreasing L_a increases the D band intensity and shifts the G band to lower wavelengths. Extended conjugation within CMSMs corresponds to a low I_D/I_G ratio and is a signature of having large crystallite sizes.²⁰

$$L_a = 44(I_D/I_G)^{-1} \quad \text{Equation 4}$$

Based on the data in Table 3.1, it can be extrapolated that the incorporation of MOP-18 increases the average crystallite size, and may thus be a factor in its ability to minimize physical

aging. The increase in the pyrolysis temperature from 550 °C to 900 °C for both the Matrimid® 5218 and PIM-1 systems produces CMSMs exhibiting higher I_D/I_G ratios and thus smaller crystallite sizes. This decrease in crystallite size to ~4 nm occurs with both systems due to a breakdown of the graphitic sheets. The crystallite size also impacts the distribution and size of the Cu particles. Smaller and more disordered graphitic sheets, subject to stacking imperfections, provide additional pathways for agglomeration to occur on a faster time scale. This could yield a more uniform distribution of particles due to fewer particles existing in the liquid phase after reaching 20 nm.

3.4.4 Transmission electron microscope

Transmission electron microscopy was used to image the copper nanoparticles present within the CMSMs. The particles size and distribution were drastically influenced by key factors such as MOP-18 loading, the final pyrolysis temperature, as well as the soaking duration. The final pyrolysis temperature and soak time are denoted as temperature (°C) - soak time (in hours). For example, a membrane pyrolyzed at 550 °C and soaked for 2 h is written as 550-2. The loading of MOP-18 proved to be key in obtaining copper particles smaller than 20 nm. As shown in Figure 3.4, membranes pyrolyzed at 550-2 exhibited an increase in the overall size of copper particles with an increase in MOP-18 loading. Decreasing the soaking duration from 2 to 0 h allowed for control over the average particle size, by decreasing the time frame in which particle-particle interactions may occur. Membranes pyrolyzed at 550-0 showed a significantly higher number of particles with sizes ranging from 1 to 20 nm (Figure 3.5a), compared to those pyrolyzed at the same temperature and soaked for 2 h (Figure 3.5b). The 20 wt/wt loading revealed the highest percentage (87%) of particles with sizes less than 10 nm (shown in Figure 3.4c), in comparison

to the 40 wt/wt (80%). When increasing the loading from 20 to 40 wt/wt, the average particles size shifts closer to 15 nm, as shown in Figure 3.4B. The 80 wt/wt CMSM produced agglomerates that were much too great in size to achieve an even distribution (Figure 3.4 C). This non-uniformity in the 80 wt/wt affects the membranes reproducibility, making them impractical for gas separations.

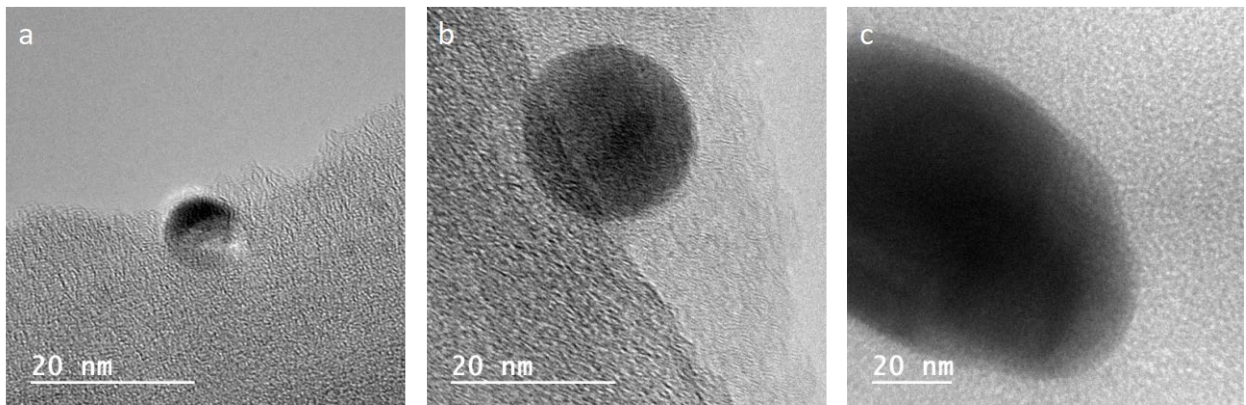


Figure 3.4: Transmission electron microscopy of MOP-18/ Matrimid[®] 5218 derived CMSMs pyrolyzed at 550 °C, 2 h: (a) 20 wt/wt , (b) 40 wt/wt, (c) 80 wt/wt

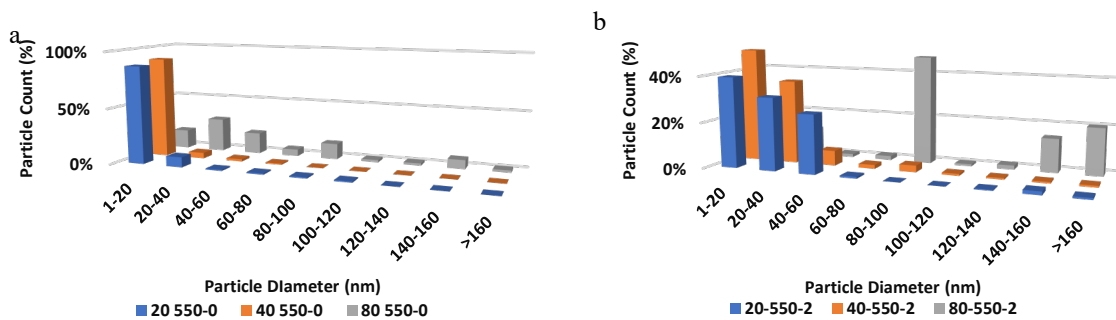


Figure 3.5: Copper particle size distribution within MOP-18/Matrimid[®] 5218 derived CMSMs at pyrolysis conditions (a) 550 °C, 0 h and (b) 550 °C, 2 h as a function of MOP-18 loading: 20 wt/wt (blue), 40 wt/wt (orange), and 80 wt/wt (gray).

When comparing Figure 3.5a to 3.5b, it can be concluded that increasing the soaking time shifts the average particle size to larger values due to an increase in the number of agglomerates. This

trend is illustrated in Figure 3.6, where a 40 wt/wt MOP-18/Matrimid[®] 5218 CMSM is soaked at 550 °C from 0 to 6 hrs. With an increase in soaking time, more particle-particle interactions occur resulting in particles with sizes approaching 60 nm as shown in the histograms in Figure 3.7. The tapering off of particles after 20 nm is due to the inability of the larger particles to move throughout the membrane. The depressed melting temperature, shown in Figure 3.2, results in the particles' ability to diffuse and agglomerate within the CMSM. The decline in the number of particles existing in the liquid phase impedes growth after 20 nm, as shown in the histograms. The particles greater than 20 nm in size are the result of Ostwald ripening. Based on Ostwald's theory, the larger particles grow at the expense of the smaller particles in order to reduce the overall energy of the system.¹⁹

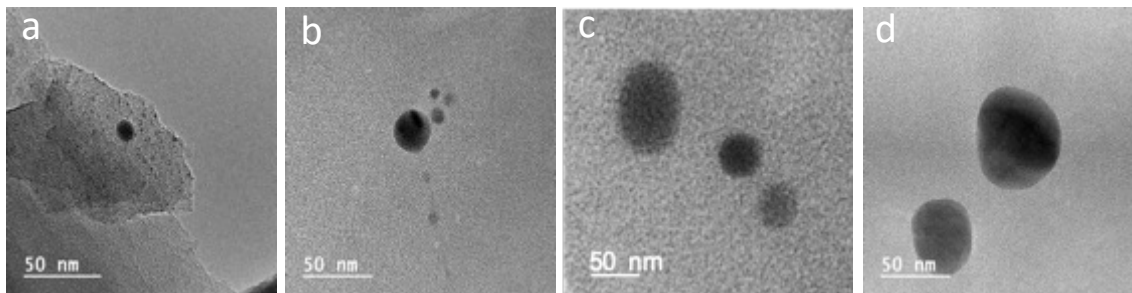


Figure 3.6: Transmission electron microscopy images of 40 wt/wt MOP-18/Matrimid[®] 5218 CMSMs pyrolyzed at (a) 550 °C, 0 h, (b) 550 °C, 2 h, (c) 550 °C, 4 h, (d) and 550 °C, 6 h.

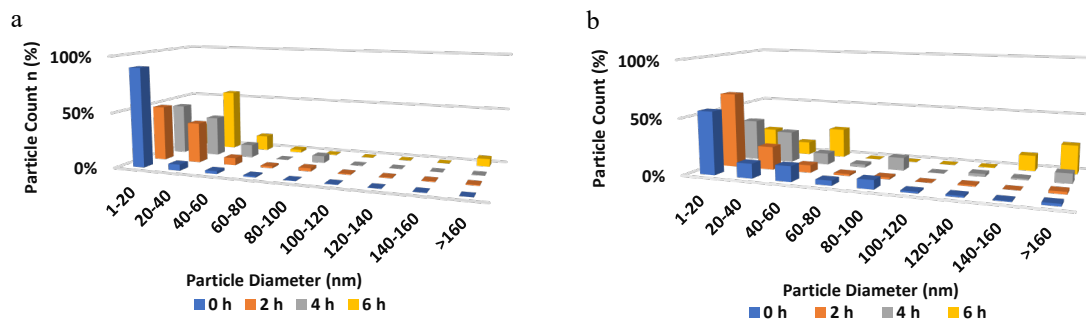


Figure 3.7: Copper particle size distribution within a 40 wt/wt MOP-18/Matrimid[®] 5218 derived CMSM at 550 °C (a) and 900 °C (b) as a function of soaking duration for 0, 2, 4, and 6 h

Particle size as a function of carbonization temperature was also investigated. When comparing the histograms presented in Figure 3.8, for each weight loading, the particle size distribution increases slightly when comparing the 550-2 (shown in orange) protocol to the 900-2 protocol (Shown in blue). Although, increasing the pyrolysis temperature did yield a narrower distribution of copper particles. This is due to the membrane becoming denser at elevated temperatures, which restricts the particles movement within the CMSM. Pyrolysis at elevated temperatures, as show in Raman, yields highly disordered carbon. The degree of disorder, as well as the extension in time to complete pyrolysis for the 900 °C protocol (2.5 h difference), leads to poor carbon (highly brittle), and larger particles.

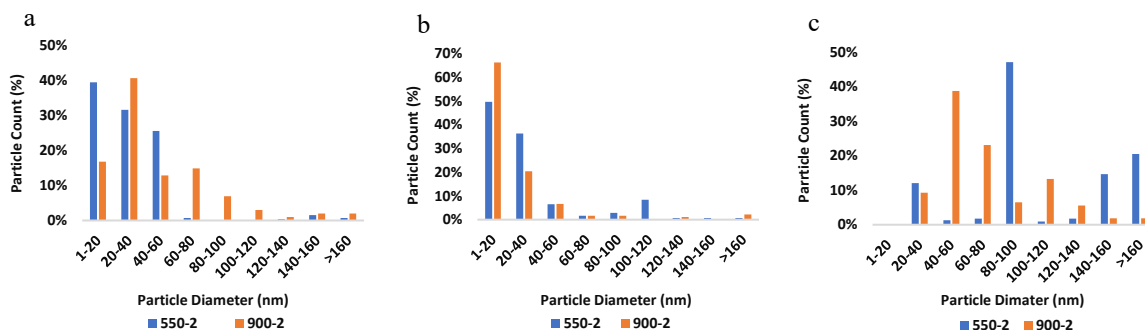


Figure 3.8: Copper particle size distribution within MOP-18/Matrimid[®] 5218 derived CMSMs as a function of carbonization temperature, 550 °C (blue) versus 900 °C (orange) for: (a) 20 wt/wt, (b) 40 wt/wt, and (c) 80 wt/wt MOP-18 loadings.

Based on the data collected the optimal pyrolysis temperature to achieve small (<20 nm) uniform particles is 550 °C. This pyrolysis temperature minimizes the distortions within the resultant graphitic membrane (fewer sp³ terminal carbons), while also minimizing the time allowed for agglomeration to occur. To maximize the effect pillaring would have on the CMSM, copper particles capable of fitting into the pore structure would be most advantageous, in order to support the membrane rather than introduce voids. Based on the data presented in Figure 3.4a and 3.6a, the 550-0 carbonization procedure yields the smallest particles with a uniform size distribution. This optimal distribution for Matrimid[®] 5218 derived CMSMs is investigated by gas permeation over time to determine its effectiveness in reducing physical aging, and is discussed in the following section.

The final parameter investigated was the effect the free volume of the precursor would have on the particle size. With the diffusion of particles being a primary factor involved in their agglomeration, the free volume of the precursor may influence the distribution. PIM-1 was used as a polymer precursor to compare to the data collected for the 40 wt/wt MOP-18/ Matrimid[®] 5218 CMSM 550

°C, 2 h. A 40 wt/wt MOP-18/PIM-1 CMSM was prepared by pyrolyzing the MMM at 550 °C, 2 h. The 550 °C, 2 h carbonization protocol was selected because it is one of the most common protocols used within the literature.

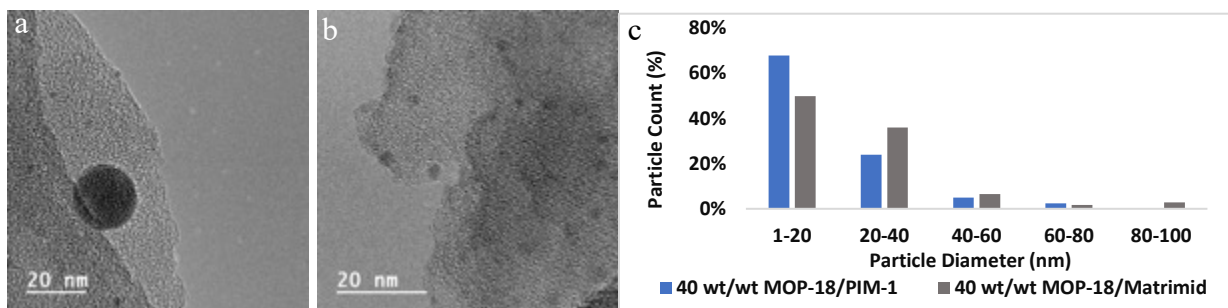


Figure 3.9: TEM images of (a) 40 wt/wt MOP-18/Matrimid[®] 5218 CMSM and (b) 40 wt/wt MOP-18/PIM-1 CMSM, and (c) their corresponding histograms.

The particle size distribution of both the 40 wt/wt MOP-18/Matrimid[®] 5218 and 40 wt/wt MOP-18/PIM-1 CMSMs are shown in Figure 3.9. The size distribution obtained suggest that the higher the free volume, the smaller the particles are. This data supports the values calculated by applying the Scheerer equation, and is due to the rate at which particles agglomerate. High free volume polymer precursors produce small graphitic sheets upon pyrolysis (L_a , Table 1), these small sheets produce both distortions (in the form of sp^3 terminal sites), and additional pathways (in the form of mesopores). These pathways facilitate particle-particle interaction, and thus occurs more frequently in high free volume systems in comparison to low free volume systems. These interactions lead to particles reaching maximum size (>20 nm) in a smaller time frame, which prevents the solid to liquid phase transition of the metal. This transition back to solid minimizes the formation of large agglomerates. Due to the disordered graphitic sheets in the PIM-1 system, reducing the loading of MOP-18 in the high free volume PIM-1 precursor to 20 wt/wt, yielded

similar results. As shown in Figure 3.16 (Appendix), a 20 wt/wt MOP-18/PIM-1 CMSM pyrolyzed at 550-2 showed a particle size distribution almost identical to the 40 wt/wt loading.

3.4.5 Pore size distribution

The collapse of a membranes pore structure, due to physical aging, is a thermodynamically-driven process which leads to a dense membrane. The mechanisms by which physical aging occurs can be probed by Raman analysis. CMSMs with low I_D/I_G ratios yield large graphitic crystallite sizes with extended conjugation. It is hypothesized that π - π interactions lead to restacking of these graphene-like domains causing pore collapse. On the other hand, CMSMs with high I_D/I_G ratios have small unconnected domains, which lead to a rearrangement of the CMSM with time. Measuring the pore size distribution of CMSMs before and after aging can illustrate the changes that occur due to physical aging. The incorporations of Cu pillars, which aim to prevent the collapse of the membranes micropore structure, may also be investigated by measuring the pore size of a Cu-pillared CMSM before and after aging. Isotherms are presented in Figure 3.10 for fresh and 21 d aged CMSMs, along with their corresponding pore size distributions. It is observed that the 21 d aged PIM-1 CMSM increases in CO_2 adsorption, whereas the aged Cu-pillared CMSM remains constant. The increase in CO_2 adsorption corresponds to an increase in the CMSMs ultramicropores. The increase is due to the collapse of the CMSMs micropores, which generates ultramicropores. The results demonstrate that the Cu-pillared PIM-1 CMSM retained its “fresh” pore size distribution due to the incorporation of pillars. The pore size distribution obtained also highlights that Cu pillars less than 5 nm are most likely serving as the support for the membranes micropores.

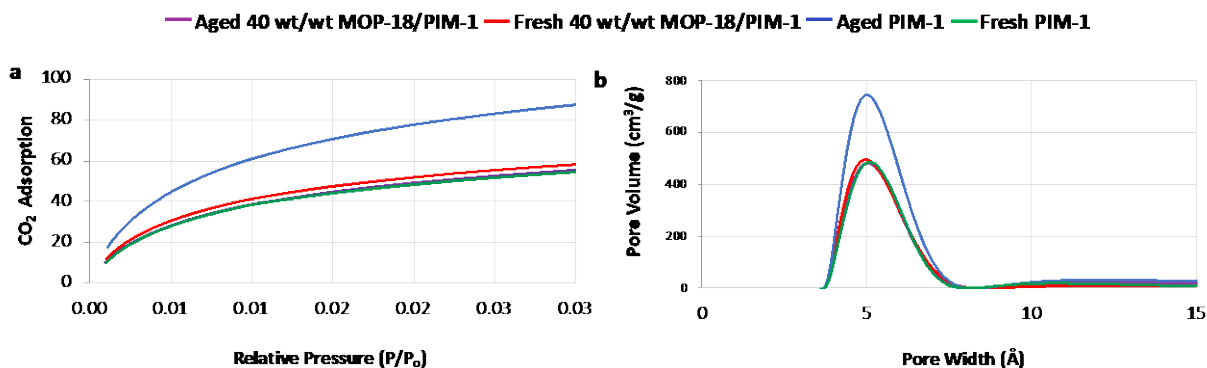


Figure 3.10: (a) Plot of CO₂ adsorption at 0 °C versus relative pressure for PIM-1-derived CMSMs, and (b) their corresponding pore size distribution calculated from the 2D-NLDFT.

The pore size distribution for Matrimid[®] 5218-derived CMSMs, before and after aging, was also investigated. Figure 3.11 shows the Matrimid[®] 5218-derived CMSMs CO₂ isotherms', along with their corresponding pore size distributions. A decline in CO₂ adsorption is observed for the pristine Matrimid[®] 5218- derived CMSM, and in the membranes ultramicropores, as the membrane ages. These data suggest that the rather large graphitic crystallites present in Matrimid[®] 5218, in comparison to PIM-1, are shifting with time. This shift in the graphitic domains, due to π - π interactions, is driving the collapse of the membranes ultramicropores. The ultramicropores are a result of defects between the graphitic sheets, thus as the CMSM transitions to a more thermodynamically stable structure, the membranes ultramicropores are negatively impacted. The Cu-pillared Matrimid[®] 5218 CMSM on the other hand, revealed a slight increase in the membranes CO₂ adsorption and ultramicropores. These results highlight that the Cu-pillared Matrimid[®] 5218 membranes pore structure is remaining intact, and that the incorporation of pillars prevented a shift in the CMSMs graphitic sheets. The increase in CO₂ adsorption and in the membranes ultramicropores, its hypothesized to occur due to the Cu-pillars creating/directing micropores

within the CMSM during its pyrolysis. A small percentage of these micropores are collapsing with time, generating ultramicropores.

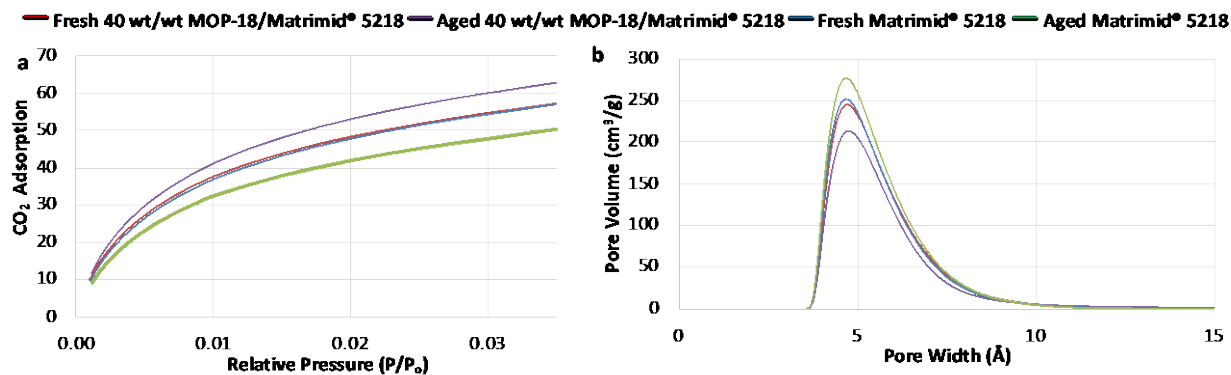


Figure 3.11: (a) Plot of CO₂ adsorption at 0 °C versus relative pressure for Matrimid® 5218-derived CMSMs, and (b) their corresponding pore size distribution calculated from the 2D-NLDFT

3.4.6 Gas permselectivities

Physical aging continues to impede the carbon molecular sieve membranes.^{21,22} Physical aging is characterized by a decline in permeability and increase in selectivity due to the collapse of pore structure.²³⁻²⁶ Table 3.2 shows the pure gas permeabilities and selectivities of fresh and 21-d aged carbon membranes (Aging exp. described in section 3.2.7). Average permeability and standard deviations were determined with the permeabilities obtained using two separate membranes for each case. The aged permeabilities shown illustrates the impact that the loading of MOP-18 and soaking duration have on the membranes effectiveness at reducing physical aging. The gas permeability data plotted in Figure 3.10 shows that the 40 wt/wt loading of MOP-18 (7% Cu), has a greater impact on physical aging in comparison to the 20 wt/wt (4% Cu). This is due to relative amount of copper present within the CMSM rather than the shape or distribution of the particles. The variation in copper size distribution obtained with the 40 wt/wt MOP-18/Matrimid® 5218

CMSM pyrolyzed at 550 °C, 2 h impacted the reproducibility of the membrane as shown in the percent standard deviations (Table 3.2).

Table 3.2: Pure gas permeabilities (in Barrer) of MOP-18 Matrimid[®] 5218 membranes at 35 °C and 2 bar.

CMSM	Fresh P-CH ₄	Fresh P-CO ₂	Aged P-CH ₄	Aged P-CO ₂	% decline (CH ₄)	% decline (CO ₂)
Matrimid [®] 5218 (550 °C, 2 h)	111 ± 9%	1179 ± 4%	71 ± 1%	912 ± 1%	36	23
20 wt/wt MOP-18/Matrimid [®] 5218 (550 °C, 2 h)	95 ± 14%	1082 ± 4%	70	900	26	17
40 wt/wt MOP-18/Matrimid [®] 5218 (550 °C, 2 h)	88 ± 15%	1654 ± 15%	73 ± 2%	1389 ± 2%	17	16
40 wt/wt MOP-18/Matrimid [®] 5218 (550 °C, 2 h)	107 ± 5%	1785 ± 3%	101 ± 1%	1765 ± 1%	0.05	0.01

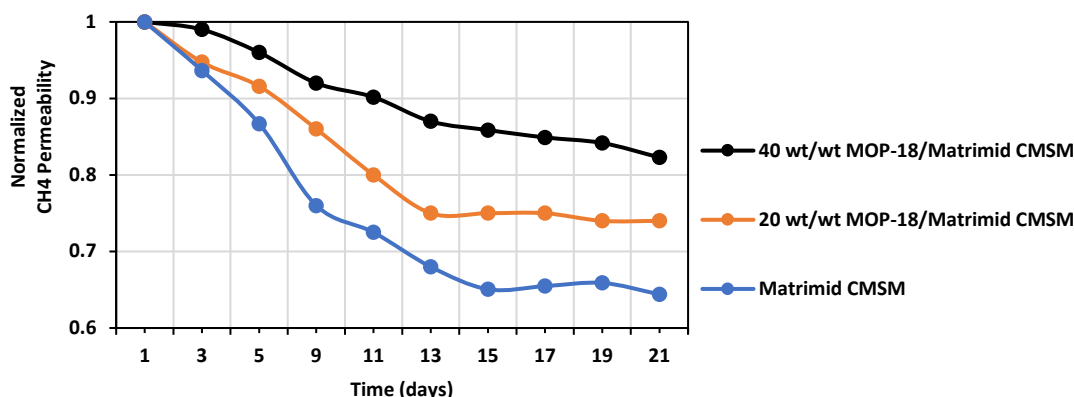


Figure 3.12: Change in CH₄ permeability upon aging for 0 wt/wt (blue), 20 wt/wt (orange), and 40 wt/wt (black) MOP-18/Matrimid[®] 5218 derived CMSMs at 550-2.

By controlling the particle shape and distribution through the carbonization protocol, the membranes ability to resist physical aging as well as the membranes reproducibility was significantly improved. Figure 3.11 shows pure gas permeabilities for a 40 wt/wt MOP-18/Matrimid[®] 5218 CMSM pyrolyzed at 550-0. Through shortening the duration at which particles are allowed to interact from 2 to 0 hours, a ~100% retention in membrane permeability was

achieved. The CMSMs resistance to physical aging was also investigated under a pressure gradient ($\Delta P = 2$), both methane and carbon dioxide retained their “fresh” permeability values of 101 and 1,756 Barrers, respectively over a period of 21 days.

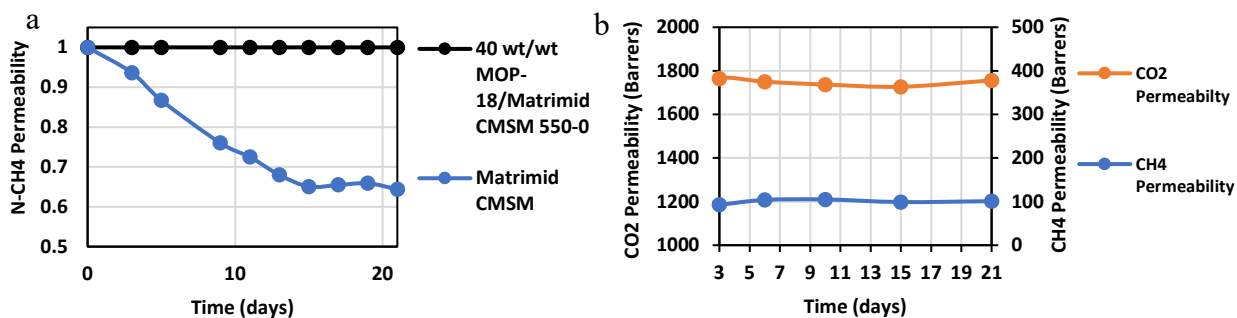


Figure 3.13: (a) Plot of normalized CH₄ permeability versus time for Matrimid[®] 5218 derived CMSMs under reduced pressure, and (b) plot CH₄ and CO₂ permeability versus time for a 40 wt/wt MOP-18/Matrimid[®] 5218 CMSM pyrolyzed at 550 °C under a pressure gradient

The incorporation of pillars to reduce physical aging has proven to be applicable in multiple systems. As shown in Chapter 2, the incorporation of copper pillars into the PIM-1 system allowed for a complete retention in carbon dioxide permeability (4187 Barrers), with only a 20% decrease in methane permeability (252 to 200 Barrers). Which is an improved resistance to aging in comparison to the pristine PIM-1 derived CMSM, whose methane permeability declined by 70% (93 to 27 Barrers). The stability of the Cu-Pillared PIM-1 CMSM was also investigated under pressure gradient. The GC data acquired with a 50:50 blend of methane and carbon dioxide showed consistent permselectivity values over a period of 21 days, with a methane permeability of 192 Barrers and a carbon dioxide permeability of 4121 Barrers. The results are summarized in Chapter 2 Table 2.2. The gas permeation data acquired for the Matrimid[®] 5218, low free volume

system, and PIM-1, high free volume system, indicate the incorporation of Cu-pillars impeded physical aging.

3.5 Conclusions

The pyrolysis of the MMMs derived from MOP-18 yielded copper nanoparticles in-situ, their size and distribution were tailored by varying the loading of MOP-18, the carbonization temperature, as well as the soaking duration. DSC confirmed the melting temperature of the copper nanoparticles to be 450 °C. The depression in melting temperature in comparison to the bulk melting temperature for copper metal (1083 °C), allowed for the agglomeration of metal particles. To minimize particle size, and tighten the size distribution, it was determined that for low free volume polymer precursors such as Matrimid[®] 5218, the 550 °C, 0 h protocol is more optimal. Gas permeation data proved that the use of copper pillars to scaffold CMSMs inherent pore structure can be utilized in various systems. The ability to impede physical aging, as observed with the copper pillared CMSMs, is not controlled by the functionality of precursor. Making this technique a more general approach. Through the use of copper pillars, the micropores of the resultant Cu-pillared CMSMs were preserved, minimizing the effects of physical aging.

3.6 Acknowledgments

The technical assistance of Dr. Edson Perez is gratefully acknowledged.

Financial support from the NSF (CBET-1917747) is gratefully acknowledged.

3.7 Appendix- Supporting information

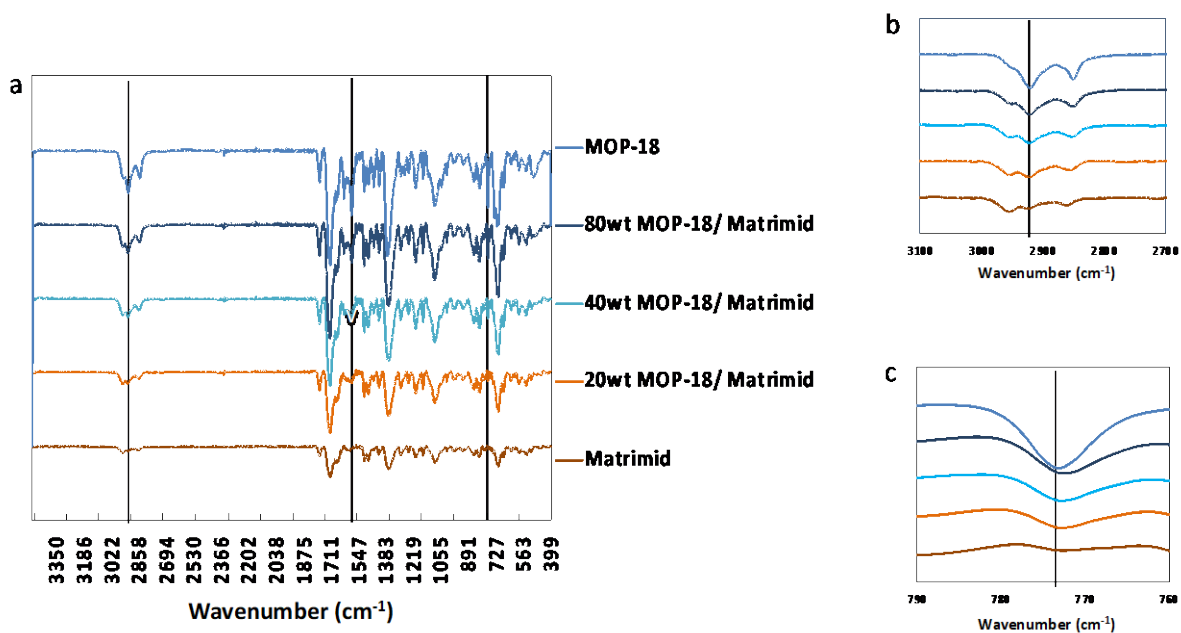


Figure 3.14: (a) FTIR spectra of MOP-18 and Matrimid[®] 5218 derived MMMs, with insets highlighting the (b) C-H, and (c) Cu-O stretch associated with the incorporation of MOP-18

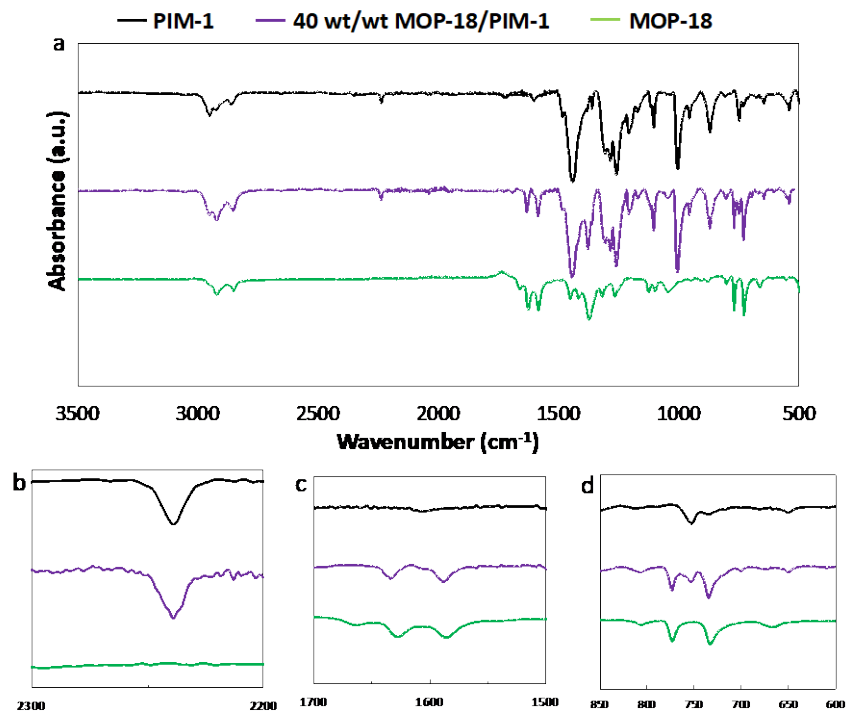


Figure 3.15: (a) FTIR spectra of MOP-18 and PIM-1 derived MMMS with insets highlighting (b) -CN stretch associated with PIM-1, along with the (c) C=C alkene and (d) Cu-O stretch associated with the incorporation of MOP-18

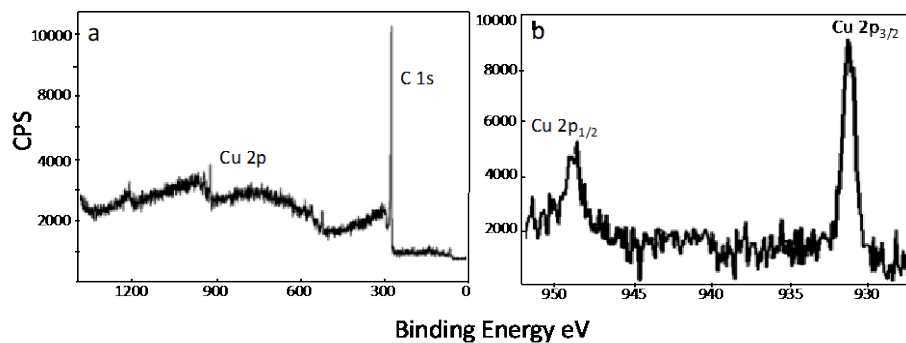


Figure 3.16: XPS spectra of 40 wt/wt MOP-18/Matrimid[®] 5218 CMSM: (a) survey, and (b) copper

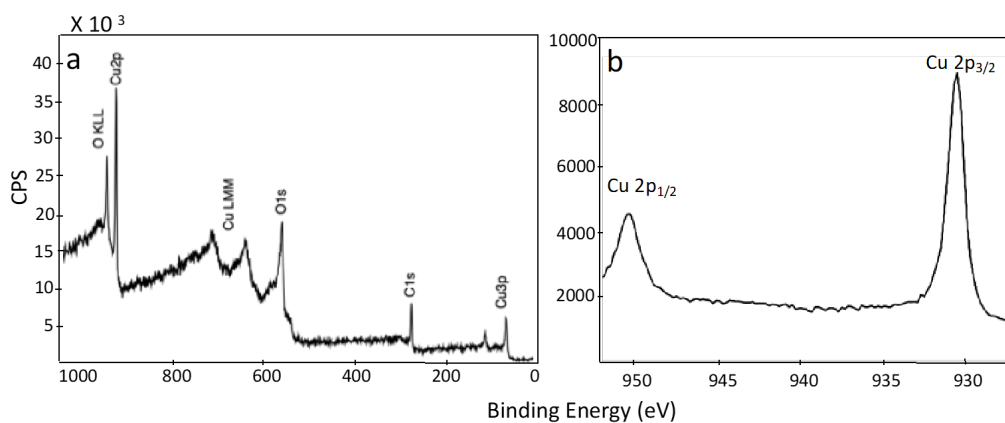


Figure 3.17: XPS spectra of 40 wt/wt MOP-18/PIM-1 CMSM: (a) survey, and (b) copper

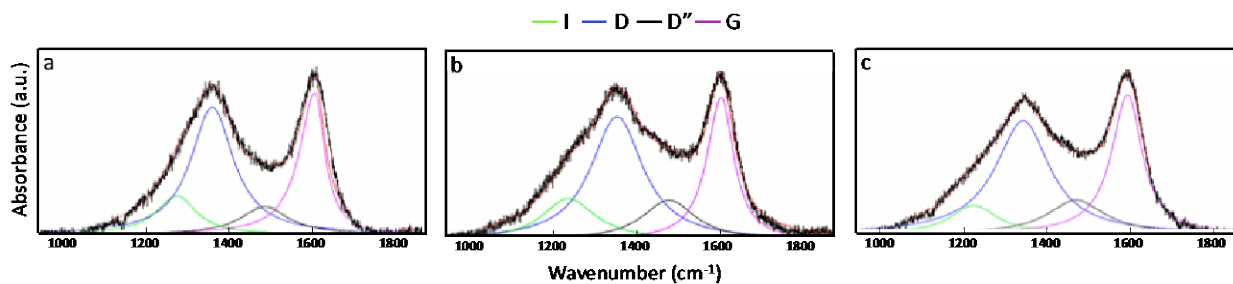


Figure 3.18: Raman spectra of (a) PIM-1, (b) MOP-18 powder, and (c) 40 wt/wt MOP-18/PIM-1 MMM pyrolyzed at 550-2

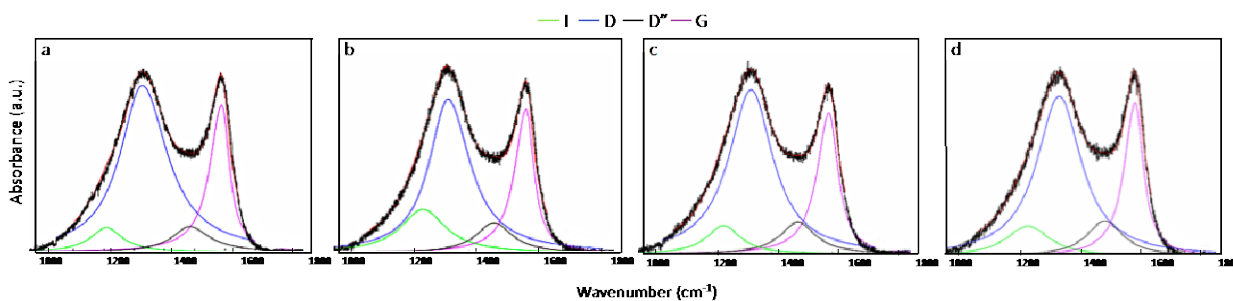


Figure 3.19: Raman spectra of MOP-18/Matrimid[®] 5218 CMSMs pyrolyzed at 900-2 with (a) 0, (b) 20, (c) 40, and (d) 80 wt/wt loadings of MOP-18

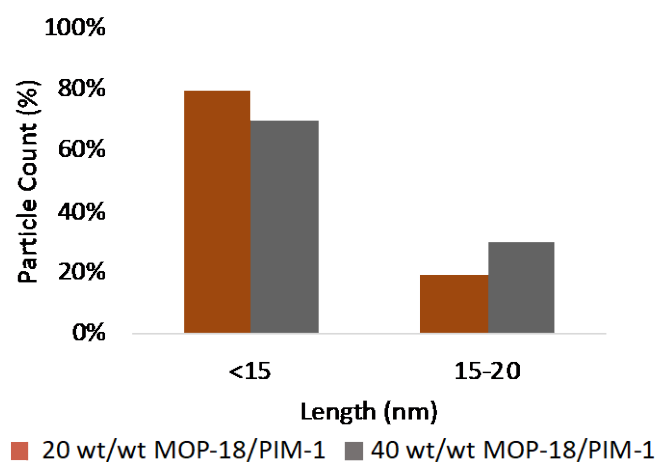


Figure 3.20: Plot of copper particle size versus particle count (%) within a 20 and 40 wt/wt MOP-18/ PIM-1 derived CMSMs

3.8 References

1. Jiang, L. Y.; Chung, T.-S.; Rajagopalan, R., Dual-layer hollow carbon fiber membranes for gas separation consisting of carbon and mixed matrix layers. *Carbon* 2007, **45** (1), 166-172.
2. Tanihara, N.; Shimazaki, H.; Hirayama, Y.; Nakanishi, S.; Yoshinaga, T.; Kusuki, Y., Gas permeation properties of asymmetric carbon hollow fiber membranes prepared from asymmetric polyimide hollow fiber. *J. Membr. Sci.* 1999, **160** (2), 179-186.
3. Yao, J.; Yu, W., Tensile strength and its variation for PAN-based carbon fibers. II. Calibration of the variation from testing. *J. Appl. Polym. Sci.* 2007, **104** (4), 2625-2632.
4. Sedghi, A.; Farsani, R. E.; Shokuhfar, A., The effect of commercial polyacrylonitrile fibers characterizations on the produced carbon fibers properties. *J. Mater. Process. Technol.* 2008, **198** (1), 60-67.
5. Yoshimune, M.; Haraya, K., Flexible carbon hollow fiber membranes derived from sulfonated poly(phenylene oxide). *Sep. Purif. Technol.* 2010, **75** (2), 193-197.
6. Mott, D.; Galkowski, J.; Wang, L.; Luo, J.; Zhong, C.-J., Synthesis of Size-Controlled and Shaped Copper Nanoparticles. *Langmuir* 2007, **23** (10), 5740-5745.
7. Boita, J.; Nicolao, L.; Alves, M. C. M.; Morais, J., Controlled growth of metallic copper nanoparticles. *N. J. Chem.* 2017, **41** (23), 14478-14485.

8. Biçer, M.; Şişman, İ., Controlled synthesis of copper nano/microstructures using ascorbic acid in aqueous CTAB solution. *Powder Technol.* 2010, **198** (2), 279-284.
9. Whitehead, C. B.; Özkar, S.; Finke, R. G., LaMer's 1950 model for particle formation of instantaneous nucleation and diffusion-controlled growth: A historical look at the model's origins, assumptions, equations, and underlying sulfur sol formation kinetics data. *Chem. Mater.* 2019, **31** (18), 7116-7132.
10. Ouyang, R.; Liu, J.-X.; Li, W.-X., Atomistic theory of Ostwald ripening and disintegration of supported metal particles under reaction conditions. *J. Am. Chem. Soc.* 2013, **135** (5), 1760-1771.
11. Meakin, P., Diffusion-limited droplet coalescence. *Physica A* 1990, **165** (1), 1-18.
12. Perez, E. V.; Balkus, K. J.; Ferraris, J. P.; Musselman, I. H., Metal-organic polyhedra 18 mixed-matrix membranes for gas separation. *J. Membr. Sci.* 2014, **463**, 82-93.
13. Song, J. et al., Linear high molecular weight ladder polymers by optimized polycondensation of tetrahydroxytetramethylspirobisindane and 1,4-dicyanotetrafluorobenzene. *Macromolecules* 2008, **41** (20), 7411-7417.
14. Lu, Z. et al., Synthesis and structure of chemically stable metal-organic polyhedra. *J. Am. Chem. Soc.* 2009, **131** (35), 12532-12533.
15. Perez, E. V.; Balkus, K. J.; Ferraris, J. P.; Musselman, I. H., Instrument for gas permeation measurements at high pressure and high temperature. *Rev. Sci. Instrum.* 2013, **84** (6), 065107.
16. Koros, W. J.; Fleming, G. K., Membrane-based gas separation. *J. Membr. Sci.* 1993, **83** (1), 1-80.
17. Perez, E. V.; Kalaw, G. J. D.; Ferraris, J. P.; Balkus Jr, K. J.; Musselman, I. H., Amine-functionalized (Al) MIL-53/VTEC™ mixed-matrix membranes for H₂/CO₂ mixture separations at high pressure and high temperature. *J. Membr. Sci.* 2017, **530**, 201-212.
18. Ryu, J.; Kim, H.-S.; Hahn, H. T., Reactive sintering of copper nanoparticles using intense pulsed light for printed electronics. *J. Electron. Mater.* 2011, **40** (1), 42-50.
19. Yeshchenko, O. A.; Dmitruk, I. M.; Alexeenko, A. A.; Dmytruk, A. M., Size-dependent melting of spherical copper nanoparticles embedded in a silica matrix. *Phys. Rev. B* 2007, **75** (8), 085434.
20. Knight, D. S.; White, W. B., Characterization of diamond films by Raman spectroscopy. *J. Mater. Res.* 2011, **4** (2), 385-393.

21. HÄGg, M. B.; Lie, J. A.; LindbrÅThen, A., Carbon Molecular Sieve Membranes. *Ann. N. Y. Acad. Sci.* 2003, **984** (1), 329-345.
22. Xu, L. et al., Physical aging in carbon molecular sieve membranes. *Carbon* 2014, **80**, 155-166.
23. Wieneke, J. U.; Staudt, C., Thermal stability of 6FDA-(co-)polyimides containing carboxylic acid groups. *Poly. Degrad. Stab.* 2010, **95** (4), 684-693.
24. Luo, S.; Wiegand, J. R.; Gao, P.; Doherty, C. M.; Hill, A. J.; Guo, R., Molecular origins of fast and selective gas transport in pentiptycene-containing polyimide membranes and their physical aging behavior. *J. Membr. Sci.* 2016, **518**, 100-109.
25. Staiger, C. L.; Pas, S. J.; Hill, A. J.; Cornelius, C. J., Gas separation, free volume distribution, and physical aging of a highly microporous spirobisindane polymer. *Chem. Mater.* 2008, **20** (8), 2606-2608.
26. Cheng, Y.; Wang, Z.; Zhao, D., Mixed matrix membranes for natural gas upgrading: current status and opportunities. *Ind. Eng. Chem. Res.* 2018, **57** (12), 4139-4169.

APPENDIX A

A THERMAL CVD METHOD FOR THE SYNTHESIS OF AN AMORPHOUS CARBON GUTTER LAYER ON STAINLESS STEEL

Abstract

A method is described to synthesize an amorphous carbon (a-carbon) gutter layer by thermal chemical vapor deposition (th-CVD) directly onto stainless steel tubular substrates. This method allows the bulk metal surface to serve both as the catalyst for carbon synthesis and the support for the membranes. The use of a gutter layer enhanced the adherence of the carbon membrane to the support and also minimized membrane defects.

Introduction

Carbon molecular sieve membranes (CMSMs) for gas separations have made significant progress in recent years. An imperative step in their commercialization is a design module capable of supporting their high flux and mechanical inelasticity. Tubular supports are often used for these systems; however, the commercially available alumina supports are economically unfeasible (>\$700 each). The commercially available supports are made from metal oxides such as alumina or zirconia. These metal oxides allow for the resultant CMSM to bind to the support, minimizing defects due to torsional strain. Reducing the cost of the support by utilizing a stainless-steel support with a binder layer, instead of alumina or zirconia, would be economically beneficial. In this appendix, I report a simple processing technique involving cost-effective stainless steel (Type 316L, \$35 per support) that can be used as a substrate for the direct growth of amorphous carbon. The composition of the stainless steel is listed in Table A.1. The carbon layer serves as a gutter

layer between the support and the CMSM, where a gutter layer is defined as a permeable material that serves as a binder medium.¹

Table A.1: Chemical composition of stainless-steel type 316L

Grade 316L	S	P	C	Si	Mn	Mo	Ni	Cr	Fe
wt %	0.03	0.045	0.08	1	2	2.5	12	17	Balance

Stainless steel (SS) can readily be used for carbon growth due to its high iron content (65%). A direct growth of carbon on the bulk metal substrate may enhance the adherence of the tubes to the CMSMs. Various procedures have been used for synthesizing carbon nanotubes (CNTs) on this material. These techniques include plasma-enhanced chemical vapor deposition, thermal CVD, and the partial oxidation of methane.² However, these techniques require substrate treatment as well as the addition of a catalyst to grow CNTs.³ A CNT growth procedure is adapted for this project to grow carbon on 316L stainless steel tubular supports. In this case, the stainless steel itself provides the active sites for CNT growth, enhancing the carbon-substrate surface interaction.

Experimental

Materials

Polybenzimidazole (PBI) 26 wt% dope in DMAc with 1.5 wt% LiCl was purchased from PBI Performance Products, Inc. DMAc was purchased from Fischer Scientific. 316 Stainless Steel tubular supports (Part No: G971030027) were purchased from Graver Technologies (Schematic shown in Figure A.1). The nominal porosity of 0.02 μm was used for the supports.

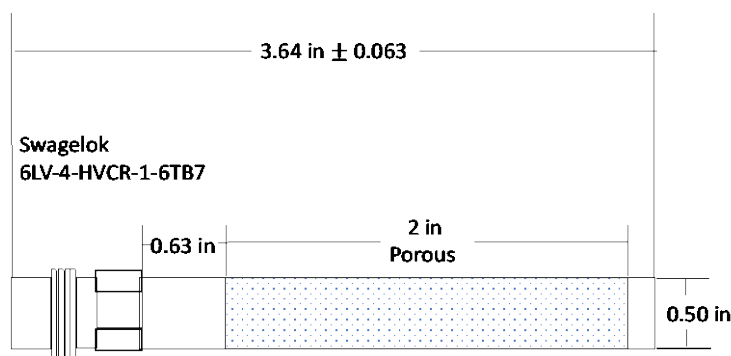


Figure A.1: Schematic of tubular support acquired from Graver technologies

Synthesis of a-Carbon

The SS supports were placed on a quartz stage and placed directly in a quartz tube. The CVD furnace used is a 3-zone tube (MSI-1200X-III), with a quartz tube (National Scientific Company, GE Type 214 Quartz) fitted with a PID temperature controller (Omega Engineering, Inc., model CN1507TC). The carbon source and carrier gases are acetylene (C_2H_2) and nitrogen (N_2), respectively. The N_2 and C_2H_2 flow rates are set at 200 ± 5 sccm and 17 ± 5 sccm, respectively. The protocol used is summarized in Figure A.2. The supports were taken from 20 °C to 725 °C at a rate of 24 °C/min under a flow of UHP N_2 (200 sccm). The temperature was held at 725 °C for 30 min, followed by the addition of C_2H_2 for 6 min. After introducing C_2H_2 , the support was held for an additional 5 min under N_2 and then cooled to room temperature.

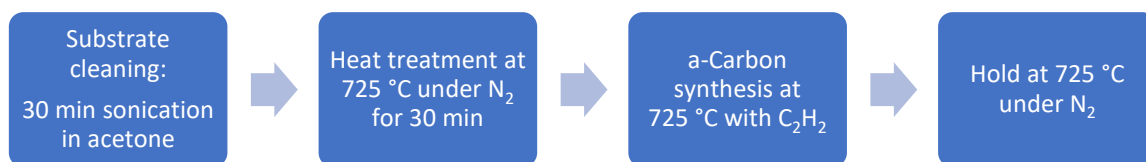


Figure A.2: Procedure for a-carbon growth on 316L stainless steel

Fabrication of precursor polymeric membranes

Pristine PBI tubular membranes were prepared by diluting the 26 wt% PBI dopant to 15 wt% with DMAc. The solution was stirred for 24 h at room temperature. The SS tubular support coated with amorphous carbon was then immersed in the polymer solution and removed slowly. The tubular membrane was then dried at 50 °C for 12 h under N₂ and then annealed in a vacuum oven at 300 °C for 1 d. The average thickness for the tubular membrane was 80 μm.

Formation of carbon molecular sieve membranes

The CMSMs were formed by pyrolysis of the precursor PBI membranes. A three-zone tube furnace (MSI-1200X-III) with a quartz tube (National Scientific Company, GE Type 214 Quartz) was fitted with a PID temperature controller (Omega Engineering, Inc., model CN1507TC). Precursor membranes were placed on a graphite plate inside the quartz tube. Pyrolysis was carried out using the temperature protocol displayed below, under a continuous flow of Ultra High Purity Nitrogen (UHP, 200 cm³/min). The CMSMs were removed from the furnace after cooling to room temperature under nitrogen and characterized.

Carbonization Protocol

1. 20 – 250 °C at a ramp rate of 15 °C/min
2. 250 – 535 °C at a ramp rate of 3.85 °C/min
4. 535 – 550 °C at a ramp rate of 0.25 °C/min
5. 120 min soak at 550 °C

Characterization

a-Carbon was grown on flat SS supports following the procedures described above. The a-carbon grown on SS was imaged using a Zeiss SUPRA 40 scanning electron microscope (SEM). Raman analysis of the a-carbon was obtained using a DXR Raman spectrophotometer with a 532 nm laser.

Results and discussion

Stainless steel itself provides poor adhesion to carbon membranes. This was determined by coating a tubular support in polybenzimidazole (PBI) and then pyrolyzing the membrane at 550 °C. The membrane flaked off the support after pyrolysis as shown in Figure A.3. Due to the poor adherence of the membrane to the support, a “gutter” or binding layer is required. Several authors have shown that a gutter layer can provide an enhanced interaction between the support and the membrane itself.¹ A carbon gutter layer was selected for this reasoning.



Figure A.3: Image of a PBI CMSM on a pristine SS tubular support

Scanning electron microscopy (SEM) of the amorphous carbon grown on 316L stainless steel is shown in Figure A.4. The non-uniformity of the carbon film was attributed to the size of the iron particles and their distribution throughout the support. Steel substrates have additional sites, such as Cr and Ni, that carbon diffuses over during the synthesis.⁴ However, these sites have a lower solubility for carbon, which may influence the growth and density of the carbon that is formed.⁴

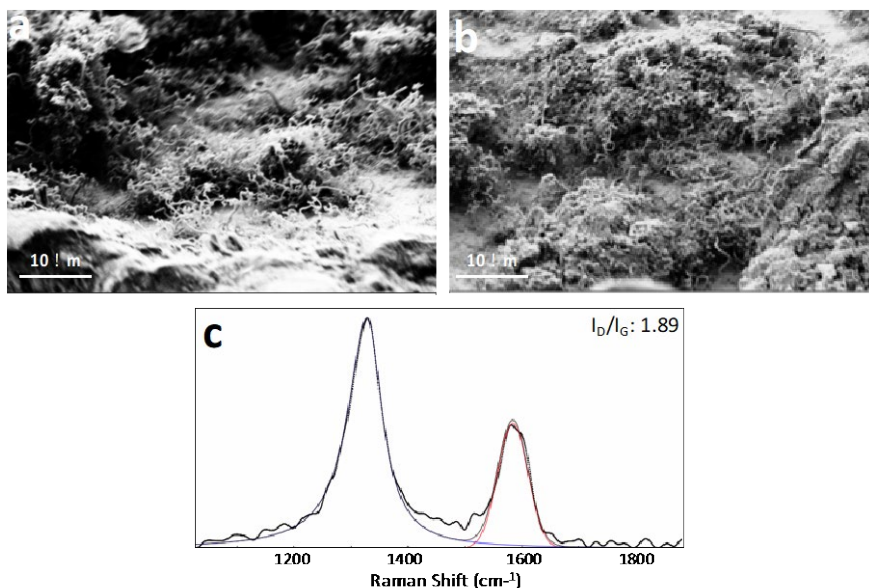


Figure A.4: (a, b) SEM images, and (c) Raman spectra of amorphous carbon grown on 316L stainless steel

The synthesized a-carbon was characterized by Raman spectroscopy to determine its relative degree of disorder. The carbon produced was highly disordered with an I_D/I_G ratio of 1.89 (see Figure A.4c). This amorphous carbon was utilized as a gutter layer. As shown in Figure A.5, a stainless-steel support following carbon growth (Figure A.5a), provided a significant increase in the adherence of the CMSM to the support (Figure A.5b). The regions where defects are observed are attributed to the non-uniform growth of the carbon in iron deficient regions of the support.



Figure A.5: (a) Stainless steel tubular support following a-carbon growth, (b) and a PBI CMSM adhered to the a-carbon gutter layer

Conclusion

In conclusion, a cost-effective stainless-steel tubular support was modified by the direct growth of α -carbon, without the use of an external catalyst. The incorporation of a carbon gutter layer allowed for an increased interaction between the carbon membrane and the support, thus minimizing membrane defects. The results suggest that the density of the carbon is directly influenced by the composition of stainless steel, and its relative percent and distribution of iron.

References

1. Tseng, H.-H.; Chang, S.-H.; Wey, M.-Y., A carbon gutter layer-modified α -Al₂O₃ substrate for PPO membrane fabrication and CO₂ separation. *J. Membr. Sci.* 2014, **454**, 51-61.
2. Masarapu, C.; Wei, B., Direct Growth of Aligned Multiwalled Carbon Nanotubes on Treated Stainless Steel Substrates. *Langmuir* 2007, **23** (17), 9046-9049.
3. Baddour, C. E. et al., A simple thermal CVD method for carbon nanotube synthesis on stainless steel 304 without the addition of an external catalyst. *Carbon* 2009, **47** (1), 313-318.
4. Camilli, L. et al., The synthesis and characterization of carbon nanotubes grown by chemical vapor deposition using a stainless-steel catalyst. *Carbon* 2011, **49** (10), 3307-3315.

BIOGRAPHICAL SKETCH

Whitney Cosey was born on September 1, 1993 in Houston, Texas. She was raised in Houston where she graduated with her BS in chemistry from Houston Baptist University in 2016. She developed interest in energy consumption and production, which led her to work at DOW Chemical Co. in 2016. She worked as a research scientist, and developed a deeper understanding of techniques being employed to reduce green-house emissions.

Whitney pursued a PhD in chemistry at The University of Texas at Dallas. She joined Dr. Inga Musselman's group in 2016 which allowed her to further expand her understanding of the technology and instrumentation used to reduce green-house emissions.

CURRICULUM VITAE

Whitney K. Cosey

800 W. Campbell Rd. Richardson,

BE 2.6, TX 75080-3021

WhitneyKCosey@gmail.com

[linkedin.com/in/whitney-cosey-analytical-chemist](https://www.linkedin.com/in/whitney-cosey-analytical-chemist)

Executive Summary

Focused and experienced analytical chemist with a passion for tackling complex problems and developing cost effective solutions. Excellent ability to maintain and operate analytical instruments, and adept at communicating scientific results to the community. Highly capable of servicing customers while maintaining company standards and policies.

Education

The University of Texas at Dallas, Richardson, TX

Department of Chemistry and Biochemistry, PhD candidate

August 2020

GPA: 3.71

Houston Baptist University, Houston, TX

College of Science and Mathematics, BS in Chemistry

May 2016

GPA: 3.35

Research Experience

The University of Texas at Dallas, Richardson, TX

Advisor: Inga H. Musselman, PhD

August 2016 - present

- Developed aging-resistant carbon molecular sieve membranes for gas separations
- Analyzed carbon molecular sieve membranes (CMSMs) using custom-built permeameters
- Improved the sustainability of CMSMs by incorporating metal nanoparticles to support the membranes microstructure

DOW Chemical Co., Freeport, TX

Advisor: Shayne Green, PhD; Mike Cheatham, PhD

June 2016 - July 2016

- Enhanced the methodology to predict whether or not polyethylene (PE) containers would generate unwanted taste and odor (T&O) based on substances stored in them
- Utilized solid phase micro extraction and stir bar sorptive extraction to analyze solutions with HPLC-MS to identify T&O components within PE resins
- Developed two methods for enhanced extraction of additives while also increasing the methods sensitivity to polar analytes

Houston Baptist University, Houston, TX
Advisor: Eric Van Caemelbecke, PhD

August 2014 to May 2016

- Probed the interactions of two diruthenium complexes, $\text{Ru}_2(\text{ap})_4\text{Cl}$ and $\text{Ru}_2(\text{Fap})_4\text{Cl}$ (ap = 2-anilinopyridinate anion) with sodium phenoxide (NaOC_6H_5) and sodium benzoate ($\text{NaO}_2\text{CC}_6\text{H}_5$) using UV-visible spectroscopy
- Determined the dimetals reaction mechanism occurred through the formation of a bisadduct and monadduct via spectroelectrochemistry and cyclic voltammetry
- Acquired fundamental knowledge on the behaviors of the two nucleophilic groups towards the dimetal complexes as well as their binding constants

Texas Christian University, Fort Worth, TX
Advisor: Geoffrey Coffey, PhD

June 2014 to July 2014

- Obtained data that proved natural forms of silica, such as tabasheer and bamboo, can be calcinated and reduced to form a mesoporous structure capable of releasing medicinal substances at a controlled rate
- Utilized X-ray analysis and cell culture plates to determine the crystallinity of silicon and its antimicrobial properties against E. coli
- Discovered a novel sustainable approach to using porous silicon as a drug delivering agent

Teaching Experience

The University of Texas at Dallas, Richardson TX

August 2016 to July 2018

- Assisted in teaching General Chemistry I and II labs and lectures
- Responsibilities: setting up all laboratory equipment, explaining procedures in accordance to the established safety guidelines, as well as collecting and grading all lab reports and quizzes

Houston Baptist University, Houston TX

August 2014 to May 2016

- Assisted in teaching General Chemistry II as well as quantitative analysis
- Responsibilities: assembling apparatuses, creating an environment for inquisitive thinking, and answering all questions proposed by the students

Skills

Instrumentation

Microscopy: SEM/EDS, TEM, AFM

Spectroscopy: FTIR, Raman, XRD, EDS, UV-VIS

Chromatography: HPLC-GC, MS-GC

Other: NMR, Autosorb, gas permeameter, Instron,

DSC, TGA, cyclic voltammetry

Software

MS: Word, Excel, PowerPoint

Other: ChemDraw, EndNote, ImageJ

Presentations

1. Cosey, K. W.; Ferraris, J. P.; Balkus, Jr., K. J.; Musselman, I. H., Aging minimization of CMSMs from the incorporation of pillars derived from copper acetate/polybenzimidazole mixed matrix membranes, *51st ACS Meeting in Miniature*, American Chemical Society, Dallas, TX, 2018. Awarded second place in the competition by The American Chemical Society.
2. Cosey, K. W.; Ferraris, J. P.; Balkus, Jr., K. J.; Musselman, I. H., Aging minimization of CMSMs from the incorporation of copper pillars derived from metal organic polyhedra-18, NAMS 28th annual meeting, North American Membrane Society, Pittsburgh, PA, 2019.
3. W.K. Cosey, K.J. Balkus Jr, J.P. Ferraris, and I.H. Musselman. Tailoring Copper Pillars to Prevent Physical Aging in Carbon Molecular Sieve Membranes. (2020) North American Membrane Society Annual Meeting. Tempe, AZ.
4. M. Tajik, W.K. Cosey, K.J. Balkus Jr, I.H. Musselman, J.P. Ferraris. Age Reduction in Highly Porous Carbon Molecular Sieve Membranes. (2020) North American Membrane Society Annual Meeting. Tempe, AZ

Publications

1. Kalluri, J.; Cosey, W.; Gonzalez, R.; Hartman, P.; Loni, A.; Canham, L. T.; Coffey, J. L. In Sustainable routes to porous silicon manufacture for drug delivery, *American Chemical Society* **2014**, pp INOR-657.
2. W. Cosey, K.J. Balkus Jr, J.P. Ferraris, and I.H. Musselman. Aging of Carbon Molecular Sieve Membranes: A Review. Under revision.
3. W. Cosey, K.J. Balkus Jr, J.P. Ferraris, and I.H. Musselman. Reduced Aging in Carbon Molecular Sieve Membranes Derived From PIM-1 and MOP-18. Manuscript submitted.
4. W. Cosey, K.J. Balkus Jr, J.P. Ferraris, and I.H. Musselman. Tailoring Copper Pillars to Prevent Physical Aging in Carbon Molecular Sieve Membranes. Under revision.

Memberships

Chemistry Graduate Student Association	2016- Present
American Chemical Society	2017- Present
North American Membrane Society	2019- Present